SETCOR
Conferences & Events

Nanotech France 2016, NanoMetrology France 2016, NanoMatEn 2016 and European Graphene Forum - EGF 2016 Joint Conferences Proceeding

http://www.setcor.org/conferences/Nanotech-France-2016

Metal nanoparticles for optical limiting: comparision of reduction with sodiumborohydrate and citrate

C. S. Hege,[1,*] S. Dengler,[1] B. Eberle,[1]

[1] Fraunhofer IOSB, Department Optronics, Ettlingen, Germany

Abstract:
Lasers radiation can damage eyes or sensors, a possibility to protect them are optical limiting devices. They attenuate intense laser beams while showing high transmittance at low intensity levels. The optical limiting is based on nonlinear optic. Metal nanoparticles act optically linear. The extent of their optical limiting ability is influenced by their shape and their size. So we compared the reduction with citrate with the reduction with sodium borohydride to see, which results in the best optical limiting.

Keywords: Optical limiting, nanoparticle synthesis, citrate, sodium borohydride

Introduction:
Metal nanoparticles as well as several organic and inorganic materials, dyes or macrocyclic rings with conjugated π-system act optically nonlinear [1]. They can be used to attenuate intense laser beams while showing high transmittance at low intensity levels. By utilizing them in so called optical limiting devices they can prevent sensors or the human eye from laser induced damage [2]. The intensity of the optical limiting of nanoparticles is related with the size and the shape of the nanoparticles.
So we examined in this study the influence of different reduction methods regarding the optical limiting properties of thus produced nanoparticles. Reduction with sodium citrate was compared to sodium borohydride.
Additionally it was analyzed if dilute concentration and long reaction times or high concentration of reduction agent and shorter reaction time give better results.

Experimental:
Silver nitrate, sodium borohydride ($NaBH_4$), sodium hydroxide, polyvinylpyrollidone (PVP, 40 kg/mol), nitric acid (all Sigma Aldrich), ascorbic acid (Alfa Aesar) were used as received.

In the first citrate reduction 5 ml of $AgNO_3$ (12 mol) were given to 15 ml of citrate solution (1 mol) in distilled water. The solution was heated to 100°C under reflux for 1 h.
In the second citrate reduction 5 ml of $AgNO_3$ (12 mol) were given to 15 ml of citrate solution (0,56 mol) in distilled water. The solution was boiled at 100°C under reflux for 4 h.
In the first $NaBH_4$-reduction, 1 ml of $AgNO_3$-solution (0,0125 mol) was given in 3 ml chloroform. 0,02 g PVP (40 kg/mol) were added and at last 500 µl of $NaBH_4$ solution (0,125 mol) in distilled water. The mixture was stirred for 4 hours.
In case of the second reduction with $NaBH_4$ 1 ml of $AgNO_3$-solution in distilled water was given to 10 ml ethanol. To this 0,11 g PVP was added. This was completed with 2 ml of $NaBH_4$-solution (7,8 mol) in distilled water. The reaction mixture was stirred for 1 hour.
The SEM-measurements were performed at 5 kV using the Hitachi SU 70.

Results:
We investigated the morphological effects of citrate and sodium borohydride reduction. In case of the citrate reduction the influence of different reduction times and additives were analyzed.

It was analyzed if dilute $NaBH_4$-solutions, or citrate solutions and longer reaction time, or concentrated $NaBH_4$-solutions or citrate solutions and shorter reduction time give better results.

The silver nanoparticles, which were produced with the citrate reduction in one hour, were small and anisotropic (see picture 1 a). The silver nanoparticles produced with a reaction time of 4 hours were wormlike (see picture 1b).
In case of the nanoparticles made with sodium borohydride neither the shape nor the size of the produced nanoparticles changes much with reduction time (see picture 1 c/d).
Consequently the optical limiting ability of the sodium borohydride produced nanoparticles is quite similar.

The worm-like nanoparticles had better optical limiting properties than the other citrate nanoparticles and the sodium borohydride particles.
The citrate nanoparticles with higher citrate concentration showed the worst optical limiting behavior. They were also with 187 nm the biggest non-structured nanoparticles.

Discussion:
The silver nanoparticles prepared with the lower amount of citrate were able to produces worm-like particles. In case of the higher citrate concentrations also after four hours only very few worm-like particles were produced and they were thicker than the other nanoworms.
The formation of nanowires/nanoworms was already shown for gold nanoparticles in case of low citrate concentration [3].
In case of the $NaBH_4$-reduction no nanoworm formation was observed.

Conclusion:
The citrate reduction with low citrate concentration produced the nanoparticles with best optical limiting ability. So it is the best of the examined reduction methods.
For optical limiting small nanoparticles or structured nanoparticles seems to be advantageous.

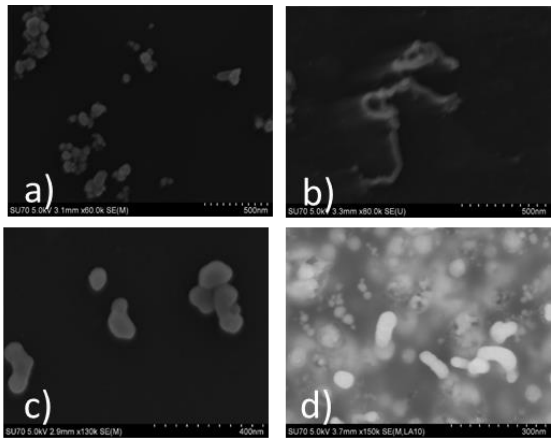

Figure 1: SEM-pictures of the nanoparticles produced by citrate reduction: a) 1 hour reaction time, 1 mol citrate solution, b) 4 hour reaction time 0,056 mol citrate solution and sodium borohydride solution a) 1 hour reduction time, 7,8 mol $NaBH_4$, b) 4 hours reduction time, 0,125 mol $NaBH_4$.

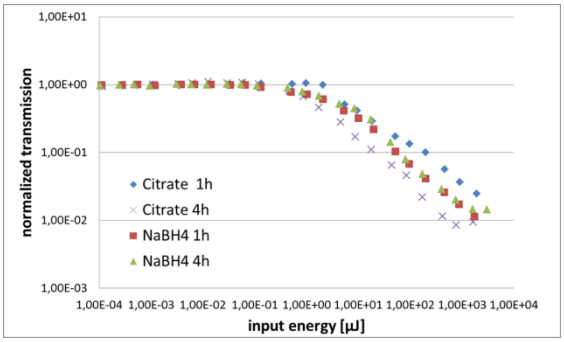

Figure 2: Measurement of the optical limiting behavior of silver nanoparticles at 532 nm. The transmittance reduces near input energies of around 1 µJ. This is important as energies of this level can damage the eye. The silver nanoparticles stabilized with citrate showed better optical limiting properties than the PVP-stabilized silver nanoparticles.

References:

1. Hollins, R. C., (1999), Materials for optical limiters, *Current Opinion in Solid State and Materials Science*, *4*(2), 189–196.
2. Dengler S, Hege C, Eberle B., (2014) Preparation and characterization of novel nanosized hybrid materials and their nonlinear optical properties, *Proc. SPIE* 9253, p 925317
3. Pei, L., Mori, K., & Adachi, M. (2004). Formation Process of Two-Dimensional Networked Gold Nanowires by Citrate Reduction of AuCl 4 - and the Shape Stabilization. *Langmuir*, *20*(17), 7837–7843. doi:10.1021/la049262v

Effect of nanoclay on short term water absorption and swelling of composites made by wood poplar flour and recycled polystyrene

A. Tavasoli,1* A. Samariha2, M. Nemati3 , Z. Masoomi4
1 Department of Agriculture, Faculty of Landscape, Islamic Azad University, Mashhad Branch, Mashhad,Iran.
2,3 Young Researchers and Elites Club, Science and Research Branch, Islamic Azad University, Tehran, Iran.
3Department of Industrial Design, Islamic Azad University, Mashhad Branch, Mashhad,Iran.

Abstract:

In this research effect of nanoclay content on short term water absorption and swelling of nano composites made by poplar flour and recycled polystyrene were investigated. Composite samples were produced by injection moulding method. 0,3 and 6 % nanoclay with 3 % MAPP were mixed to produce nanocomposites.

Nano composite samples were soaked at distilled water and 2 and 24 hours water absorption and swelling were measured according to DIN standard. Results showed that by increasing nanoclay content, water absorption and swelling of nanocomposites were decreased. Scanning electron microscopy pictures showed that by adding more nanoclay to composites, adhesion between fibers and polymer matrix has improved and voids and hollows decreased.

Keywords: nanoclay, water absorption, Composite

Introduction:

Today wood plastic composites (WPCs) are produced in progressed countries. Production of these composites is possible by too many polymers like polypropylene, polyethylene, poly vinyl colored and polystyrene(PS). Cellulosic fillers and fibers obtained from wood and paper wastes and agricultural sources are usually used in combination with polymers.

In recent years application of WPCs has gradually grown. This growth is due to some advantages of these materials like lower density, lower production costs, Biodegradability, higher Dimensional stability and higher fire resistance in comparison with raw polymers. Because of using wood flours, some defects like low impact strength and hardness has been emerged in final composites. Production of nano-composites by nano fillers can overcome to these defects. In fact the main objective of using nano scale fillers is the creation of new properties and developing new application of composites.

Polystyrene is a polymer with good resistance against water and humidity. It has good transparency and light properties. But impact strength and resistance to fire of this polymer is low. Production of PS/nanoclay composites by adding nanoclay to PS matrix will improve the morphology and mechanical strength of composites. So nowadays, industries pay more attention to using nano fillers.

Mechanical modulus, strength, heat resistance, gas permeability, physical properties and resistance against fire of polymers will improved by adding nanoclay to them.

Beside these features, investigation of physical properties of composites is necessary. Physical properties like water absorption and thickness swelling will limit extend of the use of these composites. These defects are due to hydrophilic nature of lingo cellulosic filler that are used composites. When humidity penetrates to composites, thickness swelling increase and fiber degradation will happen and finally polymer structure will destroy.

Also, water absorption destroys the compatibility between fiber and polymer matrix. This destruction lead to separation of fibers from polymer matrix and finally its connectivity became weak.

Water penetration to composites is done by three mechanisms:

1-water molecules penetrate to small pores in polymer matrix.

2-water molecules transfer by capillary process: a) to pores and cracks at intermediate region of polymer and fiber b) to wood flour and fiber pores c) to pores and cracks of composite created during the mixing and production process.

3-Fiber cell walls absorp water, because of hygroscopic nature.

Effect of short term water soaking on physical properties of waste recycled PS/wood flour /nanoclay were investigated at this research.

Materials and Methods:

Wood poplar flour was prepared from Aria Cellulose Co. wood flour screened and 60 mesh sizes were used. PS were obtained from Tabriz petroleum Co. Its melt index and density were 11g/10min and 1.07gr/cm3 respectively. Maleic anhydride polypropylene with melt index of 64gr/10 min were prepared from Solvay Co and used as a coupling agent. Nanoclay cloisite 30b were obtained from Southern clay Co.

Sample preparation

Wood flour, PS, MAPP and nanoclay were weighed (Table 1) and mixed in a mixer. Mixing temperature and rotation speed were fixed at 180 c and 60rpm respectively.

Table1: Different treatments

Wood flour %	Recycled PS%	Coupling agent(MAPP)%	Nanoclay%
50	47	3	0
50	44	3	3
50	41	3	6

After 10 minutes mixing, samples were made by injection molding machine.

Measuring physical properties

Water absorption and thickness swelling of samples after 2 and 24 hours soaking at water were measured based on DIN-EN 317. Water absorption and thickness swelling were calculated by equations 1 and 2 respectively.

$$WA(t)=(Wt-Wo)/Wi\times100 \quad (1)$$

WA: water absorption (%) at soaking time t.
Wo: weigh of samples (gr) before soaking.
Wt: weigh of samples at soaking time t.

Thickness swelling at soaking time (t) were obtained by equation 2.

$$TS(t)=(Tt-To)/To\times100 \quad (2)$$

Ts(t): thickness swelling(%) at soaking time t

To: oven dried thickness swelling.
Tt: Thickness swelling(mm) at soaking time t.
Data were analysed by SPSS software and one way Duncan test were done.

Results and Discussions

Water absorbtion

Analysis of variance showed that the effect of nano clay at 2 and 24 hours water soaking has no significant effect on water absorption. Water absorption of composites without nanoclay was higher than composites which has nanoclay. In fact water absorption after 2 and 24 hours decreased by adding nanoclay.

Thickness swelling

Analysis of variance showed that effect of nano clay on 2 hours thickness swelling had no significant effect. Thickness swelling at composites without nanoclay was higher. By addition of nanoclay to composites, thickness swelling were decreased.

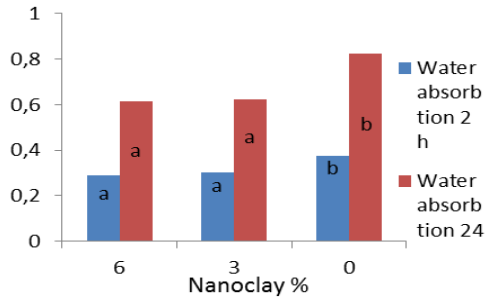

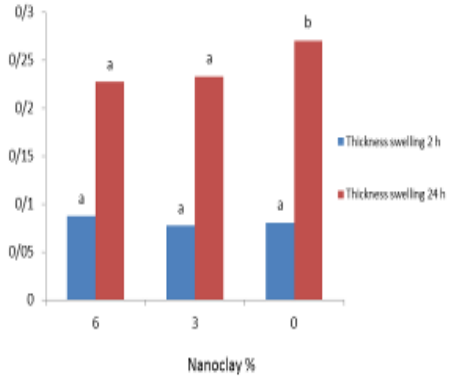

Morphology

Samples were broken and SEM pictures were obtained from surfaces. Dispertion of filler and polymer and its compatibility can be observed by SEM pictures. Creation of empty cavities shows the poor adhesion between fiber and matrix. Because of weak adhesion between fiber and polymer matrix, effect of stress and compress will pull out the fibers. Results showed that using 3 percent weigh MAPP led to create homogeny texture and fiber and polymer had good adhesion without pull out. Samples with 0 ,3 and 6 % nanoclay were shown at figures 3 (A-C)

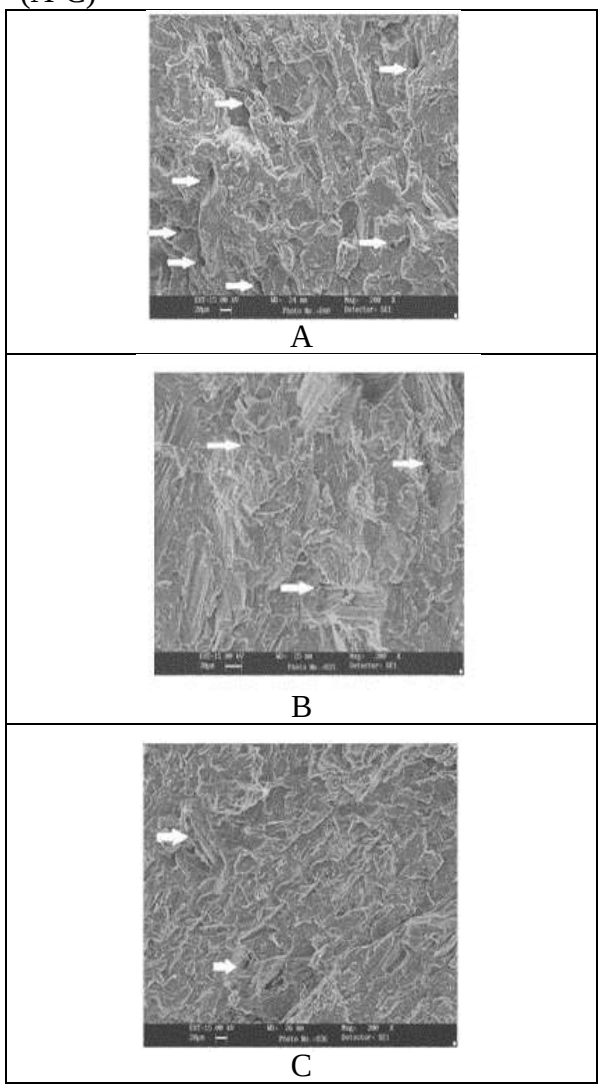

A

B

C

Figure 3: Samples with different nanoclay (A:0% nanoclay, B: 3%nanoclay C: 6% nanoclay)

.

As shown at figure 3 A , polymer matrix had good adhesion with fibers and proper distribution had been produced. Also by adding more nanoclay , number of cavities and pores decreased.

Result and discussion

Results showed that

1-water absorption and thickness swelling were decreased while adding nanoclay to WPCs. Nanoclay filled the pores and cracks between fibers and polymer materials. Water penetration to cracks and pores decreased

2- Polymeric material has usually hydrophobic nature and lignocellulos material is hydrophile.

Hydroxyl groups at cellulosic chain made new adhesion with water molecules. So water absorption of composites will improve and thickness swelling increased. Long time water soaking led to more absorption water by hydroxyl groups.

3- SEM pictures showed that adhesion between fiber and polymer improved by adding nanoclay and number of pores decreased

Refrences:

1. فرهيد، ا. 9831. برر سي تاثير الياف شيشه كوتاه و ناذو لوله كربني بر خواص پروپيلن كاربردي كامپوزيت هاي هيبريد پلي نامه كارشناسي ارشد دانشكده آرد چوب. پايان – بيعي دانشگاه تهران.كشاورزي و منابع ط

2. هياسي، م. 8831. تهيه كامپوزيت هاي اسدتايرن با ناذو رس اصلاح شده و بررسي پلي نامه كارشناسي ارشد دانشكده خواص آذها، پايان شيمي دانشگاه تبريز.

3. Arbelaiz, A., Fernandez, B., Cantero, G., Liano-Ponte, R., Valea, A., and Mondragon, I., 2005. Mechanical properties of flax fibre/polypropylene composites influence of fibre/matrix modification and glass fibre hybridization, Journal of Composites, Vol. 36, pp. 1637-1644.

4. Das, S., Sara, A. K., Choudhury, P. K., Basak, R. K., Mitra, B. C., Todd, T., Lang, S. 2000. Effect of steam pretreatment of jute fiber on dimensional stability of jute composite.

Journal of Applied Polymer Science 76, 1652–1661.

5. Espert, A. Vilaplana, F. and Karlsson, S. 2004. Comparison of water absorption in natural cellulosic fibers from wood and one-year crops in polypropylene composites and its influence on their mechanical properties. Composites, Part A, 35: 1267-1276.

6. European Standard. 1993, determination of swelling in thickness after immersion in water. Din EN 317.

7. Hon, D., & T., Sean, 1992. Composites from news prints fiber and polyolefin: their process ability and properties. Wood/plastic composites Conference proceeding. Madison, USA, 63-67.

8. Kafashi, B., Poursang, F. and Sonbolestan, E. 2007. Preparation of polyurethane/clay nanocomposites: investigating the dispersion of organoclays in PTMEG. Journal of Polymer Sciecence and Technology 20(3), 247-255.

9. Maldas, D., & Kokta, B.V, 1991. Influence of maleic anhydriedeus of coupling agent on the performance of wood fiber – polystyrene composites. Polymer engineering and Science, 31(18), 145-161.

10. Tjong, S. C. 2006. Structural and mechanical properties of polymer nanocomposites; A review. Journal of Chemical Engineering Research and Design, Vol 16, 1016-1027 pp.

Solid Cation-exchange Resin Catalysed Esterification of Lactic Acid with Ethanol: A Novel Kinetic Study

Edidiong Okon[1] and Edward Gobina[1]

[1] School of Engineering, Robert Gordon University Aberdeen, AB10 7GJ, United Kingdom.

Abstract:
Cation-exchange resin catalysts have attracted a lot of attention in the esterification process involving carboxylic acid and alcohol to produce ester and water as the by-product. In this work, the esterification of lactic acid and ethanol to produce ethyl lactate using different cation-exchange resin catalysts was carried out at 100 oC. The cation-exchange resin used as catalyst for the esterification process was amberlyst 36. The characterisation of the resin catalysts was determined using different methods including FTIR and liquid nitrogen at 77 K. The esterification product was tested using FTIR (Nicolet iS10) to determine the most adsorbed components on the surface of the resin catalysts. The absorption band at 2998 nm depicts C = O bond while the band at 1745 nm showed O-H bond, suggesting ethanol and water as the most adsorbed components on the surface of the resin catalysts based on the mechanism of Langmuir-Hinshelwood model. The surface area and pore size of resin was determined using the BET and BJH methods respectively. The BET result of amberlyst 36 was found to be 33.883m2/g. The BET result of amberlyst 36 was 33.883m2/g. The BET isotherm of the resin exhibited a type IV isotherm which was in agreement with the IUPAC classification for mesoporous material.

Introduction:
Ethyl lactate otherwise known as α–hydroxyl propionate has shown a lot of advantages in various industries including medicine, chemical, food and other industries because of its biodegradable and non-toxic properties [1]. Ethyl lactate can be obtained from the esterification of lactic acid and ethanol in the presence of catalysts. Esterification is normally performed in the presence of homogeneous catalyst including sulphuric acid and heterogeneous catalyst such as solid cation-exchange resins which are generally strong acids. Generally, the traditional method of removing water from the reaction system is through the use of a dehydrant solvent such as benzene or toluene. However, the quality of the products is affected due to the existence of these toxic dehydrant solvents [1]. During the continued development of the chemical processing industry, a lot of effort has been made in order to improve the yield of the desired products with the use of minimum amount of energy. Nevertheless, several conventional methods can be employed for increasing the yield of the reaction product including raising the pressure and temperature for such endothermic reaction to drive the reaction to a higher product yield whereas other methods seek to drive a reaction away for the equilibrium [2]. In spite of the numerous esterification studies using heterogeneous catalysts, only very few kinetic studies have consider the effect of adsorption, reaction and diffusion in the heterogeneous systems. This is in stark contrast to the homogeneous system. This is because, the reaction mechanisms and the rate expressions are more complicated in heterogeneous system than that of the homogeneous catalysts [3]. According to Sharma et al. [4] the kinetics of the esterification reaction products can be analysed using two methods; either by titration or using Gas Chromatography with a choice of detector and carrier gas. Using the GC-MS, the product can be analysed by matching the retention time of the reaction product to the retention time of the commercial ethyl lactate. Fourier transform infrared coupled with attenuated total reflection (FTIR-ATR) can be used for the structural analysis and this can be achieved based on the structure analysis of the spectra of the resin catalyst using the characteristic library spectra of organic compounds. Based on the heterogeneous and homogeneous approaches, the esterification reactions in the presence of cation-exchange resins can be explained using several kinetic models including Langmuir Hinshelwood (LH), Eley-Rideal (ER) and pseudo-homogeneous (PH) models [5]. In this work, the esterification of ethyl lactate was carried out using solid cation-exchange resin and the kinetic study of the adsorption

component was described using Langmuir model.

Kinetic Experimental Design and Procedure

Aqueous lactic acid (99.9 wt%), ethanol (99.9 wt%) solutions and the catalyst used for the experiments were all purchased from Sigma-Aldrich, UK. Prior to the esterification process, the fresh commercial resins were rinsed with deionised water and ethanol and were oven dried at 65 ^{o}C for 24 hrs to completely remove any poisonous substances**.** 30 mL of lactic acid with 5g of the different cation-exchange resins were charged into the reactor and heated to 100 ^{o}C. After the desired temperature has been attained, 50 mL of ethanol which had been heated separately using the heating mantle was added to the mixture in the reactor. The stirring and heating of the reaction mixture was achieved using a magnetic hot plate with a stirrer. FTIR method was used to determine the component with the strongest adsorption strength on the surface of the catalyst, while the BET isotherm of the catalysts was measured based on the liquid nitrogen adsorption at 77 K. Figure 1a shows the schematic diagram of the sequential steps that were employed for cation-exchange resin synthesis while figure 1b shows the FTIR instrument that was used for the characterisation process.

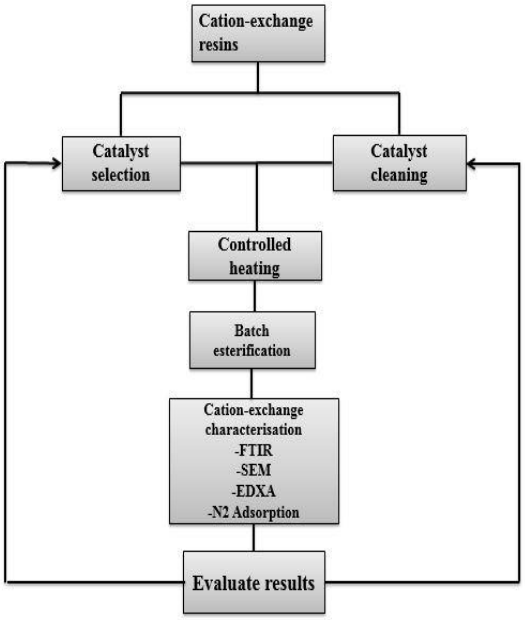

Fig. 1a: Schematic diagram of the sequential steps for Batch process esterification.

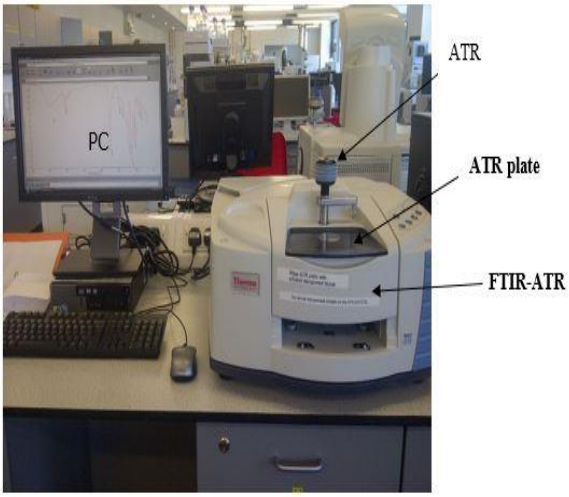

Fig. 1b. FTIR- ATR instrument for characterisation.

Results and Discussion

Figure 2 presents the FTIR-ATR spectra of the percentage transmittance (%) against the wavelength (cm^{-1}) for the esterification product at 100 ^{o}C catalysed by amberlyst 36 cation-exchange resin. It was observed from fig. 2 that there was a presence of a peak at 2996.72 and 2944.26 cm $^{-1}$ wavelengths which were attributed to O-H stretching vibration bond while the bands at 1734.43 and 1455.14 cm^{-1} corresponded to C=O and =C-O-C- functional group respectively. However, the wavelengths between 1373.77 - 757.38 cm^{-1} were attributed to the C-H functional group as shown in table 1. The C=O and –C=O-C- were suggested to originate from the lactic acid structure while C=O, C-H and O-H bonds were suggested to have originated from the ethanol and water (O-H). The assumptions of the adsorbed components for this result were explained using two mechanisms based on the Langmuir model as thus:

According to Zang et al. [13], heterogeneous reaction can be presented with many models including LM, ER and pseudo-homogenous model. Among them, LH model seems to be more appropriate for this type of reaction. The FTIR-ATR results were further tested using simplified mechanism of the Langmuir Hinshelwood model as thus:

$LA + S \leftrightarrow LA–S$ (1)

$E + S \leftrightarrow E–S$ (2)

$E – S + LA – S \leftrightarrow EL–S+W–S$ (3)

$EL – S \leftrightarrow EL+S$ (4)

$W – S \leftrightarrow W + S$ (5)

Where LA = Lactic Acid, E = Ethanol, EL = Ethyl Lactate, W = Water and S = Vacant site on catalyst surface [6]. Therefore, the LH model which describes the reaction rate as initial molar amount of lactic acid and water in the esterification process could be written as follows:

$$r = \frac{n_{LA,o}}{W}\left(\frac{dx}{dt}\right) \quad (6)$$

From equation 6, the reaction rate constant (k) involving the esterification parameters (lactic acid, ethanol, ethyl lactate and water) can be written as shown in equation 7:

$$k = \frac{a_{LA}a_E - a_{EL}a_W}{(1+k_W a_W + k_E a_E + k_{LA}a_{LA} + k_{EL}a_{EL})2} \quad (7)$$

The adsorption coefficient (i) as well as the equilibrium constant (K_{eq}) of the esterification parameters in the esterification reaction can be written using the equation 8:

$$k_i = \frac{c_i - s}{a_i\, c_s}, \qquad K_{eq} = \left(\frac{a_{EL}\ x\ a_W}{a_{LA}\ x\ a_E}\right)eq \quad (8)$$

In equation 6-8, $n_{LA,0}$= initial molar concentration of lactic acid and w = the catalyst loading, k = represents the reaction rate constant, k_i = adsorption coefficient, C_s = the concentration of vacant site on catalyst surface, $C_i – s$ = the concentration of component i at the catalyst surface, a_i = the activity for component and K_{eq} = the reaction equilibrium constant. Although ethanol and water were identified as the most adsorbed components on the surface of the resin catalysts, lactic acid was also suspected to also adsorb on the surface of the resins. However, two mechanisms of the Langmuir model were tested in order to determine which one of these was more suitable to describe the adsorption components. The 1st mechanism assumes that ethanol and water adsorbed much stronger than other components in the esterification solution and as such, the adsorption of lactic acid and ethyl lactate were ignored. The kinetic equations for the two mechanisms (1st and 2nd) were written by combining equation 7 and 8.

In the 1st mechanism, it was assumed that water and ethanol adsorbed on the surface of the resin catalysts as in the denominator of equation 9.

$$r = k\ \frac{a_{LA}a_E - \frac{u_{EL}u_W}{keq}}{(1+k_W a_W + k_E a_E)2} \quad (9)$$

In comparison to the first mechanism, in the second mechanism it was assumed that water and lactic acid adsorbed most in the second mechanism as shown in the denominator of equation 10.

$$r = k\ \frac{a_{LA}a_E - \frac{u_{EL}u_W}{keq}}{(1+k_W a_W + k_{LA}a_{LA})2} \quad (10)$$

In both 1st and 2nd mechanisms, there are three parameters involved instead of five parameters to be evaluated at a constant reaction temperature. In the 1st mechanism, the parameters include: k, k_W and k_E whereas for the 2nd mechanism, the corresponding parameters are k, k_W and $k_{LA.}$ These results further confirm Langmuir model as the fitted model for the description of the adsorption components. This model was based on a similar work by Zang et la. 2004 [6].

Table 1: Wavenumber and their respective functional groups

Wavelength (cm^{-1})	Functional group
2996.72	O-H
2944.26	O-H
1734.43	C=O
1455.14	=C-O-C-
1373.77	C-H
1216.39	C-H
1121.31	C-H

1045.93	C-H
1013.11	C-H
924.59	C-H
757.38	C-H

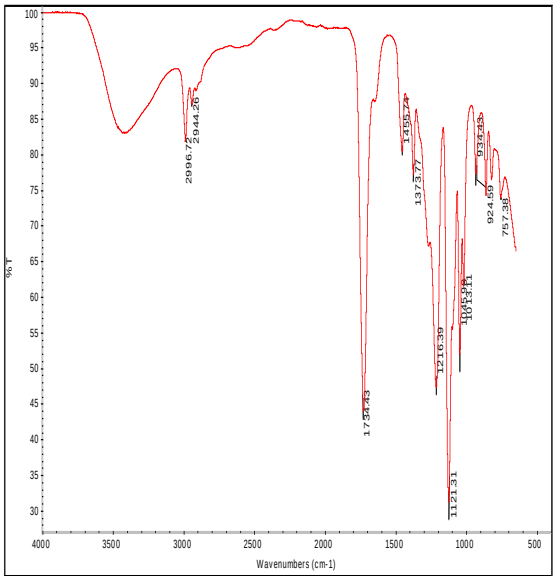

Fig.2. FTIR spectra of esterification reaction product catalysed by amberlyst 36 at 100 ^{o}C and the wavelength region of 500 – 4000cm $^{-1}$.

Figure 3 presents the relationship between the volume @ STP (cc/g) and the relative vapour pressure (P/P_o). From the results obtained, it was found that the BET surface area of the amberlyst 36 resin catalysts showed a high surface area of 33.883 m^2/g as shown in table 2 which was in accordance with the IUPAC nomenclature for mesoporous materials. A similar result was obtained in our previous study at 60 ^{o}C [7].

Table 2. BET summary of the catalyst

Slope	90.201
Intercept	1.26E+01
Correlation Coefficient, r	1
Constant, c	8.169
Surface area	33.883

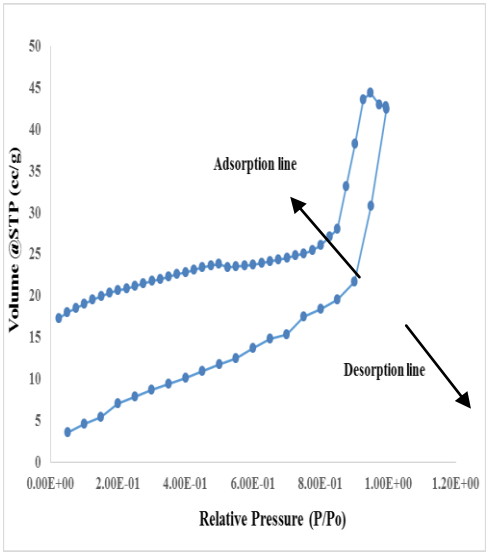

Fig. 3. N_2 adsorption/desorption BET isotherm for amberlyst 16 at 77 K.

Conclusion

The esterification of lactic acid with ethanol to produce the corresponding ethyl lactate was carried out using a batch process. The characterisation methods included FTIR and Liquid nitrogen. The spectra for the FTIR showed different functional groups including C=O, O-H and C-H. Ethanol, water and Lactic acid were identified as the most adsorbed components on the surface of the resin catalysts. The Langmuir model was found to be the best fitted model for the description of the adsorption component on the resin surface. The BET surface area of the amberlyst 36 exhibited a type 4 isotherm which was in accordance with the IUPAC classification of mesoporous material.

Acknowledgment

The author wishes to express sincere thanks to The Centre for Process Integration and Membrane Technology (CPIMT) for supplying the infrastructures used for the study, School of pharmacy and life science at RGU for the FTIR analysis. Additionally, CCEMC is gratefully acknowledged for their financial contribution towards the research work.

Nomenclature

LA = Lactic acid
E = Ethanol
W = Water
EL = Ethyl lactate
T = Temperature (K)

$n_{LA,0}$ = Initial molar amount of lactic acid (mol)
k_i = adsorption coefficient
k = rate constant ($molg^{-1}min^{-1}$)
K_{eq} = reaction equilibrium constant
c_i = concentration of i at the surface of the catalyst (mol/L)
t = time (min)
r = reaction rate ($molg^{-1}min^{-1}$)
C_s = the concentration of vacant site on catalyst surface
S = vacant site on catalyst surface
LM= Langmuir Hinshelwood (LH)
ER = Eley-Rideal
PH = Pseudo-homogeneous.

References

1. Zhang M, Chen L, Jiang Z, Ma J. Effects of Dehydration Rate on the Yield of Ethyl Lactate in a Pervaporation-Assisted Esterification Process. *Industrial & Engineering Chemistry Research.* 2015; 54(26):6669-6676.
2. Armor JN. Overcoming equilibrium limitations in chemical processes. *Applied Catalysis A: General.* 2001; 222(1–2):91-99.
3. Sharma M, Wanchoo RK, Toor AP. Adsorption and kinetic parameters for synthesis of methyl nonanoate over heterogeneous catalysts. *Industrial & Engineering Chemistry Research.* 2012; 51(44):14367-14375.
4. Sharma M, Wanchoo R, Toor AP. Amberlyst 15 Catalyzed Esterification of Nonanoic Acid with 1-Propanol: Kinetics, Modeling, and Comparison of Its Reaction Kinetics with Lower Alcohols. *Industrial & Engineering Chemistry Research.* 2014; 53(6):2167-2174.
5. Lomba L, Giner B, Zuriaga E, Gascón I, Lafuente C. Thermophysical properties of lactates. *Thermochimica Acta.* 2014; 575(0):305-312.
6. Zhang Y, Ma L, Yang J. Kinetics of esterification of lactic acid with ethanol catalyzed by cation-exchange resins. *Reactive and Functional Polymers.* 2004; 61(1):101-114.
7. Edidiong Okon, Habiba Shehu, Edward Gobina. Experimental Characterisation of Cation-exchange Resin for Biomass Green Solvent Production. *International Journal of Scientific Engineering and Technology. 2016; 5(4); Pp 173 – 179.*

Dynamic identification of perforated MEMS devices by the continuous wavelet transform

J. Lardiès[1] , T.P. Le[2]
[1]Université Bourgogne Franche-Comté, Institut FEMTO-ST, DMA, 2500 Besançon, France
[2]Université Clermont Auvergne, Sigma-Clermont, Institut Pascal,BP 10448,F-63000 Clermont-Ferrand, France

ABSTRACT

Micro electro mechanical systems (MEMS) are built using integrated circuits and include movable parts, such as perforated microplates, wich can oscillate. To control such oscillations it is necessary to know the modal parameters: eigenfrequencies, damping ratios and stiffness of the perforated microplates. The purpose of this communication is to identify the modal parameters of a perforated microplate using only the time data obtained from the displacement of the microplate. Dynamic measurements of a perforated microplate are conducted in time domain and we use the continuous wavelet transform of such measurements to identify the modal parameters of the vibrating perforated microplate. Experimental results are presented showing the effectiveness of the procedure in modal parameter identification.

Key-Words
MEMS, perforated microplate, oscillating system, dynamic response, wavelet transform, modal parameters, experimental identification.

1. INTRODUCTION

The design of micro electro mechanical systems (MEMS) includes oscillating elements and components which are often perforated microplates supported by elastic suspensions. The main purpose of the holes, due to perforations, is to reduce the damping and spring forces acting in the MEMS. These forces come essentially from the fluid flow inside and around the micro structure. The study of the damping caused by surrounding fluid and by the dissipations in the material is very important to predict the dynamic response of the microsystem and to estimate the quality factor. G. De Pasquale and T. Veijola (2008) used numerical strategies for the estimation of the damping force acting on a perforate movable MEMS, using FEM methods with ANSYS. It was shown that ANSYS results contained a systematic error at small perforations and were not usable for large perforations. A method was proposed by J. Lardiès (2015) to estimate the modal parameters of a perforated micro structure using the subspace approach. The parameters were identified by eigendecomposition of the transition matrix. In this communication we propose a time-frequency method to identify the modal parameters of a perforated microplate. Applying the continuous wavelet transform (CWT) to the displacement response of the microstructure we identify the modal parameters. Experimental results are presented showing the effectiveness of the method.

2. CONTINUOUS WAVELET TRANFORM METHOD

The continuous wavelet transform of a signal $x(t)$ is an example of a time-scale decomposition obtained by dilating and translating along the time axis a chosen analysing function called mother wavelet. The CWT is defined as *(Torresani B.*, 1995 ; *Le T.P and Argoul P.*, 2015)

$$(W_\psi x)(a,b) = \frac{1}{\sqrt{a}} \int_{-\infty}^{+\infty} x(t)\psi^*\left(\frac{t-b}{a}\right) dt \qquad (1)$$

where a is the dilatation or scale parameter defing the analysing window stretching, b is the translation parameter localising the wavelet function in the time domain and $\psi(t)$ is the mother analysing wavelet function. The CWT gives time and frequency information about the analysed data. Any function $\psi(t)$ can be used as an analysing wavelet when it satisfies the admissibility condition *(Torresani B.*, 1995), this condition being necessary to obtain the inverse of the CWT. There are a number of different complex and real valued functions used as analysing wavelets, but the Morlet wavelet may be the most commonly considered and will be used in this communication. The Morlet wavelet is defined in the time domain as

$$\psi(t) = e^{j\,\omega_o t}\; e^{-t^2/2} \qquad (2)$$

where ω_o is the oscillating frequency of the analysing wavelet. The Morlet wavelet is basically a sinusoidal function, oscillating at the frequency ω_o and modulated by a Gaussian

envelope of unit width. In the frequency domain the dilated Morlet wavelet becomes

$$\Psi(a\omega) = \sqrt{2\pi}\; e^{-\frac{1}{2}(a\omega - \omega_o)^2} \qquad (3)$$

and the maximum is located at $a\omega = \omega_o$.

3. MODAL PARAMETER IDENTIFICATION BY THE CWT

Consider a modulated signal in amplitude and frequency : $x(t)=A(t)\cos(\varphi(t))$. The CWT of $x(t)$ is

$$(W_\psi x)(a,b) = \frac{\sqrt{a}}{2}\; A(b)\; \Psi^*(a\,\dot{\varphi}(b))\; e^{j\varphi(b)} \qquad (4)$$

where $\dot{\varphi}(b) = d\varphi(b)/db$ is the instantaneous frequency of the signal. The dilatation parameter is obtained when $|(W_\psi x)(a,b)|$ is maximum, that is $a = a(b) = \omega_o / \dot{\varphi}(b)$ and (4) becomes

$$(W_\psi x)(a(b),b) = \sqrt{\pi\, a(b)/2}\; A(b)\, e^{j\varphi(b)} \qquad (5)$$

Now, consider the impulse response of a viscouly damped single degree of freedom system

$$x(t) = B\, e^{-\zeta\,\omega_n t}\cos(\omega_d\, t + \chi_o) \qquad (6)$$

where $\omega_d = \omega_n\sqrt{1-\zeta^2}$ is the damped angular frequency and ξ the damping factor. It is easy to see that $A(t) = B\, e^{-\zeta\,\omega_n t}$ and $\varphi(t) = \omega_d\, t + \chi_o$ so $\dot{\varphi}(t) = \omega_d$. The amplitude of the wavelet transform is maximum for the constant scale $a=a_1=\omega_0/\omega_d$ and we obtain the ridge of the CWT. Equation (5) becomes

$$(W_\psi x)(a_1,b) = \sqrt{\pi\, a_1/2}\; B\, e^{-\zeta\,\omega_n b}\; e^{j(\omega_d b + \chi_0)} \qquad (7)$$

From (7) we can deduce

$$\mathrm{Arg}\,((W_\psi x)(a_1,b)) = \omega_d\, b + \chi_o \qquad (8)$$

$$\ln(|(W_\psi x)(a_1,b)|) = -\xi\omega_n b + \text{constant} \qquad (9)$$

The phase function is a straight line whose slope represents the damped angular frequency. The log of the wavelet modulus cross-section is again a straight line whose slope is the decay rate $\xi\omega_n$. Once the instantaneaous frequency and the decay rate have been estimated we can identify the natural frequency and the damping ratio of the vibrating system.

4. MODAL PARAMETER IDENTIFICATION OF A PERFORATED MICROPLATE

The perforated microplate supported by an elastic suspension as shown in Figure 1, and the mechanical model used to study the microplate behavior is constituted by the following parameters : the plate mass *m* concentrated in the center of the plate, the damping coefficient *c* and the stiffness coefficient *k*. The dynamic measurements are conducted in time domain by means of a laser vibrometer. The sampling frequency is 2 MHz.

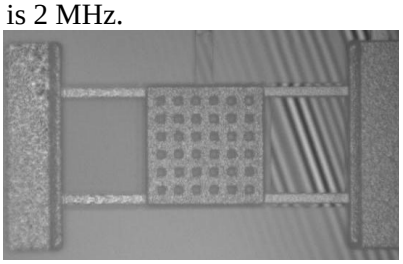

Figure 1. Optical image of the perforated microplate

The perforated microplate area is $A = 3.127\text{x}10^{-8}$ m^2 and its mass is $m = 3.814\text{x}10^{-9}$ kg. The microplate stiffness is given by $k = m\,(2\,\pi F)^2$ and the damping coefficient is $c = 4\,\pi\, m\, F\,\xi$ where F is the resonance frequency of the perforated microplate and ξ the damping factor. Figure 2 shows the time response of the microplate center to a step force actuation and the CWT amplitude of this time response. We obtain then the ridge of the wavelet transform and we can isolate the scale parameter given the maximum of the CWT amplitude.

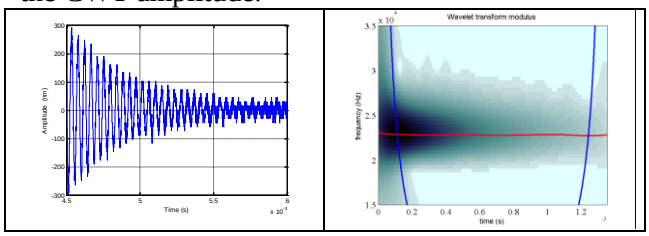

Figure 2. Displacement response of the microplate and its CWT amplitude

The modal parameters are obtained from the ridge of the CWT using the slopes of straight lines presented in Figure 3, as explained in section 3. Table 1 presents their identified values.

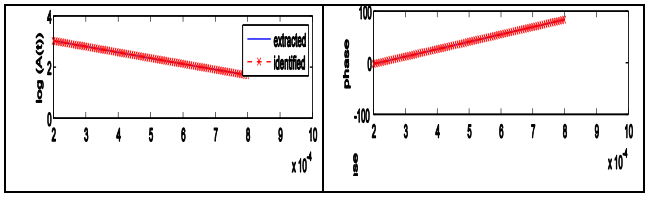

Figure3.Logarithm of the amplitude and phase of the CWT

Resonance frequency F	Damping factor ξ	Stiffness coefficient k	Damping coefficient c
22805 Hz	1.58 %	78.31 N.m-1	17.27x10-6 N.s.m-1

Table 1. Parameter identification of the microplate

5. CONCLUSION

The effectiveness of the CWT identification procedure developed in the paper has been applied to modal parameter identification of a perforated microplate. Experimental results are presented showing the accuracy of the method.

References:

De Pasquale G. and Veijola T. (2008) Comparative numerical study of FEM methods solving gas damping in perforated MEMS devices, *Microfluid Nanofluid* 5, 517-528.

Lardiès J. (2015) Modal parameter identification of perforated microplates from output data only, *Nanotech France 2015*.

Torrésani B. (1995) Analyse continue par ondelettes, *Inter Editions/CNRS, Paris*

Le T.P. and Argoul P. (2015) Distinction between harmonic and structural components in ambient tests using the time-frequency domain decomposition technique, *Mechanical Systems and Signal Processing* 52, 29-45.

Development of Flexural Properties in Woven-fabric/Epoxy Resin CFRP Panels with Additional Nano Rubber Particle Reinforcement

J. Sirichantra,[1,*] T. Pullawan,[1] P. Lamo,[1] S. Kumwongwian[1]
[1]Department of Science Service, Ministry of Science and Technology, Bangkok, Thailand

Abstract:
Twill woven carbon fibre fabric have been impregnated with the modified epoxy resins with additional nano rubber particles (Narpow®UFPR VP-501) in the range of 0 to 1 wt%. The laminates were studied in flexural properties and sectioned subsequently for microstructural damage investigation. In addition, the TEM observation was used to investigate the nano-sized Narpow®UFPR VP-501dispersed in the epoxy resin matrix. The results showed that the panels with modified epoxy resins by adding nano rubber particles up to 1 wt% were developed approximately 16% and 17% in the flexural strength and modulus of elasticity in bending, respectively. For microstructural damage investigation, the cross sections of the specimens with additional 0 and 1 wt% nano rubber particles were examined after the flexural test as shown in Figure 1. It can be seen that for the specimen without nano rubber particle (Figures 1(a)) that substantial delamination of the composite has occurred after the flexural test, whereas less damage is evident in the specimen containing a dispersion of 1 wt% nano rubber particles (Figure 1(b)). This is consistent with a higher resistance to delamination being shown by the specimens additionally reinforced with 1 wt% nano rubber particles after the bending flexural test of the specimen. The observation suggest that the enhanced flexural properties are a consequence of the nano rubber particles producing a reduction in the extent of delamination during bending fracture of the specimens. In addition, the TEM images gave representative shape distributions of the Narpow®UFPR VP-501dispersed in the epoxy resin matrix (Figure 2). The diameter of nano rubber particles ranges from about 50 to 100 nm.

Keywords: carbon fibre fabric, CFRP, nano rubber particle, modified epoxy resin, flexural properties, delamination

Introduction

Nanocomposites are currently being used to be a matrix system for fibre-reinforced polymer (FRP) composite materials. The modified polymer matrix system by adding nano materials was made to improve mechanical properties in FRP such as carbon nanotubes (Yang *et al.,* 2007). Recently, modified polymer matrix with additional nano rubber particles was studied to improve the delamination fracture toughness of CFRP laminates (Zeng *et al.,* 2012) and to increase the tensile and flexural strength of GFRP panels (Srinivasarao *et al.,* 2014). However, Young's modulus and flexural modulus of the composite were decreased (Zeng *et al.,* 2012) and (Srinivasarao *et al.,* 2014). The effects of modified epoxy resin with additional nano rubber particles on flexural properties in CFRP panels should be further investigated.

Materials

Twill woven carbon fibre fabric (obtained from J.N transos Co.,Ltd. (Thailand)), stacked in a 0/90 configuration for four layers, have been fabricated using a wet lay-up method with modified epoxy resins by a random dispersion of nano rubber particles (Narpow® UFPR VP-501obtained from Siam Extek Co., Ltd (Thailand)) up to 1 wt% of the total matrix system. The fabric is 200 tex yarn twill weave with the density between 12.5 and 13.5 picks/inch. The thickness of panels was approximately 1.8 mm.

Experimental methods

The flexural properties of CFRP laminates with nano rubber reinforcement up to 1 wt% can be determined using a composite beam specimen under a three-point bending mode according to the ASTM Standard D790-10. The laminates were cut into coupons, 12.7 mm in width and 120 mm in length which were tested by the universal testing machine (Zwick Roell Z010) with the load cell 10 kN. Subsequently, the specimens without and with additional 1 wt% nano rubber particles after the flexural test were sectioned and investigated for microstructural damage observation by the optical microscope (Olympus BX60M) at a magnification of 50x. For particle size determination, the modified epoxy resin matrix with additional nano rub-

ber particles 0.25 wt% was measured the size of nano rubber particles using Transmission Electron Microscopy (TEM).

Results and discussion

Flexural testing results

The results of flexural properties of panels with additional nano rubber particles in the range of 0 to 1 wt% are shown in Table 1. The results showed that the panel with modified epoxy resins by adding nano rubber particles up to 1 wt% was developed approximately 16% in the flexural strength which is in agreement with Srinivasarao *et al* (2014). The modulus of elasticity in bending was also improved approximately 17%. However, there are few different results of flexural properties in the panels containing nano rubber particles between 0.25 wt% and 0.5 wt%.

Table 1: Flexural strength, σ_f and modulus of elasticity in bending, E_B of specimens containing nano rubber particles up to 1 wt%

CFRP with Narpow® UFPR VP-501 [wt%]	σ_f [MPa]	E_B [GPa]
0	437.7±3.1	23.6±0.5
0.25	492.6±1.3	26.0±0.1
0.5	490.4±6.0	26.6±0.1
1	509.1±3.0	27.5±0.3

Microstructural observation

Figure 1 shows the images of microstructural damages of the cross sections of the specimens after the flexural test between 0 wt% and 1 wt% nano rubber particle additions. The results show that the image of the specimen without nano rubber particle has occurred substantial delamination (Figures 1(a)), whereas less damage is evident in the composite specimen with dispersion of 1 wt% nano rubber particles (Figure 1(b)). This is consistent with a higher resistance to delamination being shown by the specimens additionally reinforced with 1 wt% nano rubber particles after the bending flexural test of the specimen. The observation suggest that the enhanced flexural properties are a consequence of the nano rubber particles producing a reduction in the extent of delamination during bending fracture of the specimens. In addition, Figure 2 shows the TEM images which gave representative shape distributions of the Narpow®UFPR VP-501dispersed in the epoxy resin matrix. The diameter of nano rubber particles ranges from about 50 to 100 nm.

Summary

This paper shows the results of flexural properties for twill woven carbon fibre fabric reinforced epoxy resin with different additional nano rubber particles (Narpow® UFPR VP-501) panels. The flexural strength and modulus of elasticity in bending of panels with modified epoxy resin additions up to 1 wt% of nano rubber particles increase approximately 16% and 17%, respectively. The microstructure observation suggest that flexural properties increase because nano rubber particles contribute the reduction of delamination during the bending test of coupons

Acknowledgements

The authors would like to thank Department of Science Service and NSTDA, Ministry of Science and Technology Thailand for the provision of funding research project, and to thank Siam Extek Co., Ltd (Thailand) for invaluable support for the Narpow® UFPR VP-501.

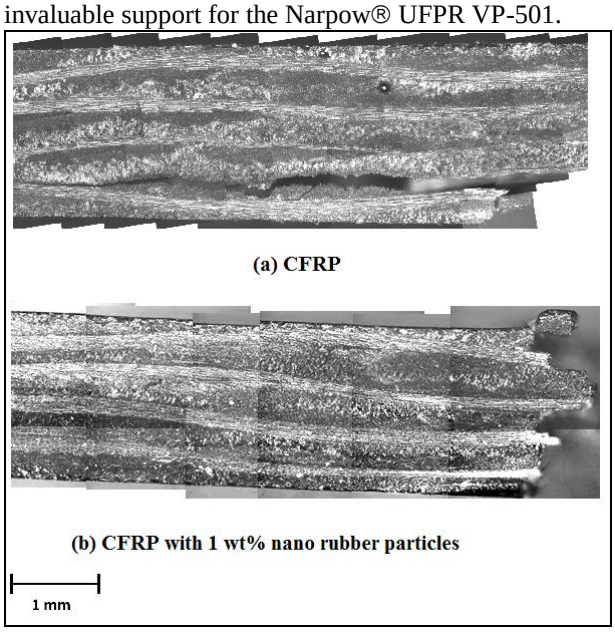

Figure 1: Cross sections of the specimens after the bending flexural test for Narpow®UFPR VP-501 additions (a) 0 wt%, (b) 1 wt%

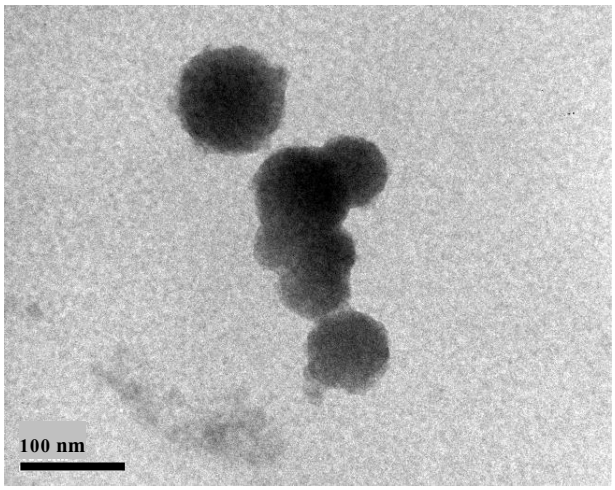

Figure 2: TEM images of the round shape distributions of the Narpow®UFPR VP-501 dispersed in the epoxy resin matrix

References:

Srinivasarao, D., Reddy, M.A., Krishna Veni, M.N.V., Mahanti, S.K. (2014), Effect of nano rubber additions on wear and mechanical properties of epoxy glass fibre composites, *IJRRCME.*, 1(1), 1-11.

Yang, Y., Lu, C.X., Su, X.L., Wu, G.P., W, X.K. (2007), Effect of nano-SiO2 modified emulsion sizing on the interfacial adhesion of carbon fibers reinforced composites, *Materials Letters.*, 61, 3601-3604.

Zeng, Y., Liu, H-Y., Mai, Y-W., Du, X-S. (2012), Improving interlaminar fracture toughness of carbon fibre/epoxy laminates by incorporation of nano-particles, *Composites Part B.*, 43, 90-94.

Temperature Controlled Growth of Ag Nanoparticles by Physical Vapour Deposition

Reem M. Alrashed and Feras G. Alzubi

Energy and Building Research Center, Kuwait Institute for Scientific Research, Safat 13109, Kuwait

Abstract:
This paper reports the fabrication of silver (Ag) nanoparticles (NPs) on silicon substrate via electron beam physical vapour deposition (PVD), followed by thermal annealing at different preset temperatures to further study the temperature difference effect on Ag NPs formation. Post physical synthesis process characterization was conducted using atomic force microscopy (AFM). AFM studies were conducted for both unannealed and annealed Ag thin-film samples. Whilst unannealed samples showed no presence of Ag NPs, annealed samples showed a clear formation of Ag NPs recognizable in the topography AFM images of the annealed samples. The images showed clear development of the surface roughness and topography compared to unanealed samples. In the case of the annealing temperature at 800^{o}C, diameters of Ag NPs ranged from 50 to 100 nm while the highest NP size was ~ 8.3 nm. Moreover, clear agglomoration was observed in the cases of annealed samples at temperatures of 500, 600, and 700 ^{o}C which to be further investigated at the completion of the running project and to be reported later.

Keywords: Silver, Nanoparticles, Noble, Growth, Annealing.

Introduction:

The synthesis of nanoparticles (NPs) of metals has been a subject of increased interest lately in many photonic and optical applications, i.e. in photovoltaic cells due to their plasmonic [1] and novel properties that can be controlled via the fabrication process. Noble NPs are efficient light capturing particles which assist converting absorbed light into electrical energy by vibrating the electrons when light passes through the structure containing the NPs. Noble NPs, especially silver (Ag), have been proven, through literature, to exhibit unique optical properties on account of their surfarce plasmon resonance (SPR) [2]. Moreover, controlling the variation in size and shape of noble metallic NPs leads to unique physicochemical characteristics, including catalytic activity, optical properties, electronic properties, and magnetic properties. However, these properties of NPs are highly depending on the fabrication techniques and the processing conditions. According to the literature, controlling the processing conditions to acheive the required size and shape has been a great challenge over the time. Several physical and chemical aproaches have been used to synthesize metallic NPs at different structures [3]. Controlling the annealing temperature is one of the main physical parameters that are used to achieve the predicted results of the NPs in terms of size, height and shape. Varying the annealing temperature is considered one of the physical approaches used to produce the required specifications of the NPs. In this paper, we report the effect of the variation of annealing temperature on the formation of the Ag NPs.

Materials and Methods:

Thin films of Ag NPs with a fixed thickness of 4 nm were deposited on square silicon substrates via electron beam physical vapour deposition (PVD) in an ultra high vacuum (UHV) chamber. The silver pellets were at a purity of 99.99% purchased from Kurt J. Lesker. Silicon substrates were B dopped <100>, and 625 µm with 200 nm thermal oxide. The deposition rate of Ag material was adjusted at 0.1A/s, whereas the vacuum during deposition was roughly about ~10-6 Torr. Subsequently, samples were annealed at different temperatures of 500, 600, 700, and 800oC in a thermal tube furnace of argon inert atmosphere for 30 minutes. Characterizing of the samples, afterwards, was carried out thourgh surface morphology studies which were conducted using the atomic force microscopy (AFM) in conctat mode, provided by Agilant Technologies.

Results and Discussions

Thin films of Ag samples with varying temperatures (500, 600, 700, and 800 ^{o}C) were annealed following similar experimental procedure and conditions. Samples annealed under 500, 600, and 700 ^{o}C have shown clear

agglomeration when studied by AFM. On the other hand, samples annealed at 800 ^{o}C have shown clear NPs which is further discussed in this paper. To insure that the aglomeration issue is not a cause of sample contamination, we produced twenty samples of Ag thin-films with different cleaning scenarios of pre and post-annealing sonication at different set timings. This is to be further investigated and reported in future work.

For the 800^{o}C sample case, the surface morphologies of the as-deposited and annealed thin films with 4 nm thickness using the AFM are shown in Figure 1(a), and (b) respectively. These morphologies clearly reveal the formation of NPs in annealed films as a result of thermal exposure, whilst the as-deposited sample shows no obvious formation of the NPs. The roughness value in the as-deposited sample was 0.14 nm, whereas in the annealed sample it was 0.69 nm. The size of the Ag NPs has been analysed using the AFM, and the size disrtibution corresponding to annealed films is shown in Figure 2. For the 800^{o}C annealed sample, about 85% of the formed NPs have heights between 9.5 and 12.5 nm reflecting a uniform formation of the NPs by PVD and annealing processes. NPs were about 400 nm apart in average compared to the very smooth surface of the unannealed sample. The average size in terms of the Ag NPs diameters has ranged between 50 to 100 nm.

Strickingly, the maximum reached height of the Ag NPs exceeds, by a factor of 3, the deposited thickness of 4 nm. This might be referred to the temperature variation at the film surface in addition to the temperature intensity. Morover, the thermal distribution on the film surface which is carried out by multiple thermal waves inside the thermal tube could be another factor contributing to the measured difference bwteen the deposited thickness and the maximum NPs height. This is defined in litreture as Marangoni convection which starts to act on the thin film after the temperature gradiant appears in a confined area [4]. This indicates that the average nanoparticle diameter and height mostly depends on the film thickness after introducing it to the thermal source.

When observing the growth of Ag NPs, during annealing at a lower temperature deposited Ag atoms and smaller Ag NPs agglomorate. This leads to the formation of larger NPs and more condensed films. As the annealing temperature is increased, the NPs grow in size because of the enhanced surface diffusivity of Ag and expand in diameter even more leading to larger separation distances between the particles. Furthermore, this phenomena can be related to the thermal conductivity of the Ag, which has a value of 429W/m K. High thermal conductivity value leads Ag to interact more with annealing thermal waves forming the NPs. In addition, the surface energy value of Ag ~ 890 mJ/m^2, which is also known as surface tension, affects the adhesion of the metallic particles and their physical interaction with the Si substrates.

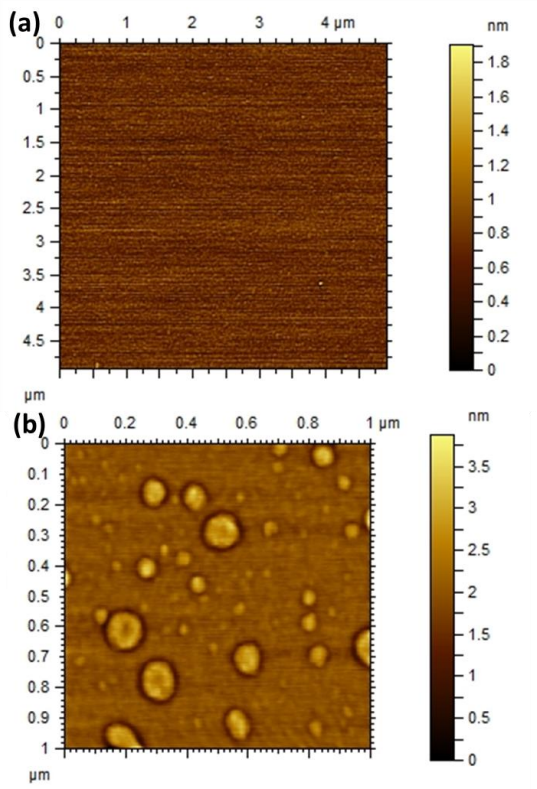

Figure 1: Atomic force microscopy topography of: (a) as-deposited Ag thin film (b) 1x1 µm surface annealed Ag films at 800^{o}C for 30 minutes in inert atmosphere.

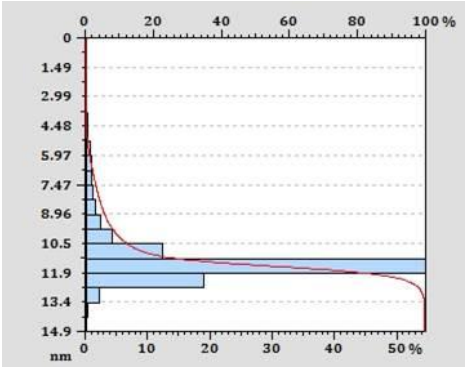

Figure 2: Size distribution in percentages of Ag NPs analyzed from the AFM topography

Conclusions:

We, in this work, were successfully able to produce ultrathin film of Ag NPs at a thickness of 4 nm via the electron beam PVD. Thermal

annealing has shown the ability to form NPs, that can be obviously observed at the AFM images, which vary in diameters as the set annealing temperature changes. The higher the annealing temperature, the more separated the nanoparticles formed. Additionally, it was observed that the hieght of Ag NPs were formed have exceeded the fabricated film thickness, which is referred to the Marangoni convection theory. Morphology studies were conducted as well as distribution of nanoparticles.

Acknowledgment:

Support is received by the Kuwait Institute for Scientific Research (KISR) and project (P-KISR-06-04 Kuwait Government). The financial support was received from KFAS for getting this work published.

References:

[1] Clavero, C. (2014). Plasmon-induced hot-electron generation at nanoparticle/metal-oxide interfaces for photovoltaic and photocatalytic devices. Nature Photonics, 8(2), 95-103.

[2] Jain, P. K., Huang, X., El-Sayed, I. H., & El-Sayed, M. A. (2007). Review of some interesting surface plasmon resonance-enhanced properties of noble metal nanoparticles and their applications to biosystems. Plasmonics, 2(3), 107-118.

[3] Mishra Y. K., Mohapatra S., Kabiraj D., Tripathi A., Pivin J. C., & Avasthi D. K. (2007). Growth of Au nanostructures by annealing elevtron beam evaporated thin films. Pure and Applied Optics 9, S410-S414.

[4] Ratautas, K., Gedvilas, M., Voisiat, B., Raciukaitis, G., & Grigonis, A. (2012). Transformation of a thin gold film to nanoparticles after nanosecond–laser irradiation. J. Laser Micro/Nanoeng, 7, 355-361.

Solvothermal hot injection synthesis of AgNi nanoalloy

Vit Vykoukal[1], Jiri Bursik[2], Pavla Roupcova[2], Jiri Pinkas[1*]

[1] Masaryk University, Faculty of Science, Department of Chemistry, Kotlarska 2, 611 37 Brno, Czech Republic

[2] Institute of Physics of Materials, ASCR, Zizkova 22, 616 62 Brno, Czech Republic

Abstract:

Nanomaterials and especially their preparation by chemical approach is a very active field of materials research. The synthesis of nanoalloys is one integral part of nanoscience and development of efficient methods is a challenging task due to their chemical, phase, and morphological variability. In case of metal nanoalloys we can observe many interesting properties such as depression of melting point,[1,2] plasmon resonance,[3,4] catalytic activity,[5] and phase separation.[6] Nanoalloys can be prepared by many approaches, but highly advantageous is the solvothermal synthesis, specifically in oleylamine.[5,7] The hot injection technique appears to be the best for ensuring homogeneous conditions for nanoparticles nucleation and growth.

AgNi nanoparticles were prepared by injection of an oleylamine solution (4 cm^3) of $AgNO_3$ and $Ni(acac)_2$ (different molar ratios, 4 mmol total amount) to a mixture of oleylamine (16 cm^3) and octadecene (20 cm^3) at 230 °C. After 10 minutes, the reaction mixture was cooled down to room temperature in a water bath. Then 20 cm^3 of acetone was added to precipitate nanoparticles and the suspension was centrifuged. The precipitate was washed by a mixture of hexane and acetone (1:3 volume ratio). This procedure was repeated twice and finally the precipitate was dispersed in hexane and characterized.

Dynamic Light Scattering (DLS), Transmission Electron Microscopy (TEM), Elemental analyses (ICP OES), and Small-Angle X-ray Scattering (SAXS) analyses were performed for determination of chemical composition, average size, size distribution, and shape of the prepared nanoparticles. Plasmon resonances were observed and we found that the intensity of plasmon resonance was dependent on the molar ratio of AgNi in the particles. HT-XRD was carried out and we observed a phase separation in the prepared nanoalloy. Magnetic properties and their dependence on temperature were also characterized and the results are in a good agreement with the HT-XRD characterization.

Keywords: nanomaterials, nanoalloy, silver, nickel, DLS, SAXS

Introduction:

Nanomaterials and especially their preparation by chemical approach is a very active field of materials research. The synthesis of nanoalloys is one integral part of nanoscience and development of efficient methods is a challenging task due to their chemical, phase, and morphological variability. In case of metal nanoalloys we can observe many interesting properties such as depression of melting point,[1,2] plasmon resonance,[3,4] catalytic activity,[5] and phase separation.[6] Nanoalloys can be prepared by many approaches, but highly advantageous is the solvothermal synthesis, specifically in oleylamine.[5,7] The hot injection technique appears to be the best for ensuring homogeneous conditions for nanoparticles nucleation and growth.

We used the hot injection method to prepare AgNi alloy nanoparticles from simple precursors $AgNO_3$ and $Ni(acac)_2$ in oleylamine and octadecene at 230 °C and characterized them by DLS, SAXS, and TEM techniques.

Synthesis:

For a typical synthesis $Ni(acac)_2$ (Aldrich) and $AgNO_3$ (different ratios, total amount 4 mmol) were put to Schlenk flask. Schlenk cyclus was carried out three times and then dry oleylamine (4 cm^3, 80–90% Aldrich) was added. Mixture was heated in an oil bath to 85 °C. Oleylamine (16 cm^3) and 1-octadecene (20 cm^3, 90% Aldrich) were put into a three neck Schlenk flask and were heated to 120 °C under reduced pressure to remove residual water and oxygen. After 20 minutes vacuum was exchanged for

nitrogen atmosphere and temperature was increased to 230 °C. The precursor solution was rapidly injected to mixture of solvents. After 10 minutes, the reaction mixture was cooled down to room temperature in a water bath. Then 20 cm^3 of acetone was added and the mixture was centrifuged. Acetone was added to increase the yield, because after acetone addition aggregates arise and these aggregates are easily dispersible in hexane. The precipitate was washed with a mixture of hexane and acetone (1:3 volume ratio). This procedure was repeated twice and finally the precipitate was dispersed in hexane and characterized.

Results and Discussions

Dependency of nanoparticle sizes on their composition was studied by using DLS technique. This characterization method provides tree types of results which can be used for description of prepared nanoparticles. Samples must be free of aggregates, impurities and dust, because their presence can highly distort results. Syringe filtration and sedimentation were used for removing of distorting influences. Results are summarized in

Table 1. Composition of nanoparticles was established by ICP-OES analyses. Every DLS result is an average of three measurements. Z-Average and PdI are mentioned only when software marked them as satisfactory. When PdI is lower than 0.1 sample can be considered as monodisperse. Z-Average as one of the results from DLS characterization can be used for comparison with other characterization techniques such as SAXS. This comparison is summed up in **Table 2**. The model of average nanoparticle can be calculated on the basis of SAXS data, see **Figure 1**.

Table 1: DLS characterization of AgNi nanoalloys with different compositions

Ag (mol%)	11	18	32	41	49	59	60	63	73	75	83
$\bar{x}$ (d = nm)	28	33	27	27	25	34	30	27	28	29	27
Z-Aver. (d = nm)	28	28	25	26	23	28	28	25	25	31	25
PDI	0.253	0.194	0.092	0.225	0.069	0.194	0.073	0.067	0.099	0.293	0.074

Table 2: Z-Average and SAXS results comparison

Ag mol%	32	41	49	59	63	73	83
Z-Average (d = nm)	25	26	23	28	25	25	25
SAXS	15.2	34.3	40.9	21.9	38.4	23.2	15.3

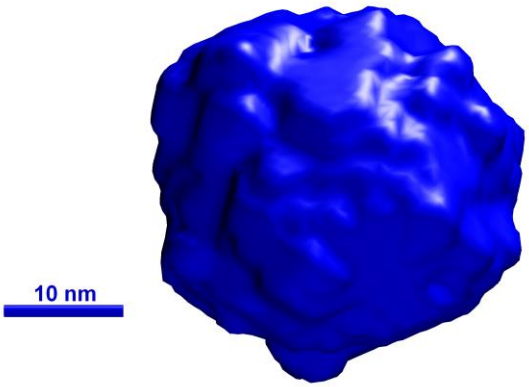

Figure 1: SAXS model of AgNi nanoalloy (Ag 73 mol%)

Size, shape and dispersity of prepared nanoalloys with different compositions were characterized also by the TEM method. Figures of nanoparticles were analyzed by ImageJ software and histograms of nanoparticle diameters were obtained (see **Figure 2** and **Figure 3**). The results are in good agreement with DLS characterization. Weighted averages of nanoparticle diameters are smaller according to TEM characterization, because the method observes only metal core of nanoparticles, unlike DLS technique which observes hydrodynamic diameters, i.e. metal cores with organic layers on the surfaces of nanoparticles.

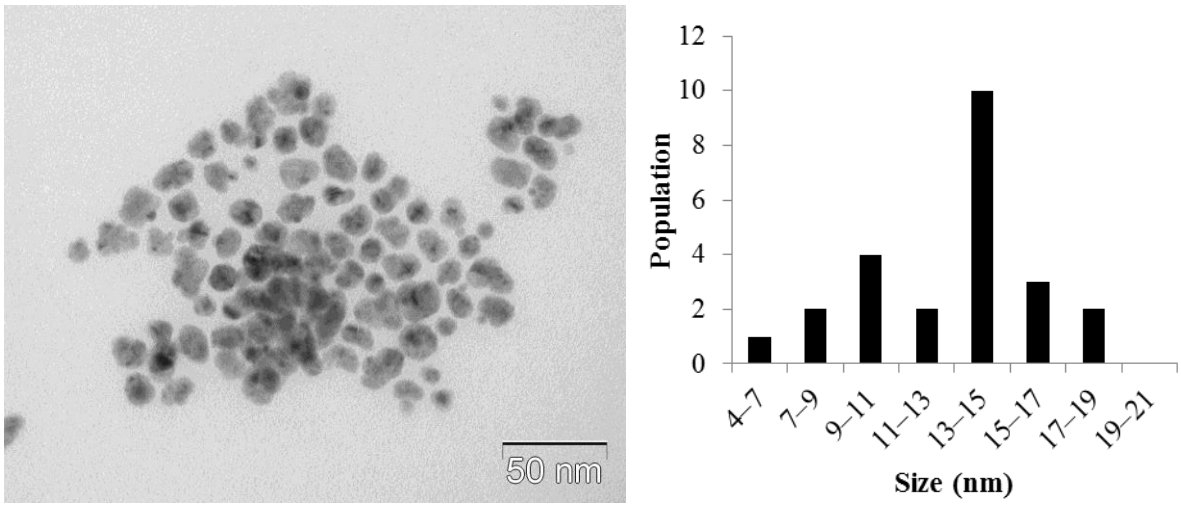

Figure 2: TEM analysis of AgNi nanoalloy (Ag 19 mol%) $\bar{x}$ = 13.9 nm

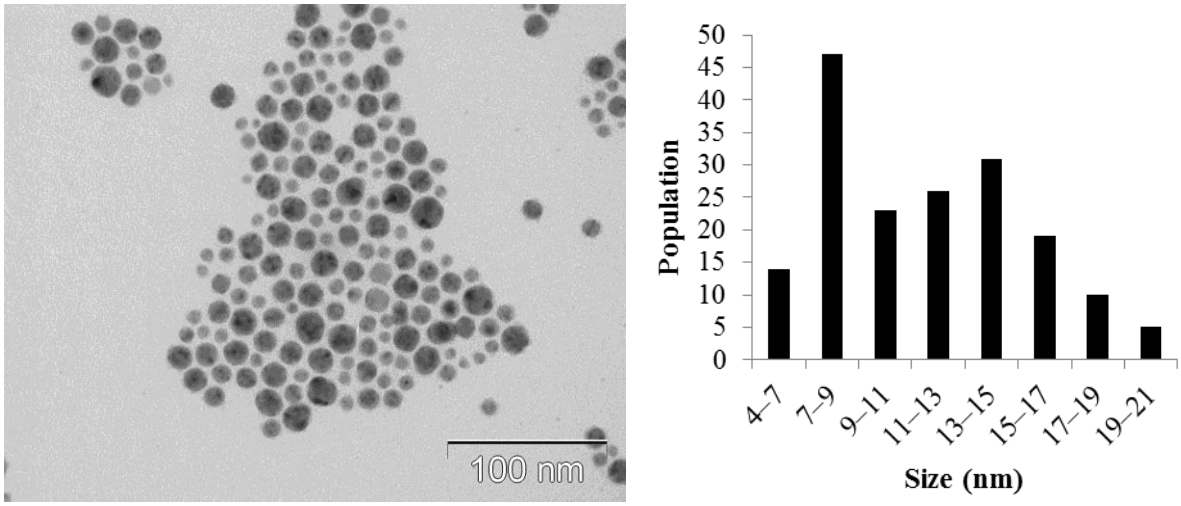

Figure 3: TEM analysis of AgNi nanoalloy (Ag 83 mol%) $\bar{x}$ = 12.5 nm

Conclusions:

AgNi nanoalloys were synthesized with variable composition by the solvothermal hot injection technique using very common precursors in a mixture of oleylamine and 1-octadecene. Prepared nanoparticles were characterized by DLS, SAXS, and TEM focused to size, shape, and distribution. The results were mutually compared. We have found that size, shape, and distribution do not depend on nanoparticle composition. Distribution of sizes is relatively narrow.

Acknowledgements:

This research has been financially supported by the Czech Science Foundation under the project ‘‘Stability and phase equilibria of bimetallic nanoparticles’’ (GA14-12653S) and the Ministry of Education, Youth and Sports of the Czech Republic under the project CEITEC 2020 (LQ1601). Authors thank the X-ray Diffraction and Bio-SAXS Core Facility of CEITEC and the Structural Analysis Laboratory of Central European Institute of Technology CEITEC – CEITEC Nano project (LM2015041), funded by the MEYS of the Czech Republic under the activity „Projects of major infrastructures for research, development and innovations”.

References:

(1) Zou, C.; Gao, Y.; Yang, B.; Zhai, Q. *J. Mater. Sci.: Materials in Electronics* **2009**, *21* (9), 868–874.

(2) Jiang, H.; Moon, K.; Hua, F.; Wong, C. P. *Chem. Mater.* **2007**, *19* (18), 4482–4485.

(3) Link, S.; El-Sayed, M. A. *Annu. Rev. Phys. Chem.* **2003**, *54*, 331–366.

(4) Gonzalez, C. M.; Liu, Y.; Scaiano, J. C. *J. Phys. Chem. C* **2009**, *113* (27), 11861–11867.

(5) Zhang, Y.; Huang, W.; Habas, S. E.; Kuhn, J. N.; Grass, M. E.; Yamada, Y.; Yang, P.; Somorjai, G. A. *J. Phys. Chem. C* **2008**, *112* (32), 12092–12095.

(6) Sopousek, J.; Zobac, O.; Bursik, J.; Roupcova, P.; Vykoukal, V.; Brož, P.; Pinkas, J.; Vrestal, J. *Phys. Chem. Chem. Phys.* **2015**.

(7) Sopousek, J.; Pinkas, J.; Broz, P.; Bursik, J.; Vykoukal, V.; Skoda, D.; Styskalík, A.; Zobac, O.; Vrestall, J.; Hrdlicka, A.; Simbera, J. *J.Nanomaterials* **2014**, *2014*, 1–13.

Exact solution for the axial pressure drop in cylindrical isothermal channels with Maxwell slip flow

A. C. Hoffmann, M. Karakitsiou, B. Holst
Dept. of Physics and Technology, University of Bergen Allegaten 55, 5007 Bergen, Norway

Abstract

An Explicit expression for the axial pressure profiles in a cylindrical channel with Maxwell slip gas flow is derived and given in this paper. The resulting expression, which only involves the inlet and outlet pressures and the channel diameter, is given for use in modelling and design of MEMS and NEMS or for simulations of channel flows at Knudsen numbers in the range 10^{-3}–0.1. The expression is validated by deriving from it an expression for the channel mass flow, which is found to be identical to the known expression for the mass flow through cylindrical channels with Maxwell slip flow.

1 Introduction

An upsurge in the development of micro-and nanoelectromechanical devices has kindled renewed interest in the flow of fluids at moderately high Knudsen numbers through channels and crevices. In many modern design applications, e.g. MEMS and NEMS, micro- and nanoelectromechanical devices, it is necessary to characterize and model the flow in narrow channels. For this it is useful to know the pressure profile in channel flow at Knudsen numbers whereby the flow is in the Maxwell slip regime, since this is often the regime into which the flows in such devices fall in practise. It is therefore notable that expressions for the pressure profiles for Maxwell slip flow in channels, even of simple geometries, have not yet been published.

Arkilic et al. [1] derived an expression for the axial pressure profile in slip flow, based on a 2-D model and perturbation analysis applicable to a rectangular channel of very large aspect ratio, accurate to zeroth order. Gallis and Torczynsky [2] derived an expression for the pressure profile in channels in the slip flow regime based on a more advanced slip expression than the one of Maxwell but did not give an explicit solution.

In this paper an explicit expression for the axial pressure profiles in a cylindrical channel is derived directly from first principles. Since there is nothing in the functional forms obtained below that will demand that the variables are non-dimensionalized, the derivations will be done in terms of the physical, dimensional variables themselves.

2 Pressure profile

A standard momentum balance on an element differential in the axial direction to analyze laminar pipe flow, with a no-slip wall boundary condition, results in [3]:

$$\frac{dp}{dz} = -\frac{2}{r}\left(-\mu\frac{du}{dr}\right) \tag{1}$$

giving by integration:

$$\int_0^u du' = \frac{dp}{dz}\frac{1}{2\mu}\int_R^r r'\,dr' \tag{2}$$

The for Maxwell wall slip is ([4, 5]): $u_w = -\zeta\frac{du}{dr}\big|_{r=R}$ with $\zeta = \frac{\zeta_0}{p}$ and the factor $\frac{du}{dr}\big|_{r=R}$ evaluated from the no-slip solution. This results in:

$$\int_{-\zeta\frac{du}{dr}\big|_{r=R}}^u du' = \frac{dp}{dz}\frac{1}{2\mu}\int_R^r r'\,dr' \tag{3}$$

giving:

$$u + \zeta\frac{du}{dr}\bigg|_{r=R} = -\frac{dp}{dz}\frac{1}{4\mu}\left(R^2 - r^2\right). \tag{4}$$

From the no-slip DE, (1):

$$\frac{du}{dr} = \frac{r}{2\mu}\frac{dp}{dz} \quad \Rightarrow \quad \frac{du}{dr}\bigg|_{r=R} = \frac{R}{2\mu}\frac{dp}{dz} \tag{5}$$

Roy et al. [6] and others give $\zeta = \frac{2-\sigma_V}{\sigma_V}\lambda$. σ_V is the momentum accommodation coefficient [7] and in general depends on the nature of the gas, the channel wall material and the Knudsen number. In many cases $\sigma_V \approx 0.8$ ([7, 8]), λ is the mean free path in the gas. Filling in, this makes the solution for u, the gas velocity:

$$u = -\frac{dp}{dz}\frac{1}{4\mu}\left(R^2 - r^2\right) - \frac{2-\sigma_V}{\sigma_V}\lambda\frac{R}{2\mu}\frac{dp}{dz}. \quad (6)$$

The mass flow, $\dot{m}_t = \int_0^R \rho u 2\pi r\, dr$, becomes:

$$\dot{m}_t = -\frac{\pi\rho R^3}{8\mu\sigma_V}\left(4\lambda(2-\sigma_V) + \sigma_V R\right)\frac{dp}{dz}.$$

$\rho = \frac{pM}{\mathbb{R}T} = \frac{pm}{k_B T}$ where M and m are the molar and molecular masses, $\mathbb{R}$ the universal gas constant, k_B the Boltzmann constant and $\lambda = \frac{k_B T}{\sqrt{2}\pi d^2 p}$ ([5]), with d the molecular collisional diameter, is the mean free path in the gas, giving for the mass flow,$\dot{m}_t$:

$$-\frac{\pi p m R^3}{k_B T\, 8\mu\sigma_V}\left(4\frac{k_B T}{\sqrt{2}\pi d^2 p}(2-\sigma_V) + \sigma_V R\right)\frac{dp}{dz}$$

which can be rewritten to:

$$\dot{m}_t = A\frac{dp}{dz} + Bp\frac{dp}{dz} \quad (7)$$

where, after simplification,

$$A = -\frac{mR^3(2-\sigma_V)}{\sqrt{8}d^2\mu\sigma_V} \quad \text{and} \quad B = -\frac{\pi m R^4}{8\mu k_B T}. \quad (8)$$

$0 \leqq \sigma_V \leqq 1$, is the fraction of molecules or atoms undergoing diffuse, rather than specular, reflection at the wall ([2, 8]), so that both A and B are negative.

Equation (7) is a differential equation for $p(z)$, and can be solved as a boundary value problem. A standard, first-principles, steady-state mass balance on an element, which spans the channel cross-section and is differential in the z-direction, gives after rearrangement:

$$(A + Bp)\frac{d^2p}{dz^2} + B\left(\frac{dp}{dz}\right)^2 = 0, \quad (9)$$

There are two solutions to this equation. Taking the positive one as the one satisfying the boundary conditions at the ends of the channel gives the following expression for the pressure as a function of axial position in the channel, $p(z)$:

$$-\frac{A + \sqrt{(A+Bp_0)^2 - \frac{B(p_0-p_L)(2A+B(p_0+p_L))z}{L}}}{B} \quad (10)$$

satisfying the end boundary conditions. This profile is quite non-linear, similar to Poiseuille flow, in the low-Kn range of the Maxwell slip and becomes progressively more linear at higher Kn, which is reasonable.

This solution makes it possible to study the effects of the governing variables, such as the accommodation coefficient as shown in Fig.1.

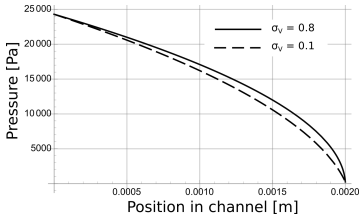

Figure 1: Pressure profiles for slip flow in a cylindrical channel with diameter 325 μm, effect of the accommodation coefficient.

References

[1] E. B. Arkilic, M. A. Schmidt, and K. S. Breuer. Gaseous slip flow in long microchannels. *Journal of Microelectromechanical Systems*, 6:167–178, 1997.

[2] M. A. Gallis and J. R. Torczynsky. DSMC-based expression for the gas mass flow rate and pressure profile in a microscale tube. *Physics of Fluids*, 24:012005–1–012005–21, 2012.

[3] W. L. McCabe, J. Smith, and P. Hariott. *Unit operations of chemical engineering*. McGraw-Hill, London, 7 edition, 2004.

[4] W. G. Pollard and R. D. Present. On gaseous sefdiffusion in long capillary tubes. *Physical Review*, 73:762–774, 1948.

[5] R. B. Bird, W. E. Stewart, and E. N. Lightfoot. *Transport phenomena*. John Wiley & Sons, New York, 2 edition, 2002.

[6] S. Roy, R. Raju, H. F. Chuang, B. A. Cruden, and M. Meyyappan. Modeling gas flow through microchannels and nanopores. *Journal of Applied Physics*, 93:4870–4879, 2003.

[7] G. Karniadakis, A. Beskok, and N. Aluru. *Microflows and Nanoflows. Fundamentals and Simulation*. Springer Verlag, New York, 2005.

[8] A. Roth. *Vacuum technology*. Elsevier Science B.V, Amsterdam, 1990.

Piezo-Resistive Sensing Active (PRSA) Probes integrated into a Nanomeasuring Machine (NMM-1)

A. El Melegy,[1,3,*] T. Hausotte,[1,] M. A. Younes,[2,] M. Amer[3]

[1]Friedrich Alexander University Erlangen-Nürnberg (FAU), Institute of Manufacturing Metrology (FMT), Erlangen, Germany
[2]Alexandria University, Faculty of Engineering, Alexandria, Egypt.
[3]National Institute for Standard (NIS), Engineering and Surface Metrology Laboratory (ESML), El Giza, Egypt.

Abstract:
Atomic force microscopes (AFMs) are instruments for the measurement of topographic surface features in the nanoscale. Nanoscale surface features are reconstructed through scanning the surface by silicon cantilevers The recent use of selfsensing and self-actuating cantilevers eliminated the need for the relatively bulcky optical deflection systems. To overcome the limitation on the measurement range, a new measuring system has been developed where a piezo-resistive sensing active (PRSA) cantilever is integrated into a nanomeasuring machine (NMM-1) which extends the lateral scanning area up to 25 mm × 25 mm with a vertical range up to 5 mm. The PRSA_AFM integrated system was successfully used for measuring two samples; a glass scale with a spacing of 8 µm and 100 nm feature height; and a calibration grid of 119 nm and 5 µm step height and width respectively. The integration, calibration and factors affecting the performance of the developed system have been investigated.

Keywords: Nanometrology, Atomic Force Microscopy (AFM), Self-Sensing Cantilevers, NanoMeasuring Machines (NMMs).

Introduction:
Surface features imaging and measurement is a major challenge especially in the nanoscale. One of the most versatile tools for surface measurement is the Atomic Force Microscope (AFM) [1]. It can image a wide range of various samples regardless of being conductive or noconductive, in vacuum, in air or in a fluid [6]. It depends on the interaction forces generated between the cantilever probe tip and the surface as the tip comes into a close proximity with the test surface. Conventionally, the AFM has a laser source, cantilever and optical readout photo-senstive device (PSD) [3]. As the cantilever scans across the test sample, the reflected laser beam which is focused into the upper surface of the cantilever draws surface features on the PSD readout. Despite its high sensitivity and precision, conventional AFMs have major drawbacks such as design complications, difficulty to precisely align optical components, limited throughput and small range[2,4,5].

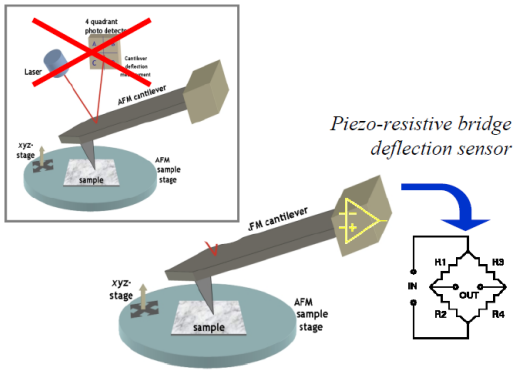

Figure 1: Self-sensing AFM cantilever in comparison to the conventional optical AFM [15].

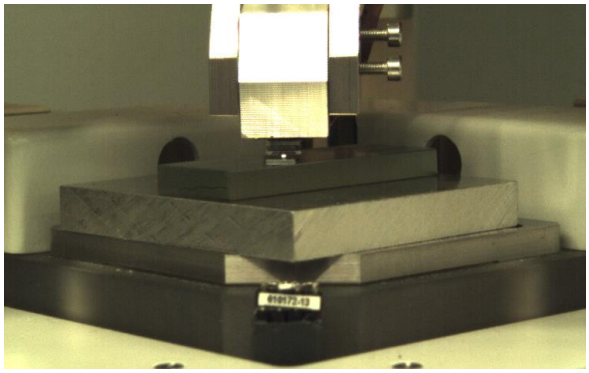

Figure 2: The PRSA_AFM integrated system is illustrated, Self-sensing cantilever is integrated into the NMM-1.

A briliant idea to simplify AFM construction has been the use of a self-sensing cantilever type, firstly done by Tortonese et.al. [7]. It depends on integrating a piezoresistor on the cantilever. Defelection in the cantilever causes a

corresponding change in the resistor resistance. The AFM design becomes more simple with no need for the optical units. It also facilitates the use of a parallel self-sensing cantilevers set in an automated operation which increases the throughput and saves the scanning time [8,9,13]. Thermal resistor actuators have recently been introduced to produce not only self-sensing but also selfactuating cantilevers [10,11,14]. Self-sensing cantilevers are applied in many applications including; data writing and reading, multi-probe, nantopographical imaging and nanostructure fabrication [12]. Self-sensing cantilevers can be easily integrated into electronic devices. In this a paper, a self-sensing thermal self-actuating PRSA cantilever [6] has been integrated into a Nano-Measuring Machine (NMM-1) to build a new type of metrological large range Atomic Force Microscopes for surface topography measurements. The PRSA_AFM integrated system has a range of 25mm × 25mm × 5mm. Nano features of a glass scale and a calibration grid have been measured using the new system. Calibration and factors affecting the performance of the integrated system are illustrated.

Instrumentation:

The main components of the PRSA_AFM integrated system are; PRSA cantilevers, AFM pre-amplifier box, mechnaical assembly, HF2 Lock-in amplifier and Nano-measuring machine (NMM-1). PRSA cantilevers are silicon cantilevers with integrated piezo resistors and thermal actuators for selfsensing and self-actuating scanning probe microscopy (SCL-Sensor.Tech. Fabrication GmbH). AFM Pre-Amplifier Box is designed at FMT-FAU institute to connect the small electronic PRSA_Preamplifier part to other system components, Figure 3. Mechanical assembly is designed and built at FMT-FAU Institute to integrate and install the setup of PRSA cantilevers into NMM-1, Figure 4. HF2 Lock-in Amplifier is a digital lock-in amplifier covering the frequency range between DC and 50 MHz. The signal to be measured is amplified to a defined range, filtered, and digitized at very high speed and sent directly to NMM-1. The lock-in amplifier one of the most important elements in this setup. It gives the operating signal (input signal) for tapping mode and digitizes the output signal from AFM cantilever and send it directly to the NMM-1. NMM-1 is used for three-dimensional coordinate measurement in a range of 25mm x 25mm x 5mm with a resolution of 0.1 nm (SIOS Meßtechnik GmbH). It has a unique sensor arrangement that provides Abbe error-free measurements on all three coordinate axes, Figure 5.

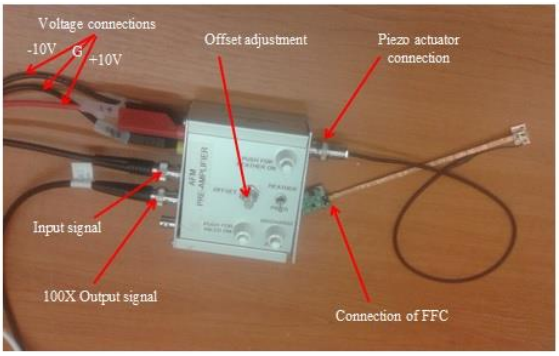

Figure 3: AFM Pre-Amplifier Box.

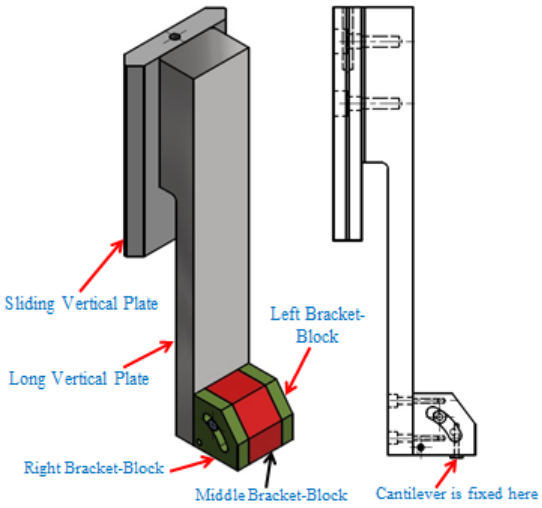

Figure 4: Mechanical assembly

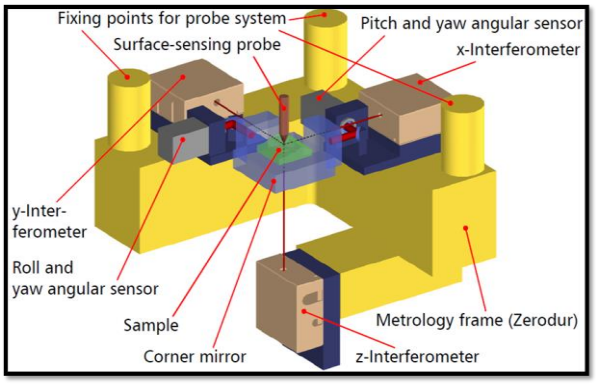

Figure 5: Schematic principle of the NMM. The detection point coincides with the intersection of three interferometer beams orientated in *x*, *y*, and *z* axes. The Abbe error is minimum.

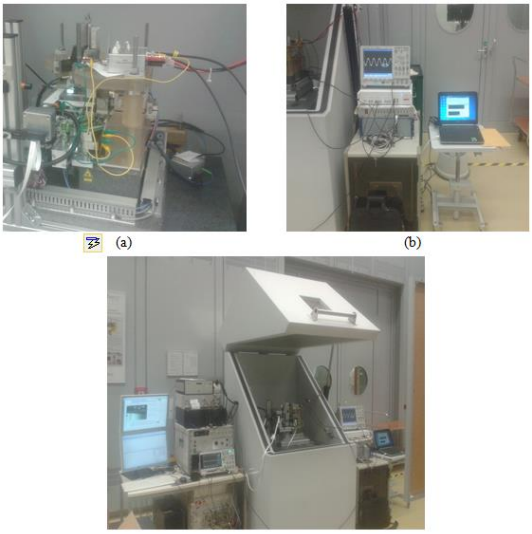

Figure 6: Experimental Setup for PRSA_AFM system.

Measurement Procedure:

The PRSA_AFM integrated system is used for tapping mode with thermal actuation. The cantilever is adjusted vertically at a stand off distance of approximately 300 nm from the test sample surface. Then, the cantilever is calibrated against the NMM-1 vertical axis in this range. The proper scanning speed is selected together with the appropriate NMM-1 control parameters. The system can be used either in linear or area scanning modes.

Results and Discussions:

The PRSA_AFM integrated system is intially calibrated against the NMM-1 before measurements. The output signal of the PRSA-AFM probe is compared against the NMM_Z axis reading. This facilitates the communications between the cantilever and the NMM and converts cantilever signal to units of length. The NMM stage is moved in z axis for a specified distance (usually 300 nm) twowards the AFM cantilever (forward direction, FWD) and then moved upward in opposite direction (backward direction, BWD), Figure7. The output signal of PRSA_cantilever in "mV" is calibrated against the z-axis of NMM-1 in nm. The NMM-1 reads the signal of AFM and converts its values into nanometer length units.

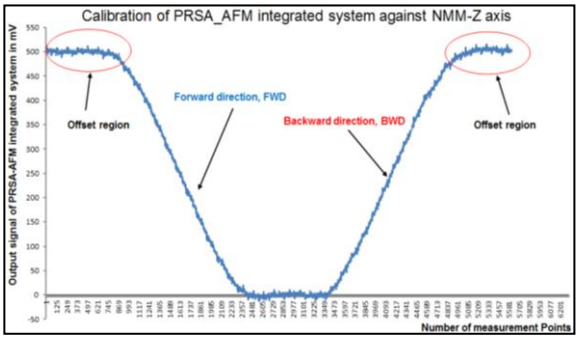

Figure 7: Calibration of PRSA_AFM integrated system against NMM-Z axis.

The PRSA-AFM developed system was used for line scanning at different speeds, Figures 8 and 9. When the scanning speed was increased from 1 µm/s to 10 µm/s and 25 µm/s, sharp spikes were observed in the recorded signal. Thorough investigation revealed the possibility of controlling these spikes by careful setting of the NMM-1Proportional–Integral–Derivative (PID) controller parameters (Kp and Kn).

An optimization procedure was performed using a full factorial design of experiments to select the most appropriate values of the two parameters K_p and K_n to supress the spikes observed at high speeds. The test samples used in the experimental analysis are a Glass Scale of 99 nm step height and 16 µm periodicity; and a Calibration Grid of 119 nm step height and 10 µm periodicity. Step height and periodicity are measured three times for both samples at all possible ettings of K_p and K_n.

Table (1) shows levels of both Kp and Kn used in this study. The experimental analysis was performed at a tapping amplitude of 1200mVpp and a scan speed of 25 µm/s.

Table (1) Levels of Kp and Kn used in the study.

K_p	K_n
25	0.05
50	0.10
75	0.15
100	0.20
125	0.25
150	0.30
	0.35
	0.40

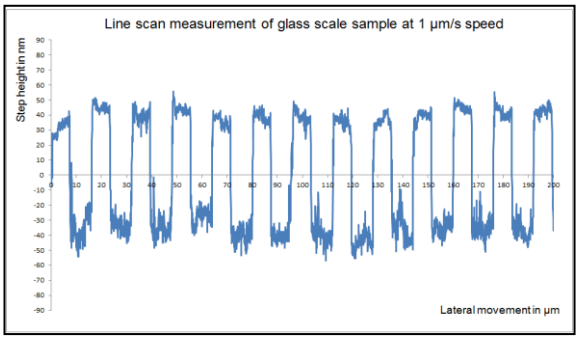

Figure 8: Recorded signal of the glass scale sample at a scan speed of 1 µm/s.

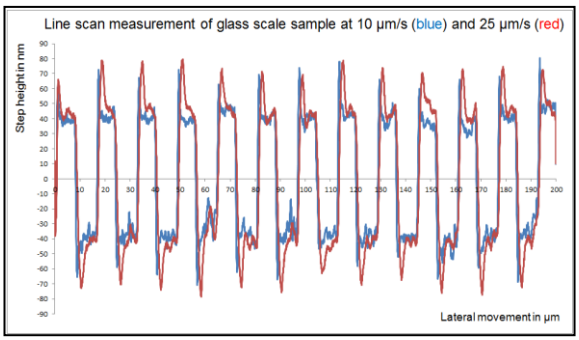

Figure 9: Recorded signal of the glass scale sample at scan speeds of 10 µm/s (blue) and 25 µm/s (red).

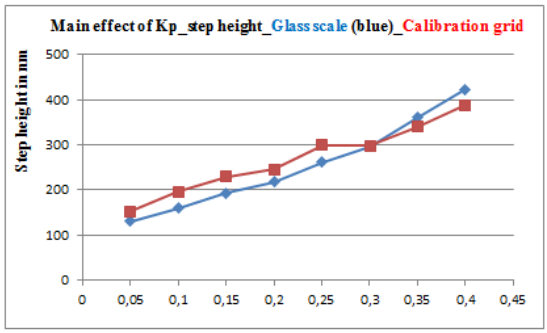

(a)

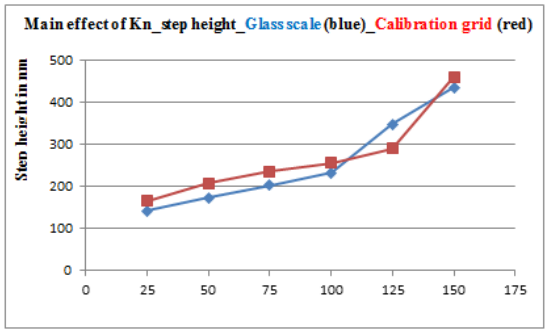

(b)

Figure 10: Main effects of Kn and Kp on the measured values of the step height (a) Kp (b) Kn

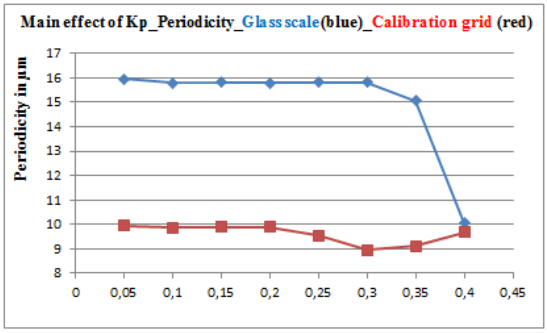

(a)

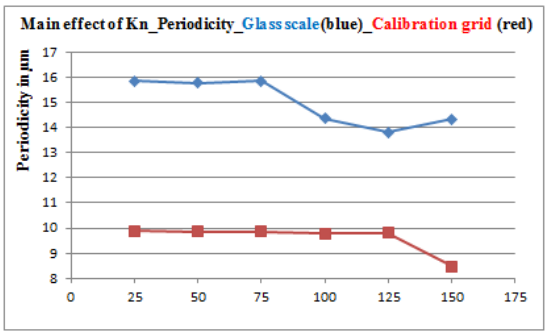

(b)

Figure 11: Main effects of Kn and Kp on the measured values of the periodicity (a) Kp (b) Kn

Figures 10 and 11 show the main effects of both K_p and K_n on the estimated average step height and periodicity for either glass scale and calibration grid samples. It is obvious that the error in the measured values of either step height or periodicity increases by increasing both K_p and K_n. The results suggest that the values of 25 for Kn and 0.05 for Kp give minimum error in the measurement results.

Conclusions and Outlook:

The PRSA_AFM system is integrated into a Nano Measuring Machine (NMM-1). It has a large range of 25 mm × 25 mm × 5 mm. The integrated system is calibrated against the Z axis of NMM that the output signal of PRSA cantilever can be converted into unit of length. The PID controller has the main effect on NMM at high speed. To get the minimum measurement error especially at high speeds up to 25 µm/s, the parameters of PID controller of Kp and Kn have to be used at Kp 0.05 and Kn 25. The PRSA_AFM integrated system has a capability to measure precisely at nanoscale.

Acknowledgments
The authors would like to thank the technical team in FMT institute in FAU Erlangen-Nürnberg University. Special thanks are for Mrs Ute Klöpzig for her effort in designing and manufacturing of the Pre-amplifier AFM box.

References:

1. Gaoliang Dai, Wolfgang Häßler-Grohne, Dorothee Hüser, Helmut Wolff, Hans-Ulrich Danzebrink, Ludger Koenders, and Harald Bosse, (2011) Development of a 3d-afm for true 3d measurements of nanostructures, *Measurement science and technology*, 22:094009(10pp).
2. Gaoliang Dai, Frank Pohlenz, Hans-Ulrich Danzebrink, Min Xu, Klaus Hasche, and Günter Wilkening, (2004) Metrological large range scanning probe microscope, *Review of scientific instruments*, 75(4).
3. Michael Leitner, Georg E. Fantner, Ernest J. Fantner, Katerina Ivanova, Tzvetan Ivanov, Ivo Rangelow, Andreas Ebner, Martina Rangl, Jilin Tang, and Peter Hinterdorfer, (2012) Increased imaging speed and force sensitivity for bio-applications with small cantilevers using a conventional afm setup, *Micron*, 43(12):1399–1407.
4. Nataliya Vorbringer-Dorozhovets, Tino Hausotte, Eberhard Manske, Jing-Chung Shen, and Gerd Jäger, (2011) Novel control scheme for a high-speed metrological scanning probe microscope, *Meas. Sci. Technol.*, 22:094012 (7pp).
5. Jian Zhao, Tong Guo, Long Ma, Xing Fu, and Xiaotang Hu, (2011) Metrological atomic force microscope with self-sensing measuring head, *Sensors and Actuators A: Physical*, 167(2):267–272.
6. G E Fantner, W Schumann, R J Barbero, A Deutschinger, V Todorov, D S Gray, A M Belcher, I W Rangelow and K Youcef-Toumi, (2009) Use of self-actuating and self-sensing cantilevers for imaging biological samples in fluid, *Nanotechnology* 20 434003 (10pp).
7. M. Tortonese, H. Yamada, R. C. Barrett, and C. F. Quate, (1991) Atomic Force Microscopy Using A Piezoresistive Cantilever, *IEEE*, 448 – 451.
8. S. C. Minne, S. R. Manalis, and C. F. Quate, (1995) Parallel atomic force microscopy using cantilevers with integrated piezoresistive sensors and integrated piezoelectric actuators, *Appl. Phys. Lett.* 67 (26), 1995.
9. S. C. Minne, G. Yaralioglu, S. R. Manalis, J. D. Adams, J. Zesch, A. Atalar, and C. F. Quate' (1998) Automated parallel high-speed atomic force microscopy, *Appl. Phys. Lett.*, Vol. 72, No. 18.
10. Teodor Gotszalk, Piotr Grabiec, Ivo W. Rangelow, (2000) Piezoresistive sensors for scanning probe microscopy, *Ultramicroscopy* 82 (39-48).
11. J. Thaysen, A. Boisen, O. Hansen, S. Bouwstra, (2000) Atomic force microscopy probe with piezoresistive read-out and a highly symmetrical Wheatstone bridge arrangement, *Sensors and Actuators* 83 (47–53).
12. William P. King, Thomas W. Kenny, and Kenneth E. Goodson, Graham Cross, Michel Despont, Urs Du¨ rig, Hugo Rothuizen, Gerd K. Binnig, and Peter Vettiger, (2001) AFM cantilevers for combined thermomechanical data writing and reading, *Appl. Phys. Lett.*, Vol. 78, No. 9.
13. Teodor Gotszalk, Piotr Grabiec, Ivo W. Rangelow, (2003) Calibration and examination of piezoresistive Wheatstone bridge cantilevers for SPMs, *Ultramicroscopy* 97 (385–389).
14. Zunxian Yang, Xinxin Li, Yuelin Wang, Haifei Bao, Min Liu, (2004) Micro cantilever probe array integrated with Piezoresistive sensor, *Microelectronics Journal* 35 (479–483).
15. DI Alexander Deutschinger (2013), Electric Self-Sensing Cantilevers SCL, Poster, *http://www.sclsensortech.com/fileadmin/content/2013-02-13_Poster_Winterschool_self-sensing_CLs.pdf*

Legal Metrology Framework for Nanotechnology in Australia

Sheila Devasahayam
Macquarie University, Sydney, NSW 2109 Australia

Abstract:

This work explores the feasibility of legal metrology (LM) as a platform to address the impact of nanotechnology (NT) on legal and social-economic aspects for NT and the associated benefits and risks.

Keywords: legal metrology, national measurement system, nanotechnology, regulatory regimes, nanometrology

Introduction:

There is a general consensus for an internationally integrated Nanotechnology (NT) governance due to the current fragmented regulatory regimes for NT world wide. It is expected Legal metrology (LM) as a platform can fill the gap. Legal metrology (LM) objectives aligns with International Organisation of Legal Metrology (OIML)'s objectives on global harmonisation of regulations and measurements. It is neither exclusive to measurement ranges eg. macro, micro, meso, nano, nor to specific technologies, eg, space and biotechnologies.

Methods:

The international harmonization is achieved through CIPM MRA (a guarantee of competence and of valid testing and examination results on the basis of OIML Recommendations) and OIML MAA(International equivalence of measurements: Mutual Recognition Arrangement). LM integrates with Metre convention and International Laboratory Accreditation Cooperation (ILAC) to deliver a global measurement system.

The Commonwealth Government in Australia gives effect to International treaty obligations, the Metre Convention, 1947 (The Metre Convention established the structure and processes through which we obtain world-wide uniformity in measurement, firstly through the use of a harmonised set of units of f measurement, the International System of Units (SI), and secondly through recognised means of establishing measurement standards that realise these units, described by the International Bureau of Weights and Measures (BIPM)) and the OIML convention, 1959 with respect to measurement under the National Measurement Act 1960 (Cth) through National Measurement Institute (NMI).

LM is the application of legal requirements to measurements and measuring instruments,comprising all measurements carried out for any legal purpose including measurements in the areas of health and safety Environment (HSE), law & trade.

TheLM is founded on the key principles of metrology, the measurement traceability and confidence in measurements (Peggs 2005), at whatever accuracy and for whatever physical quantity, and to ensure the measurements are expressed in legal units with known uncertainties.

The national measurement system in Australia, ensures that measurements can be made on a consistent basis throughout the country and are linked to the International System of Units (SI) and ensures technical,legal and international traceability. This is achieved through the hierarchy of standards by which physical measurements can be related back through the national metrological pyramid to the relevant SI units.

The National Measurement Act (The Act) prescribes that 'Australian legal units of measurement (ALUM) of a physical quantity are the sole legal units of measurement of that physical quantity'in addition to establishing a framework for the regulation of measuring instruments providing specifications for pattern approval and verification. The National Measurement Regulations 1999(Cth) provides details on the application of the Act and prescribes the ALUM. The NMI in Australia, in addition to in addition to coordinating Australia's measurement system, also develops and maintains standards of measurement, reference materials and reference techniques.

Discussions:

A LM Framework (LMF) in Australia is as depicted in Figure 2, executed through:

- National Measurement Act 1960 (Cth)
- ALUMS
  - Which reflect SI units into Australian law
  - Recognised as the sole units of measurement for physical quantities
- Verification ALUMS, via
  - Standards of measurement
  - Certified measuring instruments
  - Australian certified reference materials
  - Combination of one or more above.

The LMF accords legal status to the measurements through its certification, verification / reverification, uniform test procedures and accreditation programmes to ensure confidence

and integrity of the measurement systems. It ensures that measurements are what they purport to be thus satisfying Australia's international obligation and Australian law (Birch 1998., Brittain, 2013). The LMF (Figure 1) is directly linked to the Australian measurement system.

The LMF, however needs to be developed in conjunction with the nanometrology group in Australia, responsible for developing measurement infrastructure and standards for the NT. The challenges of nanometrology are for the measurements to be expressed in legal units and the measurement errors to be known with specified probability and comparable to the interatomic distances and to be able to measure any property in three dimensions at the nanometre scale. Many measurements are effective in two dimensions (or 2½ dimensions) and there is generally a trade off between measurement sensitivity & spatial resolution. In addition different techniques measure and operate on different principles and do not cover the full range of measurement values. Some measurement problems fall between the ranges of available instruments where there is no overlap.

The use of scanning probe microscopy (spm) allows measurements and imaging at a nanoscale.The traceability for metrological spm and interferometermeters is established using lasers whose frequency is traced back to to SI-unit meter (Petr Klapetek, 2013, Miles, 2010). Thesy are used to calibrate standards for flatness, step height standards and fiffractometers for1D or 2D grating. These calibrated standards are subsequently used to calibrate the secondary instruments maintained by the NMI and the user instruments. When the traceability chain is accompanied by the ceritification program offered under the LMF under the provisions in National Measurement Regulations as shown in Figure 2, it offers measurement confidence and traceability for nanodimenional measurements.

Conclusions:

A Legal Metrology Framework for Nanotechnology can ensure

- uniform and accurate methods of NT measurement across Australia and internationally.
- agreed level of transparency in the measurement.
- reduced transaction costs and trade barriers.
- promote confidence that measurements are what they purport to be.
- settle legal disputes.
- can be applied equally throughout the product lifecycle of manufactured nanoparticles.

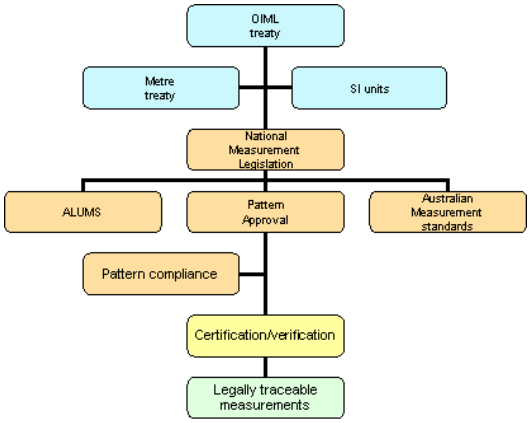

Figure 1: Legal Metrology Framework

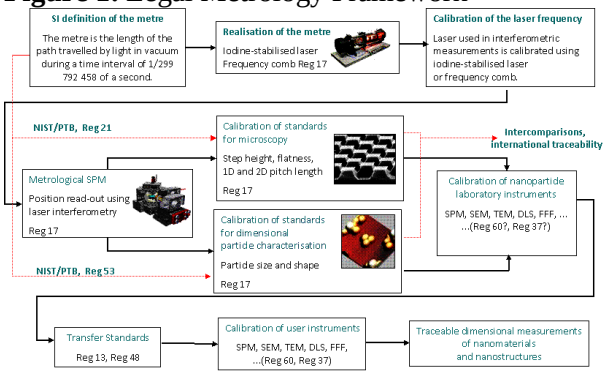

Figure 2: LMF for traceability of nano-scale dimensional measurements in Australia:

References:

1. Peggs, G.N, Measurement in the nanoworld, Nanotechnology Perceptions, 1, 2005, 18–23.
2. Birch, J. Metrological Control of Measuring Instruments, Leaflet 26, 1998.
3. Brittain, R, Australian National Speed Measurement Program: Technology, Type Approval, Verification, OIML TC7/SC4 NIST 16-18 July 2013.
4. Petr Klapetek, 2013, Dimensional Measurements, Chapter 5 in Quantitative Data Procesing in Scanning Probe Microscopy-SPM applications for Nanometrology, Elsevier, Oxford, UK.
5. Miles, J, 20130, , Nanotechnology work health and safety symposium, Sep 9-10, 2010.

Conjugated Polyrotaxanes: A Critical Assessment of Photophysical Properties in Correlation with the Effect of the Nature of Host Molecules Encapsulation

A. Farcas,[1*] A.-M. Resmerita,[1] P.-H. Aubert[2]

[1] ''Petru Poni'' Institute of Macromolecular Chemistry, Iasi, Romania
[2] Laboratoire de Physicochimie des Polymères et des Interfaces, Institut des Matériaux, Université de Cergy-Pontoise, France

Abstract:
We report the influence of the nature of the host molecules on the photophysical properties of poly(9,9-dioctylfluorene-*alt*-bithiophene) (PF-BT) copolymers. **1·RM-βCD**, **1·TM-βCD**, **1·TMS-βCD** and **1·CB7** polyrotaxanes have been synthesized by Suzuki cross-coupling of 5,5'-dibromo-2,2'-bithiophene (**BT**) inclusion complexes in randomly methylated β-cyclodextrin (RM-βCD), 2,3,6-tri-O-methyl β-cyclodextrin (TM-βCD), 2,3,6-tri-O-trimethylsilyl β-cyclodextrin (TMS-βCD) or cucurbit[7]uril (CB7) and bulky 9,9-dioctylfluorene-2,7-diboronic acid bis(1,3-propanediol) ester (**DF**) (Figure 1). Their optical, electrochemical and morphological properties have been evaluated and compared to those of the non-rotaxane **1** counterpart. The comparison reveals that the rotaxane formation is sufficient to induce the desirable film forming ability combined with a high transparency as well as favourable optical and morphological properties. Fluorescence emission shows vibronic transitions and a mono-exponential kinetics independent of the concentration. HOMO/LUMO energy levels proved that the polyrotaxanes are electrochemically accessible in an electroluminescence configuration cell. Based on AFM analysis, the less flexible conformation of the *rod-like* polyrotaxane chains indicates their higher tendency to organize into fibers or linear ribbons in the solid state. These findings are relevant to the application of these supramolecular architectures in electronic devices, where it is essential to prevent luminescence quenching without hindering charge transport properties.

Keywords: fluorene-bithiophene copolymer, host-guest system, polyrotaxanes, macrocycles, permethylated βCD, persilylated βCD, fluorescence, wetting properties, surfaces, optical applications.

Introduction:

Conjugated polymers (CPs) have gained widespread interest as an alternative to conventional inorganic materials in many electronic applications. Undesirable intermolecular interactions, which affect the fluorescence efficiency limit considerably their application as semiconductor materials in optoelectronics.[1] The past decade has witnessed remarkable innovations and progress in polymer science, including the field of supramolecular science as a complementary field, which offers great opportunity to tune a large number of physico-chemical properties of CPs by polyrotaxane formation.[2,3] The polyrotaxane architectures preserve the semiconducting and optical properties of conjugated backbones and keep the conjugated chains at a minimum separation distance, imposed by the thickness of the macrocycle walls and diminish the aggregation tendency. Despite the reduction of aggregate formation, threading of conjugated backbones into macrocycles leads to an increasing environmental stability and resistance to quenching from impurities. This approach has been applied to the synthesis of PF-BT polyrotaxanes by incorporating chemically-modified CDs or CB7 as host molecules.

Materials and Methods:

The synthesis and characterization of the polyrotaxanes **1·RM-βCD**, **1·TM-βCD**, **1·TMS-βCD** and **1·CB7** as well as the non-rotaxane **1** counterpart used in this study is described elsewhere.[4-6]

Results and Discussions

In order to investigate the effect of macrocyclic encapsulation on the photophysical properties of PF-BT copolymers, **1·RM-βCD**, **1·TM-βCD**, **1·TMS-βCD** and **1·CB7** polyrotaxanes and the non-rotaxane **1** counterpart have been synthesized from a 1/1 molar ratio of **BT** encap-

sulated into RM-βCD, TM-βCD, TMS-βCD or CB7 cavities with **DF**.[4-6]

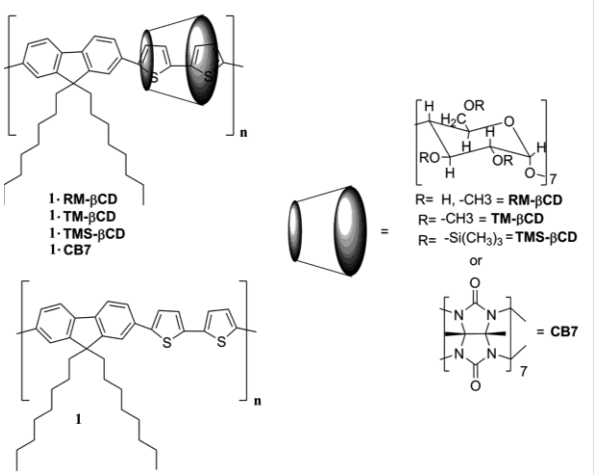

Figure 1: Chemical structures of **1·RM-βCD**, **1·TM-βCD**, **1·TMS-βCD** and **1·CB7** polyrotaxanes and the non-rotaxane **1** counterpart.

The synthesis of polyrotaxane structures leads to distinct improvements in the solubility, thermal stability, better film forming ability combined with a high transparency. The optical properties of the compounds were investigated by UV-Vis and fluorescence spectroscopy, Table 1.

Table 1. Optical properties

Samples	λ_{abs}^{max} (nm)	λ_{em}^{max} (nm)	Φ_{PL} [a]	τ_F (ps)[b]
1·RM-βCD[c]	446	493, 523[d]	0.35	630
1·TM-βCD[e]	452	511, 537[d]	0.49	620
1·TMS-βCD[e]	440	496, 530, 569[d]	0.47	640
1·CB7[f]	390	494, 521	0.45	665
1[e]	450	498, 527, 560	0.52	630

[a] Fluorescence quantum yield; [b] Lifetimes; [c] Measured in $CHCl_3$;[d] Shoulder in the emission; [e] Measured in THF; [f] Measured in a 9:1 (v/v) THF/DMSO mixture of solvents.

The emission shows different vibronic transitions for the samples and a mono-exponential kinetics independent of the solution concentration. The diagram of the HOMO/LUMO energy levels of compounds suggest good compatibility in an organic photovoltaic configuration cell using Al (cathode) and ITO (anode).[4-6] The less flexible conformation of the *rod-like* polyrotaxane chains, investigated by AFM, indicates their higher tendency to organize into fibers or linear ribbons in the solid state.

Conclusions:

These investigations provide that the PF-BT's photophysical properties could effectively be improved by rotaxane formation. The future strategy is to find additional improvements of these complex architectures for the generation of active layer in organic electronic devices.

Acknowledgements:
The research has been supported by the Romanian National Authority for Scientific Research, MEN - UEFISCDI, project number PN-II-ID-PCE-2011-3-0035.

References:

1. Noriega, R., Rivnay, J., Vandewal, K., Koch, F. P. V., Stingelin, N., Smith, P., Toney, M. F., Sallelo, A. (2013), A general relationship between disorder, aggregation and charge transport in conjugated polymers, *Nat. Mat.*, 12, 1038–1044.
2. Frampton, M. J., Anderson, H. L. (2007), Insulated molecular wires, *Angew. Chem. Int. Ed.*, 46, 1028-1064.
3. Harada, A., Hashidzume, A., Yamaguchi, H., Takashima, Y. (2009), Polymeric rotaxanes, *Chem. Rev.*, 109, 5974-6023.
4. Farcas, A., Ghosh, I., Grigoras, V. C., Stoica, I., Peptu, C., Nau, W. M. (2011), Effect of rotaxane formation on the photophysical, morphological, and adhesion properties of poly[2,7-(9,9-dioctylfluorene)-alt-(5,5'- bithiophene)] main chain polyrotaxanes, *Macromol. Chem. Phys.*, 212, 1022–1031.
5. Farcas, A., Tregnago, G., Resmerita, A.-M., Taleb Dehkordi, S., Cantin, S., Goubard, F., Aubert, P.-H., Cacialli, F. (2014), Effect of permodified β-cyclodextrin on the photophysical properties of poly[2,7-(9,9-dioctylfluorene)-*alt*-(5,5′-bithiophene)] main- chain polyrotaxanes, *J. Polym. Sci. A Polym. Chem.*, 52, 460-471.
6. Farcas, A., Aubert, P.-H., Mohanty, J., Lazar, A. I., Cantin, S., Nau, W. M. (2015), Molecular wire formation from poly[2,7-(9,9-dioctylfluorene)-*alt*-(5,5′- bithiophene /cucurbit[7]uril)] polyrotaxane copolymer, *Eur. Polym. J.*, 62, 124-129.

Development of nano-porous geopolymer for passive cooling systems

M. Alshaaer[1,*], J. Alkafawein[2], Y. Al-Fayez[2], T. Fahmy[1,3], M. Zamorano Toro[4], M. Martín Morales[5]

[1] Department of Physics, Prince Sattam Bin Abdul Aziz University, 11942 Alkharj, Saudi Arabia
[2] Department of Chemistry, King Faisal University, Al-Ahsa, Saudi Arabia
[3]Department of Physics, Faculty of Science, Mansoura University, Mansoura 35516, Egypt
[4] Departament of Civil Engineering, University of Granada, 18071 Granada, Spain
[5] Department of Building Construction, University of Granada, 18071 Granada, Spain

Abstract:
This work aims to investigate the use of alkali activated metakaolinite from natural kaolinitic soil as precursors for the production of Nano-porous geoplymer cement for passive cooling systems. Nano – porous geopolymer cement was synthesized using metakaolinite, and alkaline activators, namely sodium silicate (Na_2SiO_3) and sodium hydroxide. For metakaolinite preparation, Kaolinitic soil sample was collected from kaolin deposit (Saudi Arabia), which is located in Riyadh region. XRD analysis showed that kaolinite phase, was diminished due calcination and geopolymerization. The produced geopolymer cement exhibited a flexural strength of 12.3MPa, and compressive strength of 32MPa and 44.2MPa under immersed and dry conditions. The microstructure of the produced geopolyemer was characterized by formation of Nano-porous network as shown by the SEM images. The general evaluation of the produced geopolymer cement from kaolinitic soil indicates its potential for a number of applications including green construction materials, and passive cooling.

Keywords: Nano-porous, Geopolymers, Kaolinite, SEM, Construction, Minerals, Strength.

1 Introduction

Geopolymerisation, refers to stabilization of aluminosilicates such as kaolinite and transformation into geopolymers [1-5]. Geopolymers consist of an amorphous, structure resulting from the transformation of aluminosilicate monomers in an alkaline solution [4,5]. The geopolymerization reactions involving polycondensation of hypothetical monomers, i.e. orthosialate ions, has been proposed. As a result of these reactions, solid, hard, and stable materials similar to hydroxysodalite, feldspatiod or zeolite are formed [6]. These geopolymers are composed from SiO_4 and AlO_4 tetrahedra linked alternately by sharing all the oxygen atoms. When aluminum is four coordinated to oxygen atoms, a negative charge is created and therefore the presence of cations such as (Na^+, K^+, Li^+, Ca_2^+, Ba_2^+, NH_4^+, and H_3O^+) is essential to balance the negative charge of Al in the fourfold coordination [7].

Geopolymers cement has recently received wide attention in view of their advantages over other cementitious materials, like Portland cement. Some of the advantages are high strength, low environmental impact, chemical resistance and thermal stability [8,9]. Geopolymer cement results from the geopolymerization of aluminosilicate monomers in an alkaline solution; the products obtained are considered ceramic-like materials. Kaolin clay is an abundant natural resource and readily commercially available. The objective of this work is to determine if a low purity kaolin mineral from mineral deposits in Saudi Arabia can be successfully used to produce alkali-activated geopolymer cement. The investigation addressed the synthesis and evaluation of nano-porous geopolymer cement using kaolinite from Saudi Arabia, in terms of microstructure, mechanical, and physical properties. The significance of this research is to encourage the commercializing of the geopolymer cement by using low cost, and available in large amounts precursors such as low purity kaolin from local deposits [6-9]. The produced Nano-porous geopolymer cement could be a good candidate for passive cooling using evaporative cooling system.

2 Materials and methods

2.1 Materials

Nano-porous Geopolymer cement was synthesized using kaolinite from natural deposit, sodium silicate (Na_2SiO_3) and sodium hydroxide. Untreated kaolinite was collected from a deposit in Riyadh region (Saudi Arabia) with the assist of Saudi Ceramic Company. Preparation of the kaolinite samples involved crushing of oven dried clay (at 105 °C) with a grain size less than 60 µm. The powdered clay was heated at 750 ^oC for 4 h in a laboratory furnace to obtain its respective metakaolinite. The chemical composition of kaolinite was determined by X-ray Fluorescence (XRF) (Bruker System S4 Pioneer) and is given in Table 1. Na_2SiO_3 and NaOH solutions were used as alkaline activators for the dissolution of aluminosilicate phases. Sodium silicate solution (Merck, Germany) contained 27% SiO_2 and 8% Na_2O. The hydroxide solution with a concentration of 6.0 M was prepared using sodium hydroxide (NaOH) flakes of 98% purity (Merck) and distilled water.

Table 1, Chemical analysis of untreated kaolinite

Compound	Composition%
MnO	0.3
Cr_2O_3	0.4
CaO	1.1
K_2O	0.1
P_2O_5	0.9
Fe_2O_3	9.3
Al_2O_3	22.5
SiO_2	38.1
TiO_2	14.2

2.2 Production of geopolymer cement

The ratios used during the alkaline activation process were: SiO_2 (in sodium silicate solution)/Al_2O_3 (in metakaolinite) molar ratio of 1, and Na2O (in sodium silicate and NaOH solutions)/Al_2O_3 (in metakaolinite) molar ratio of 1. The H_2O/Na_2O molar ratio was 13. The aqueous solution of Na_2SiO_3, NaOH and H_2O was mechanically mixed for 1 min. Metakaolinite was mixed with the sodium hydroxide and sodium silicate solutions for 15 minutes. The final pulp was poured into three rectangular molds (160mm×15mm×30mm each) which were cured in a ventilated oven (Binder-ED115, Germany) at 40oC for one day. After curing, specimens were removed from the molds and cooled at room temperature. In addition, three discs (2cm×2cm×1cm) were prepared from each mixture, to carry out microstructural and mineralogical studies using XRD, TGA and SEM.

2.3 Mineralogical analyses

X-ray diffraction (XRD) analyses were carried out on powdered samples to identify major crystalline and potentially newly formed phases using a Shimadzu diffractometer-6000 (Japan) with a Co tube and a scanning range from 5^o to 80^o 2θ at a scan rate of 2°/min. Qualitative analysis was carried out using the crystalline phases were identified by detecting and analyzing the positions of the peaks using the software package supplied with the instrument. The morphology of the specimens was studied using an Inspect F50 scanning electron microscope (Netherlands). The samples were pre-coated with platinum under an argon atmosphere. Energy-dispersive X-ray spectroscopy (EDX) was used for elemental analysis and chemical characterization of samples.

2.4 Mechanical and physical characterizations of geopolymer cement

The fabricated specimens were tested for the water absorption, the density, the flexural strength and the compression strength. Water absorption of the immersed specimens (Group-2) was calculated for each series according to the following equation.

$$W\ \% = ((W_w - W_d)/W_d) \times 100\ \%$$

Where, W % is the absorption of water expressed as percentage; W_w and W_d are the weights of the immersed specimen and of specimens after drying, respectively. For density measurements, the eight specimens after the curing were weighed using an electronic balance and their dimensions were measured using a digital micrometer. The specimens were tested in three-point bending and in compression. Testing was performed at room temperature with a universal testing machine. The bending specimen's dimensions were: height=15 mm, width=30 mm and length 160 mm, the distance between the supports was 120 mm and the speed of the machine head during testing was 0.1 mm/minute. Compression tests were performed on the failed bending specimens, placed on their side with a

loading area=40×15 mm^2 and height=30 mm. The speed of the machine head during testing was 2 mm/minute.

3 Results and discussion

3.1 Microstructural characteristics and phase composition

The XRD patterns of kaolinitic soil and produced geopolymer cement are reported in Fig.1. The results show that most the identified peaks are corresponding to kaolin, Fig1-B. As a result of calcination and metakaolinite-alkali geopolymerization a high background seen in XRD patterns, Fig. 1-A, between 20^o to 40^o indicates the presence of amorphous phases [6]. The amorphous phase detected could be albite since the K^+ content in the reactants (kaolinite and Na-silicate solution) is very low compared to Na^+. The diminishing of XRD peaks corresponding to kaolinite and the formation of amorphous phase (gel) indicate to the high percentage of the geopolymerization of kaolinitic soil. The geopolymer gel is considered as the binder material of the end products as shown by the SEM analysis, Fig.2. The formation of high amount of binder material is an indication of the high mechanical performance and stability of the produced geopolymer cement [3].

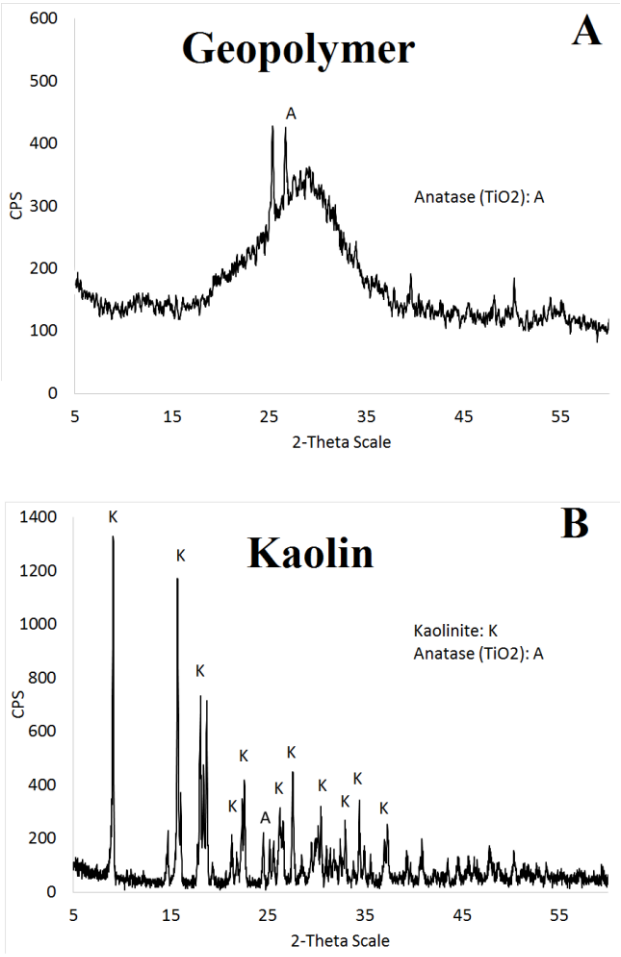

Figure 1: Qualitative XRD patterns of powdered kaolinitic soil, and powdered geopolymer cement

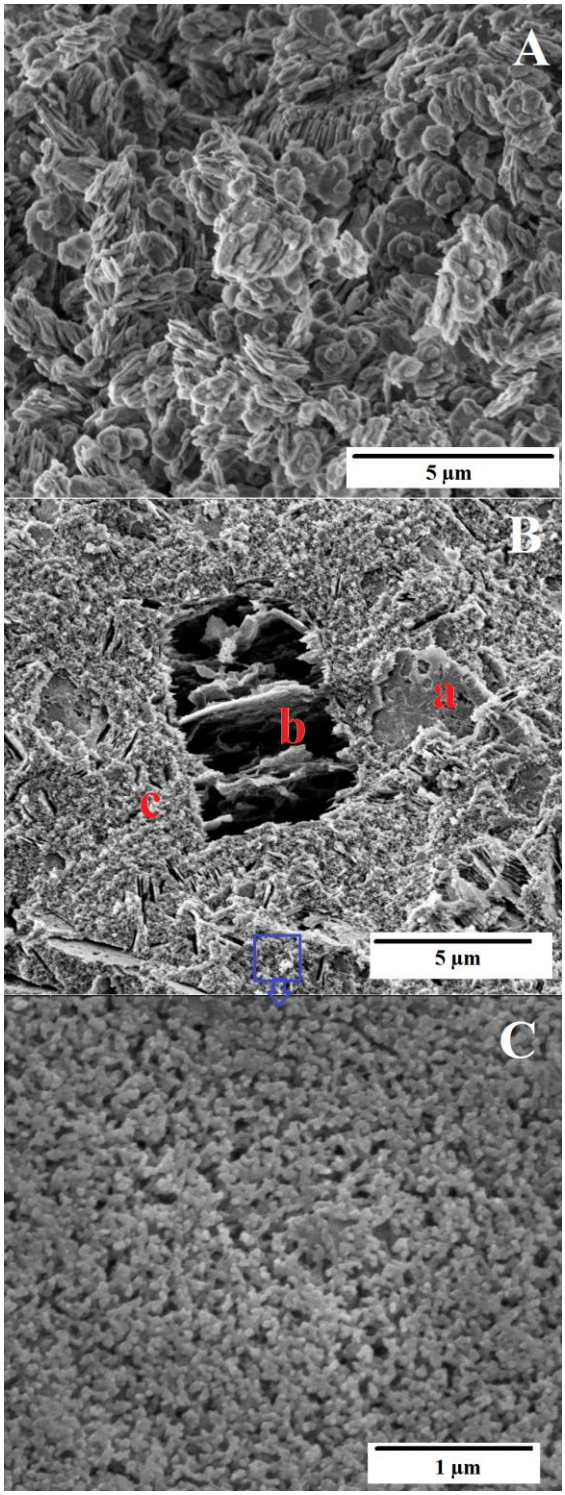

Figure 2: SEM image of geopolymer cement; A: Kaolin, B: fully transformed metakaolin, C: Nano-porous sodium aluminum silicate phase (geopolymer gel).

The layers of metakaolin are repoted by the SEM as shown in Fig. 2-A. SEM analysis indicates that the microstructure of metakaolinite-based geopolymers, is characterized by the coexistence of geopolymer gel and partially unreacted metakaolinite layers (Fig. 2-B). This SEM image reveals also that due to geopolymeric reactions the gaps between partially reacted metakaolinite layers have been filled with formed geopolymeric gel (sodium aluminosilicate matrix).

The metakaolinite, which is considered as precursor in this study, was attacked by the alkaline solution during geoplymerisation as shown in Fig. 3 and was partially consumed. The residual metakaolin was amorphous, as seen in Fig. 2-B. Due to the alkaline attack, macro holes filled with new formed Na-aluminosilicates are widely scattered between the residual metakaolin layers. The geopolymer gel, binder material, composed from Nano-porous network, Fig. 2-C. The size of the pores less than 100 nm as reported in this figure.

3.2 Physical and Mechanical properties of geopolymers

Experimental results show that flexural strength of the produced geopolymers is around 12.3MPa. It is reported also that compressive strength of the produced geopolymer is 32MPa and 44.2MPa under immersed and dry conditions respectively. The bulk density, 1.45g/m^3, and water absorption 15% (w/w). These results are comparable with geopolymer produced from pure kaolin [3,6,9].

4 Conclusions

Nano-porous Geopolymers have been successfully produced by alkali-activation of natural and untreated kaolinitic soil from mineral deposits in Saudi Arabia. The products composed mainly from geopolymer gel and broken kaolinite layers. The geopolymer gel consists a Nano-porous network with pore sizes less than 100nm. Due to its optimum pore sizes and the regular pore network, this cement could be a good candidate for evaporative cooling systems.

Acknowledgments:

The financial support of the project "Development of functional geopolymer – based construction materials for passive cooling of buildings" funded under the contract number (AT-34- 211) by the King Abdulaziz City for Science and Technology KACST within the Research Grants Program is gratefully acknowledged.

References:

1. Davidovits, J., Geopolymer chemistry and sustainable development. The Poly(sialate) terminology: a very useful and simple model for the promotion and understanding of green-chemistry. In: Davidovits J., ed. Proc. of the World Congress Geopolymer, Saint Quentin, France, 28 June – 1 July 2005: p. 9-15.
2. Alshaaer, M., Two-phase geopolymerization of kaolinite-based geopolymers, Applied Clay Science, 86, 2013, 162–168
3. Khale, D., Chaudhary, R., Mechanism of geopolymerization and factors influencing its development: a review, J. Mater. Sci. 42, 2007, 729–746.
4. Bignozzi, M.C., Manzi, S., Lancellotti, I., Kamseu, E., Barbieri, L., Leonelli, C., Mix design and characterization of alkali activated materials based on metakaolin and ladle slag. Appl. Clay Sci. 73,2013, 78–85.
5. Yousefi, E.,Majidi, B., Effects of free quartz onmechanical behaviour of kaolinite based geopolymers, Materials Technology: Advanced Performance Materials, 26, 4, 2,2011, 96-99.
6. Alshaaer, M., Cuypers, H.,Wastiels, J., Stabilisation of kaolinitic soil for construction purposes by using mineral polymerisation technique. Proceedings of the 6th International Conference Technology for Developing Countries, ed. Musa Resheidat,(3), Jordan, 2002, 1085–1092.
7. Alshaaer, M., El-Eswed, B., Yousef, R.I., Khalili, F., Rahier, H., Development of functional geopolymers for water purification, and construction purposes. Journal of Saudi Chemical Society, DOI:10.1016/j.jscs.2012.09.012, 2012.
8. Oswaldo Burciaga-Diaz, Jose Ivan Escalante-Garcia, Alexander Gorokhovsky, Geopolymers based on a coarse low-purity kaolin mineral: Mechanical strength as a function of the chemical composition and temperature, Cement & Concrete Composites, 34, 2012, 18–24.
9. Rowles M, O'Connor B., Chemical optimization of the compressive strength of aluminosilicate geopolymers synthesized by sodium silicate activation of metakaolinite, J Mater Chem, 13, 2003, 1161–1165.

Nanofluids with enhanced thermal properties: an experimental and theoretical analysis

Javier Navas,[1] Antonio Sánchez-Coronilla,[2] Elisa I. Martín,[3] Roberto Gómez-Villarejo,[1] Miriam Teruel,[1] Juan Jesús Gallardo,[1] Teresa Aguilar,[1] Rodrigo Alcántara,[1] Concha Fernández-Lorenzo,[1] Joaquín Martín-Calleja[1]

[1]Cádiz University, Department of Physical Chemistry, Cádiz, Spain
[2]Seville University, Department of Physical Chemistry, Seville, Spain.
[3]Seville University, Department of Chemical Engineering, Seville, Spain.

Keywords: nanofluids, Concentrating Solar Power, Dynamic Molecular, heat transfer fluid, specific heat, thermal conductivity, nanoparticles.

Concentrating Solar Power (CSP) is one of the most interesting option as renewable energy today. One option in order to improve the efficiency of these plants is to enhance the properties of the heat thermal fluid (HTF) used. Thus, one of the research lines of greater interest is the use of nanofluids to enhance the thermal properties of HTFs, because of the incorporation of solids into these fluids improves several thermal properties such as thermal conductivity or the heat transfer coefficient.[1,2] In this work, we report nanofluids based on metallic nanoparticles, and we analysed the effect of the presence of the nanoparticles in different properties such as density, viscosity, and thermal properties, that is isobaric specific heat, thermal conductivity, and thermal diffusivity. So, in function of the nanoparticle nature, the enhancement of the HTF properties were different. Also, in order to understand the behaviour of the nanofluidics systems, dynamic molecular analysis were performed. The structural and dynamic properties of the nanofluids were analysed. From, radial distribution function (RDF) and the spatial distribution function (SDF) analysis, the structural properties of the systems were studied. In turn, the thermal properties were estimated from theoretical calculations, and the same trend obtained from the experimental results were observed, which validates the methodology proposed.

The nanofluids studied in this work were prepared by means of the two-step method.[3] This method consist of the dispersion of nanoparticles into the base fluid. The nanoparticles are synthesized (first step) and then dispersed into the base fluid (second step). In this study, a eutectic mixture of biphenyl ($C_{12}H_{10}$, 26.5%) and diphenyl oxide ($C_{12}H_{10}O$, 73.5%) was used as the base fluid. Also, commercial Cu and Ni nanoparticles were added. Cu nanoparticles (purity ≥ 99.5%, density 8940 kg m^{-3} at 298 K, Sigma-Aldrich©), showed a particle size of 40.60 nm. Ni nanoparticles (purity ≥ 99%, density 8900 kg m^{-3} at 298 K, Sigma-Aldrich©), showed a particle size of < 100 nm.

The performance of the nanofluid prepared was analysed according to Dittus-Boelter equation,[4,5] which was used as a *Figure of Merit*. The Dittus-Boelter equation gives the ratio between the heat transfer coefficient, h, of the nanofluid and the base fluid, which depends on the density, ρ, viscosity, μ, isobaric specific heat, C_p, and thermal conductivity, k, according to

$$FoM = \frac{h_{nf}}{h_{bf}} = \left(\frac{\rho_{nf}}{\rho_{bf}}\right)^{0.8}\left(\frac{k_{nf}}{k_{bf}}\right)^{0.6}\left(\frac{C_{p(nf)}}{C_{p(bf)}}\right)^{0.4}\left(\frac{\mu_{nf}}{\mu_{bf}}\right)^{-0.4}$$

where subscripts nf and bf are related to nanofluid and base fluid, respectively. When $h_{nf}/h_{bf} > 1$, an improvement in the performance of the nanofluid with respect to the base fluid is obtained. From the values measured for density, viscosity, isobaric specific heat and thermal conductivity, this *FoM* was estimated. The values obtained are shown in Figure 1. It shows how the efficiency of the nanofluid system can be improved by up to 11% by adding Cu nanoparticles to the base fluid. In turn, the addition of Ni nanoparticles does not improve the performance of the base fluid. So different behaviour is found depending on the nature of the nanoparticles used.

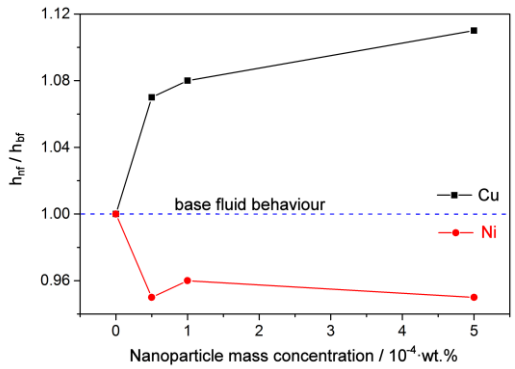

Figure 1. Values of the ratio of the heat transfer coefficients for the nanofluids prepared.

For understanding the different behaviour of the two nanofluids systems depending on the nature of the nanoparticles, molecular dynamics calculations were performed. From RDF and SDF analysis, there is difference in the interaction between metal and O. For Cu nanofluids, there is three O atoms around the metal, but for Ni nanofluids there is only one O atom around the metal. This results is found too from SDF analysis, as is shown in Figure 2. In this Figure, red surface is assigned to O atoms, blue surface is related to C atoms bonded to O atoms, and sky-blue surface is assigned to C in the benzene rings. So, three biphenyl oxide molecules round the Cu, but only one biphenyl oxide rounds the Ni. The reason of this situation is the π-interaction. Cu-benzene interaction is weak probably due to a stable d^{10} configuration for Cu. Ni-benzene interaction is higher, because Ni atoms transfer charge to benzene rings, that is π-interaction is produced. So the different reordering of the base fluid around the metal must be responsible for the different thermal properties found in the two nanofluids. The preference for an M-O interaction for Cu seems to be favoured and leads to an increase of C_p and thermal conductivity.

Thus, this study provides us with a better understanding of how the HTF molecules are rearranged around the metal, leading to an enhancement of the thermal properties.

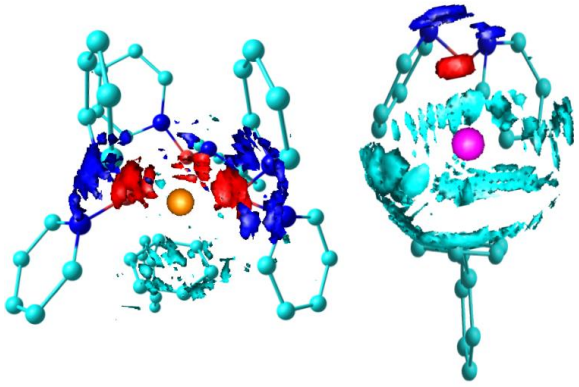

Figure 2. The metal-fluid interactions lead to a different behaviour of the thermal properties of nanofluids based on metallic nanoparticles (Cu on the right and Ni on the left) and the eutectic mixture of diphenyl oxide and byphenil as base fluid.

References:

[1] Yoo, D. H., Hong, K. S., Yang, H. S. (2007) Study of thermal conductivity of nanofluids for the application of heat transfer fluids, *Thermochim. Acta*, 455, 66-69.

[2] Lee, S., Choi, S. U. S., Li, S., Eastman, J. A. (1999) Measuring thermal conductivity of fluids containing oxide nanoparticles, *J. Heat Trans-T. Asme*, 121, 280-289.

[3] Li, Y. J., Zhou, J. E., Tung, S., Schneider, E., Xi, S. Q. (2009) A review on development of nanofluid preparation and characterization, *Powder Technol.*, 196, 89-101.

[4] Dittus, F.W., Boelter, L.M.K. (1930) Pioneers in heat transfer - heat transfer in automobile radiators of the tubular type, *University California Publications Eng.*, 2, 443-461.

[5] Singh, D., Timofeeva, E. V., Moravek, M. Cingarapu, S. R.,. Yu, W. H., Fischer, T., Mathur, S. (2014) Use of the metallic nanoparticles to improve the thermophysical properties of the organic heat transfer fluids used in concentrated solar power, *Sol. Energy*, 105, 468-478.

Optimized reliable Metal-IN InGaN solar cell

Abdoulwahab Adaine[1,2], Sidi Ould Saad Hamady[1,2], Nicolas Fressengeas[1,2]
[1]Université de Lorraine, Laboratoire Matériaux Optiques, Photonique et Systèmes, Metz, F-57070, France
[2]Laboratoire Matériaux Optiques, Photonique et Systèmes, CentraleSupélec, Université Paris-Saclay, Metz, F-57070, France

The Indium Gallium Nitride (InGaN) ternary alloy is a good material for high–efficiency–high–reliability solar cells, notably through its good tolerance to radiations, its high light absorption and its Indium–composition–tuned bandgap [1]. Unfortunately, owing to the lack of *ad hoc* acceptors and to residual n-doping [2], InGaN p-doping is still a challenge.

We propose a new Metal-IN (MIN) InGaN solar cell structure, Shown on figure 1, where the InGaN p-doped layer is removed and replaced by a Schottky contact, addressing the above mentioned drawback. A set of realistic physical models based on actual measurements is used to simulate and optimize its behavior and performance using mathematically rigorous multi-veried optimization methods.

The material dependent parameters used in this study have been determined for GaN and InN binaries, either from experimental work or ab initio calculations. The values for InGaN were linearly interpolated in between the GaN and InN binaries, except for the bandgap E_g and the electronic affinity χ where the modified Vegard Law was used, with a bowing factor $b = 1.43eV$ for the bandgap and $b = 0.8eV$ for the affinity, respectively [3].

The transport equations for electrons and holes are derived from a drift-diffusion model. We included in the model the bandgap narrowing effect [4], as well as the Shockley–Read–Hall (SRH) [5] and the direct and Auger recombination models using Fermi statistics [6]. The holes and electrons lifetime was taken equal to 1ns [7] in InGaN.

Light absorption and refraction index in InGaN are modeled for the whole solar spectrum and for all x Indium compositions.

The device was then simulated in the framework of the above mentioned drift-diffusion model using the Atlas® device simulation tool from Silvaco®. The mathematically rigorous L-BFGS-B quasi-Newton optimization method [8] was used to find the optimum efficiency with respect to a given set of parameters; work done through a Python package that we developed in the SAGE interface to the SciPy [9] optimizers, using the Atlas® simulator as the backend engine.

The MIN solar cell was optimized with respect to its most important parameters: L_i and L_n , the thicknesses of the I and N layers respectively, N_i and N_d , the doping levels of the I and N layers respectively, the Indium composition x and the metal workfunction W_f . The optimal values for all these parameters have been sought within a physically and technologically meaningful interval.

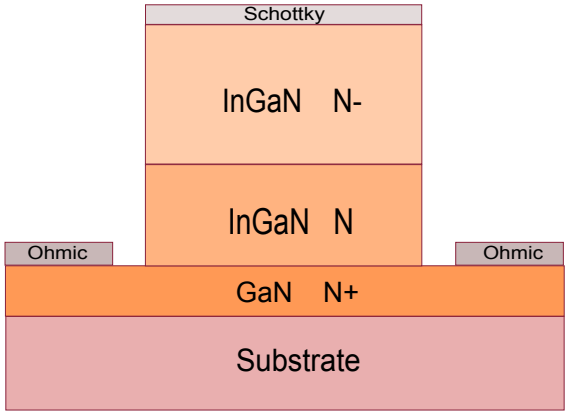

Figure 1: Schematic views of the Schottky and MIN solar cells structures.

The resulting optimum efficiency is reported in table 1, along with the associated photovoltaic parameters as well as the corresponding parameters and their tolerance range. The results corresponding to the previously reported Schottky structure [10, 11] are provided for comparison purposes.

Figure 2 shows the current-voltage characteristics of the optimal MIN solar cell, the Schottky one still being shown for comparison purposes. We observe that the MIN structure has a lower V_{OC} compared to the Schottky structure, but a higher J_{SC}, associated to a higher overall efficiency. This behavior stems from the change in the bandgap induced by the Indium composition variation.

The maximum MIN cell efficiency is found to be 19.8%, It is associated to wide tolerance ranges, addressing two of the major drawbacks of InGaN technology for solar cells. Indeed, on the one hand, the Schottky contact has removed the need for p-doping, yielding a MIN solar cell with an efficiency comparable to that of the highest efficiencies reported for the thin films structures. On the other hand, the MIN structure wide tolerances could facilitate the design of low resistance ohmic contacts and growth defects management, leading to the next generation of high efficiency reliable solar cells.

	$L_i(\mu m)$	$L_n(\mu m)$	$N_i(cm^{-3})$	$N_d(cm^{-3})$	$W_f(eV)$	x	$\eta(\%)$ $V_{OC}(V)$ $J_{SC}(mA/cm^2)$ $FF(\%)$
Range	$[0.10-1.00]$	$[0.10-1.00]$	$[1.0\times10^{14}-1.0\times10^{17}]$	$[1.0\times10^{16}-1.0\times10^{19}]$	$[5.50-6.30]$	$[0.00-1.00]$	
MIN	**0.61** $[0.10-1.00]$	**0.83** $[0.10-1.00]$	6.1×10^{16} $[1.0\times10^{14}-1.0\times10^{17}]$	3.6×10^{17} $[1.8\times10^{16}-1.0\times10^{19}]$	**6.30** $[6.11-6.30]$	**0.60** $[0.48-0.72]$	**19.8** **0.835** **30.29** **78.39**
Schottky		**0.86** $[0.53-1.00]$		6.5×10^{16} $[1.0\times10^{16}-3.0\times10^{17}]$	**6.30** $[6.15-6.30]$	**0.56** $[0.50-0.72]$	**18.2** **0.863** **26.80** **78.82**

Table 1: Optimum efficiency η obtained for the *MIN* solar cell and associated open-circuit voltage V_{OC}, short-circuit current J_{SC} and Fill Factor FF, along with the corresponding physical and material parameters, all compared to the previously published *Schottky* structure used as a reference. These results are obtained from several optimizations with random starting points ensuring the absoluteness of the optimum efficiency η. x is the indium composition. L_i and L_n are the thicknesses of the I and N layers respectively and where applicable. N_i and N_d are the dopings of the I and N layers respectively where applicable. For each parameter, a range and a tolerance range are given. The range is on the second line of the table. It is the range within which the optimum value of a given parameter is sought. The tolerance range is given just below each parameter optimal value. It corresponds to the set of values of that parameter for which the efficiency η remains above 90% of its maximum, the other parameters being kept at their optimum values.

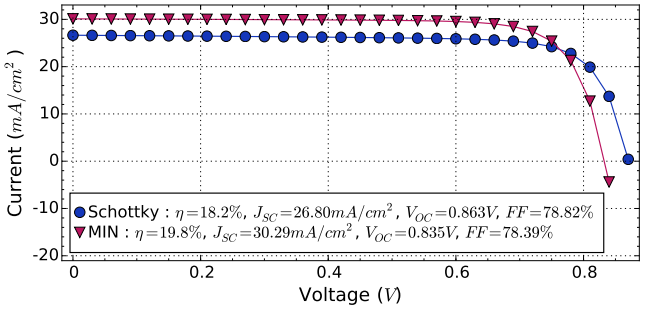

Figure 2: Current-voltage characteristics for the *InGaN* Schottky and MIN solar cells.

References

[1] A. Bhuiyan, K. Sugita, A. Hashimoto, A. Yamamoto, InGaN solar cells: present state of the art and important challenges, Photovoltaics, IEEE Journal of 2 (3) (2012) 276–293.

[2] B. Pantha, H. Wang, N. Khan, J. Lin, H. Jiang, Origin of background electron concentration in In x Ga 1-x N alloys, Physical Review B 84 (7) (2011) 075327.

[3] G. Franssen, T. Suski, A. Kamińska, J. Pereiro Viterbo, E. Muñoz Merino, E. Lliopoulus, A. Georgakilas, S. Che, Y. Ishitani, A. Yoshikawa, et al., Bowing of the band gap pressure coefficients in InGaN alloys, Journal of Applied Physics 103 (3) (2008) 033514–1.

[4] H. Schenk, S. Borenstain, A. Berezin, A. Schön, E. Cheifetz, S. Khatsevich, D. Rich, Band gap narrowing and radiative efficiency of silicon doped gan, Journal of Applied Physics 103 (10) (2008) 103502.

[5] H.-Y. Ryu, H.-S. Kim, J.-I. Shim, Rate equation analysis of efficiency droop in InGaN light-emitting diodes, Applied Physics Letters 95 (8) (2009) 081114.

[6] F. Bertazzi, M. Goano, E. Bellotti, A numerical study of auger recombination in bulk InGaN, Applied Physics Letters 97 (23) (2010) 231118.

[7] K. Kumakura, T. Makimoto, N. Kobayashi, T. Hashizume, T. Fukui, H. Hasegawa, Minority carrier diffusion length in GaN: Dislocation density and doping concentration dependence, Applied Physics Letters 86 (5) (2005) 052105.

[8] J. Nocedal, S. J. Wright, Large-scale unconstrained optimization, Numerical Optimization (2006) 164–192.

[9] S. van der Walt, S. Colbert, G. Varoquaux, The NumPy array: A structure for efficient numerical computation, Computing in Science Engineering 13 (2) (2011) 22–30.

[10] S. Ould Saad Hamady, A. Adaine, N. Fressengeas, Numerical simulation of InGaN Schottky solar cell, Materials Science in Semiconductor Processing 41 (2) (2016) 219–225.

[11] A. Adaine, S. O. Saad Hamady, N. Fressengeas, Simulation study of a new InGaN p-layer free schottky based solar cell, Superlattices and Microstructures In Press (2016) . doi:10.1016/j.spmi.2016.05.020.

Low Cost and Free TCO Porous Coal as a Counter Electrode (CE) for Dye Sensitized Solar Cell (DSSC)

M.Y. Feteha, Shaker Ebrahim and Laila Saad

Department of Materials Science, Institute of Graduate Studies and Research, Alexandria University, P.O Box 832, Alexandria, Egypt.

Abstract:

In this work, commercial porous coal and its nanocomposites with platinum nanoparticles are investigated as a CE for DSSCs. Two types of CEs were fabricated using carbon material namely, commercial porous coal and commercial porous coal with electrodepositing of platinum nano-particles (NPs) layer. The photovoltaic cell parameters, i.e., open circuit voltage (Voc), short circuit current density (Jsc), fill factor (FF) and energy conversion efficiency (η) were evaluated under illumination (AM1.5) and were found to be 0.42 V, 4.9 mA/cm2, 0.26 and 0.53% respectively for new DSSC structure of glass/ITO/TiO2(NPs)-N3dye/electrolyte/commercial porous coal/Pt nanocompsites. The prepared materials and the cells were characterized using scanning electron microscope (SEM), cyclic voltammetry (CV), current density– voltage (J-V) and impedance measurements.

Introduction:

DSSC is used for the conversion of visible light into electricity based on the sensitization of a semiconductor with a wide band-gap by a dye as a sensitizer and Tri-iodide ions I3- created by the reduction of dye cations with I− ions are re-reduced to I- ions at the CE interface [1]. The increased cost of platinum has recommended the replacement of platinum as a CE for DSSC with other cheaper materials for decreasing the production cost of DSSCs [2]. The catalytic activity of inexpensive conducting polymers in DSSCs -such as Polypyrrole or Polyaniline and it's nanocomposites- have been investigated to find a replacement for the expensive platinum-based CE [2-3]. On the other hand, carbon nanotubes (CNTs) are a novel carbon allotrope that offers structural and electronic properties that are unique from other carbon allotropes, such as graphite, fullerene and diamond [4] but still relatively expensive. Carbonaceous materials are quite attractive to be applied as a CE for DSSCs due to their high electronic conductivity, high corrosion resistance towards I2, high reactivity for triiodide reduction and low cost production [5]. Prashant Poudel et al in 2014 reviewed the development in carbon based CEs which have the advantages of high surface area and high electrocatalytic ability due to the porous morphology. Various carbon nanostructures including graphene, carbon nanotubes, carbon nanofibers, carbon nanoparticles, conductive carbon, carbon dye and composite carbon nanostructures were investigated and their surface defects effect on DSSC performance was studied [6]. Yimhyun Jo et al in 2012 prepared highly interconnected ordered mesoporous carbon–carbon nanotubes nanocomposites which create a Pt-free DSSC with a remarkable long-term durability [7]. On the other hand, an ordered multimodal porous carbon (OMPC) as a CE was used in DSSCs and the cell efficiency was 8.67% [8].

In other work, a combination of porous coals with a different structures and dimensions were investigated for constructing a metal-free DSSC with a good stability and an efficiency of 7.5 % [9]. Also, a pure carbon CE was used for DSSC by an industrial flexible graphite sheet as substrate and activated carbon as a catalytic material. The CE shows a very low series resistance (Rs) and low charge-transfer resistance (Rct). The fabricated DSSC has a conversion efficiency of 5% [10]. In addition, a nano-scale carbon/TiO2 composite CE was used in DSSC and the efficiency was 5.5% compared to Pt-based CE DSSC with an efficiency of 6.4 % [11]. Many works [12-13] investigated the using of porous Pt films on a conductive glass substrate with different techniques (polyol reduction, electro-deposition and thermal decomposition) as a CE in a DSSC and the lowest gained efficiency (less than 3%) was attained using polyol technique.

In this work, two types of CEs were fabricated using a carbon material namely commercial porous coal and commercial porous coal with an electrodepositing of platinum nano particles (NPs) film. The new DSSC structu-tu-

re(glass/ITO/TiO2(NPs)N3dye/electrolyte/(porous coal) or (porous coal/Pt(NPs)) with TCO-free CE was characterized and the effect of different CEs on the cell performance was investigated.

Materials and Methods:

2.1 Commercial Porous Coal Preparation

The commercial coal substrates were first polished with two different sizes of sandpaper. Secondly, they were washed in an ultrasonic bath with distilled water at room temperature for 30 minutes followed by a drying stage at 80 ºC.

2.2 Electrochemical Preparation of Platinum Nanoparticles Film

Thin layer of platinum nanoparticles was electrodeposited on commercial porous carbon substrate in order to be used as counter electrode. Three-electrode system was used for Pt deposition and Pt plate counter and Ag/AgCl (SCE) reference electrodes are connected with potentiostat (750 G, Gamry instruments) using 0.01 M of K_2PtC_{l6} in 0.5 M of H_2SO_4 solution and applying of -0.3 V for 900 sec. As a consequence, two types of CEs (commercial porous coal and commercial porous coal with an electrodepositing of platinum nano-particles (NPs) film) were fabricated to be used in the assembled DSSC. On the other hand, the photo-electrode was prepared using the method mentioned in ref.[3].

2.3 DSSC Assembly

The assembly of DSSC was performed by sandwiching the sensitized N3 Ruthenium dye -TiO_2 NPs film photoelectrode with one of the two CEs using paper clips without an additional pressure. The potassium iodide (0.5M) and iodine (0.05M) as an electrolyte solution in ethanol was injected between the two electrodes. Photographs of the N3-TiO_2 NPs photoelectrode and the commercial coal CE are shown in Figure (1) and the fabricated DSSC structure is shown in Figure (2).

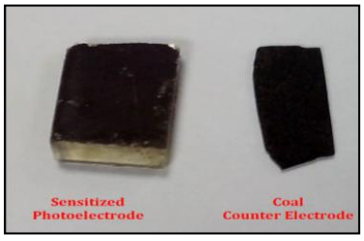

Fig. 1: Photograph of sensitized photoelectrode and coal CE.

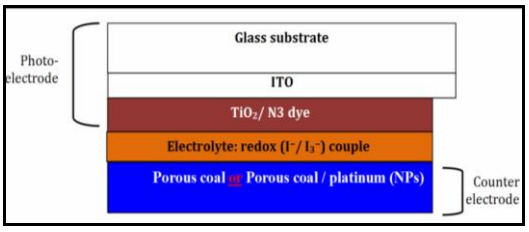

Fig. 2: DSSCs structures based on porous coal/ Pt counter electrode.

Results and Discussions

3.1 Morphology of Commercial Porous Coal Nanocomposites

SEM micrographs of commercial porous coal and commercial porous coal /platinum NP film CEs were performed for studying the morphologies of the carbon counter electrodes and the distribution of platinum NPs within it. Figure (3-a) shows that the coal electrode has a micro-porous surface which ensures a high surface area for the electrode. In addition, it can be observed from figures (3-b) and (3-c) that the platinum NPs are uniformly deposited in the inner side of the pores with a nano-scale and this will enhance the surface area as well as the roughness factor.

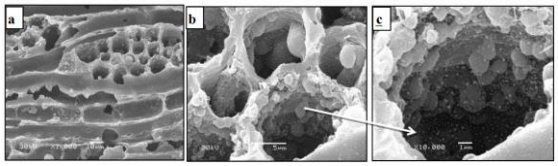

Fig. 3 SEM micrographs of (a) Commercial porous coal CE, (b) Commercial porous coal/platnium nanocomposite CE and (c) Magnification of porous coal /platnium nanocomposite CE.

3.2 Catalytic Activities of Commercial Porous Coal Counter electrode

The catalytic activity of the prepared electrodes toward the reduction of I3−/I− was investigated by cyclic voltammetry (CV) technique. The oxidation reduction peaks for porous coal and porous coal/ platinum NPs counter electrodes cannot well identified as shown in figures (4-a) and (4-b). This result suggests that the electrode may have low tendency toward the reduction of I3−/I− or may need more surface modification. On the other hand, it has been observed that after deposition of platinum NPs the area under curve was enlarged which indicates that the catalytic activity of the CE electrode was enhanced.

3.3 DSSCs Performance Characterization:

The performance of the prepared DSSCs was investigated using both electrochemical impedance spectroscopy and current density-voltage (J-V) characteristics. Moreover, the effect of changing the CE structure with the same photo-electrode and electrolyte on the cell performance was carried out. The using of commercial porous coal as a CE creates a novel DSSC structure with free TCO substrate.

3.3.1 Impedance Measurements: The Nequist impedance spectra (Figure(5)) of the DSSCs based on commercial porous coal counter electrode were performed before and after the deposition of platinum NPs on the surface of the porous coal counter electrode. Impedance measurements were carried out at a zero bias, ac amplitude of 10 mV and the electrolyte containing 0.5 M KI and 0.05 M I2 in ethanol. Table (1) shows the series resistance (R_s) and charge transfer resistance (R_{ct}) values of the cells at both dark and illumination (AM 1.5) conditions. The values of the R_s and R_{ct} are decreased with the presence of platinum NPs layer due to the high conductivity of Pt. The value of R_{ct} significantly deceases with approximately of 85 % for DSSC with porous coal/Pt counter electrode under illumination due to the low value of interfacial charge transfer resistance at the electrolyte/counter electrode interface [14]. This effect may be due to the high surface area of the deposited platinum NPs, as well as their superior catalytic property.

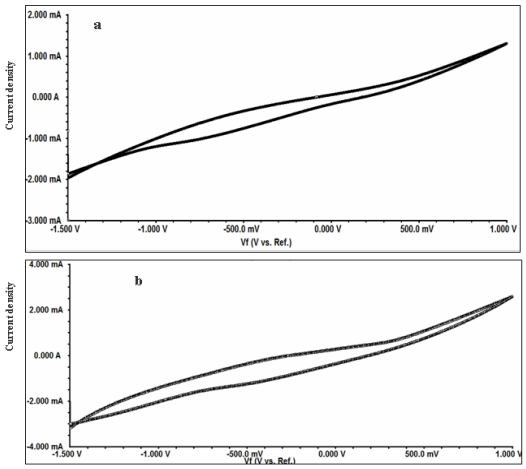

Fig. 4 CV curves of (a) Commercial porous coal and (b) Commercial porous coal/platinum nanocomposite counter electrodes.

The Warburg diffusion process [15] in the electrolyte at the low-frequency region can obviously observed in figure (5-a) under illumination and this supports that after deposition of platinum NPs the diffusion of the electrolyte in the CE has been enhanced as well as the reduction of I3−/I−. As a consequence, R_{ct} value remarkably decreased as shown in Table (1). As a conclusion, the enhanced photocatalytic activity of the porous coal/platinum composite is attributed to (1) the load of the Pt nanoparticles which increases the surface area of the electrode in addition to its high catalytic activity and (2) the carbon (commercial coal)-which identified as a rapid electron transfer unit- is facilitating the separation of photoelectron and hole pairs.

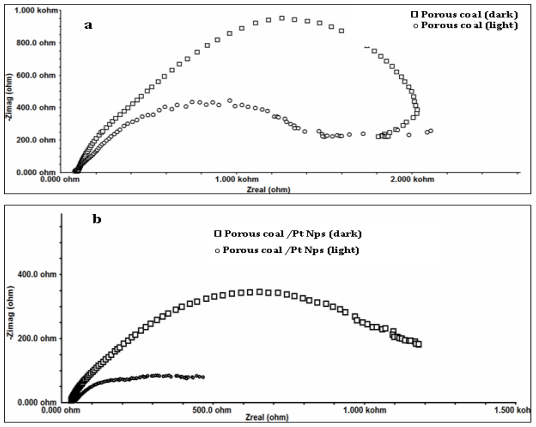

Fig. 5 Nyquist plots of DSSCs based on (a) Commercial porous coal and (b) Commercial porous coal /platinum nanocompsites.

Table 1 R_s and R_{ct} values for DSSCs with different counter electrode compositions at both dark and illumination (AM 1.5) conditions.

Counter electrode	Under Darkness		Under Illumination	
	R_S (Ω)	R_{ct} (Ω)	R_S (Ω)	R_{ct} (Ω)
Porous coal	80.7	2024	72.3	1390
Porous coal/platinum	43.3	1190	30.5	212

3.3.2 J-V characteristics: The photovoltaic performance of DSSCs was measured under dark and illumination (100 mW cm^{-2}) conditions using a computerized Keithley system source meter. Figure (6) shows the current density-voltage of DSSCs based on commercial porous coal CE. The photovoltaic parameters such as open circuit voltage (V_{oc}), short circuit current density (J_{sc}), fill factor (FF) and conversion efficiency (η) are summarized in Table (2). The conversion efficiency of the cell which based on commercial porous coal CE is 0.34 % with a low value of FF (0.26%). This low value of

FF may be due to the high R_s value of the cell as shown in Table (1). After the electrodeposition of the platinum NPs layer, the cell efficiency is enhanced by 56 % due to a reduction in R_s and R_{ct} values as mentioned in Table (1). Also, this effect is due to the good conductivity and the high surface area of the commercial porous coal/Pt NPs nanocomposite as shown in SEM micrograph of figure (3-b).

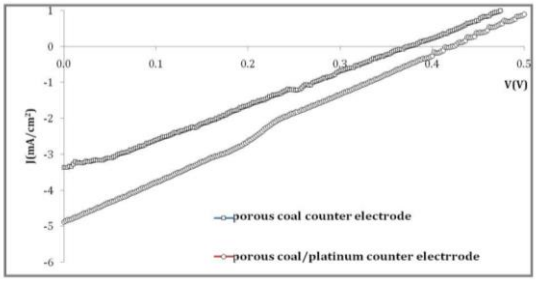

Fig. 6 J-V characteristic curves of DSSCs based on commercial porous coal CE.

Table 2. Photovoltaic parameters of DSSCs based on commercial porous coal CE**.**

Photovoltaic parameters / Counter electrode	Voc (V)	Jsc (mA/cm^2)	FF	η (%)
Commercial Porous coal	0.37	3.6	0.26	0.34
Commercial Porous coal/platinum NPs	0.42	4.9	0.26	0.53

Conclusions:

Using of commercial coal as a material for counter electrode in DSSC offers a cheap, light weight, suitable catalytic activity and simple way of treatment cell relative to platinum counter electrode DSSC. On the other hand, depositing of the platinum NPs on the commercial coal counter electrode surface enhanced the cell efficiency by 56 % due to a reduction in cell's resistance components values. Also, this effect was due to the good conductivity and the high surface area of the porous coal/Pt NPs nanocomposite. This promising DSSC using of commercial porous coal as a counter electrode needs a further investigations and improvements in other work.

References:

1. Grätzel M, (2001), "Photoelectrochemical Cells: Insight Review Articles", Nature, **414**, 338-344.
2. Dembele K.T., Nechache R., Nikolova L., Vomiero A., Santato C., Licoccia S. and Rosei F., (2013), 'Effect of multi-walled carbon nanotubes on the stability of dye sensitized solar cells', Journal of Power Sources, **233**, 93-97.
3. Saad L., Feteha M.Y., Ebrahim Sh., Abdel Fettah T.A. and Soliman M., (2014), "Dye Sensitized Solar Cell Based on Polyaniline-Carbon Nanotubes/Graphite Composite", The Electrochemical Society, Journal of Solid State Science and Technology, **3(10)**, 55-60.
4. Yimhyun J., et al, (2012), " Highly Interconnected Ordered Mesoporous Carbon–Carbon Nanotube Nanocomposites: Pt-free, highly efficient, and durable counter electrodes for dye-sensitized solar cells", Chem. Commun., **48**, 8057-8059.
5. Xiaoru Guo , Ganhua Lu and Junhong Chen, (2015), "Graphene-Based Materials for Photoanodes in Dye-Sensitized Solar Cells" Nonmaterials and Technology, Review, **3**, Article 50.
6. Hua D., Zhaoxin W. ,Yucui G., Ahmed Sh., Bo J., Yang D., Xun H., (2014), "A Nanostructure-Based Counter Electrode for Dye-Sensitized Solar Cells by Assembly of Silver Nanoparticles", Organic Electronics, **15**, 1641–1649.
7. Yimhyun J., Jae Y. C., Jeonghun Y., Hu Y. J., Chi-Hwan H.,Yongseok J. and Sang H. J., (2012), " Highly Interconnected Ordered Mesoporous Carbon–Carbon Nanotube Nanocomposites: Pt-free, highly efficient, and durable counter electrodes for dye-sensitized solar cells", Chem. Commun., 48, 8057-8059.
8. Fan, Sh.-Q·, Fang, B. K., Jung H., Jeong, Banseok K., Chulwoo Y., JongSung K., Jaejung, (2010), "Ordered Multimodal Porous Carbon as Highly Efficient Counter Electrodes in Dye-Sensitized and Quantum-Dot Solar Cells", Journal of surfaces and colloids , **26 (16)**, 13644–13649.
9. Fang B., Kim J., Kim M., Yu J., (2010), "Hierarchical Porous Hollow Spherical Carbon with Mesoporous Shell as a Unique Cathode Catalyst 9 Support in Proton Exchange Membrane Fuel Cell", Phys Chem.; **11(9)**, 1380-7.
10. Jikun Ch., Kexin L., Yanhong L., Xiaozhi G., Dongmei L., Minghui D., (2009), "A Flexible Carbon Counter Electrode for Dye-Sensitized Solar", Carbon, **47** , 2704–2708.
11. Prakash J., Yu X., Mike R., David G., Shelia B. and Qiquan Q., (2009), "Dye-Sensitized Solar Cells Based on Low Cost Nanoscale Carbon/TiO2 Composite Counter Electrode", Energy Environ. Sci., **2**, 426-429.
12. Thi H. P., My L. P. L., Thai H. N., and Thi P. Th. N., (2014), "Synthesis, Properties and Performance of Platinum and Platinum/Carbon Nanotube Films as Cathode Materials for Dye-

Sensitized Solar Cells", ECS publication, **161(4)**, H235-H239.

13. Jikun Ch., Kexin L., Yanhong L., Xiaozhi G., Dongmei L., Minghui D., (2009), "A Flexible Carbon Counter Electrode for Dye-Sensitized Solar", Carbon, **47** , 2704–2708.
14. Tsao H. , Burschka J. , Yi Ch. , Kessler F. , Mohammad K. N. and Grätzel M., (2011), " Influence of the Interfacial Charge-transfer Resistance at the Counter Electrode in Dye-Sensitized Solar Cells Employing Cobalt Redox Shuttles " , Energy Environ. Sci., **4**, 4921-4924.
15. Ali E, Mohammad G M, MajidJ A, (2011), "Electrochemical impedance spectroscopy study on intercalation and anomalous diffusion of AlCl−4 ions into graphite in basic molten salt", Turk J Chem., **35**, 735 – 743.A.

Study of Degradability of Starch-Based Films Mixing with Nano-Titanium Dioxide

J. Komasatitaya,[1,*] S. Mataweechotikul,[1] A. Simprasert[1]
[1]King Mongkut University of Technology Thonburi, Department of Printing and Packaging Technology, Bangkok, Thailand

Abstract:
The study of degradability of starch-based films mixing with nano-Titanium dioxide was aimed to prepare the starch film which made from Tapioca flour mixed with nano-TiO2 and study the degradability of starch film by 3 and 30 percent weight of nano-TiO_2 based by starch weight. The starch film are formed into thin and thick sheets. The degradation of the nano-TiO2 and starch film was studied by weighing lost , spectrum infrared , micrograph and tensile strength. The results showed that the degradability of 30 percent of nano-TiO_2 starch film was higher than 3 percent of nano-TiO2 starch film for 1.13 of weight lost. The thin starch film was degraded more than the thick starch film and the weight of the thin film reduced approx 0.18 times of initial weight. The weight of the thick starch film reduced approx 0.16 times of initial weight. The spectrum infrared of before and after UV exposure of the nano-TiO2 starch film was changed at frequency of 3500-3250 cm-1 (OH) and 1200-1000 cm-1 (COH)

Keywords: nano TiO_2, cassava, starch, IR spectrum, degradation, photocatalyst

Introduction:

This present work was aim to study photodegradability of cassava starch film using nanoTiO_2. The starch degradation was proved by tensile property and Fourier transform infrared spectroscopy (FTIR).

Materials and Methods:

A food grade Cassava flour (Brand : Pla Mangkorn, commercially available in Thailand) was dissolved at an amount of 5% by wt in warm water at 60-70°C. After dissolving, the cassava paste was directly mixed with Titanium dioxide powder (anatase-form nanoparticle) at 3% and 30% by wt of solution using an overhead stirrer: stirring at a speed of 500 rpm. During stirring, glycerol, commercial grade, and a nonionic surface active agent, commercial grade, were added into the nanoTiO_2-cassava paste for dry film forming process as shown in Table 1.

Table 1 Ingredient of nanoTiO_2-cassava paste

Ingredients	Functions	Amount (% by wt)
Cassava flour	starch film	5
nanoTiO_2	photocatalyst degradation	3 or 30
glecerol	film plasticizer	40
surface active agent	particle dispersion	2-3 droplets
water	Dissolving cassava flour	residual

Film casting process, the nanoTiO_2-cassava paste was pouring the nanoTiO_2-cassava paste onto a petri dish and left it dry under surrounding temperature. Some of dried film having thickness in a range of 0.1-0.25 mm were separately exposed to sunlight, and under a long UVA lamp for 120 hrs of each exposure, totally. Sunlight- and UV-exposed nanoTiO_2-cassava films were investigated degradation of starch by measuring weight loss, tesing their tensile property, inspecting chemical structure using FTIR technique (PerkinElmer, SpectrumOne), and their microstructure via SEM when exposure for 56 hrs.

The sunlight- and UV-exposed nanoTiO_2-cassava film was cut into a size for tensile testing according to ISO 527-3. An universal tensile tester : Hounsfield, H5KS, clamped and pulled the samples of nanoTiO_2-cassava films at a begining speed of 10 mm/min. Tensile property was measured using QMAT PRO program.

The nanoTiO2-cassava films were brought to FTIR spectrum instrument for inspecting their chemical structures when exposed to sunlight.

Physical structure of the sunlight- and UV-exposed nanoTiO2-cassava film was observed via a scaning electron microscopy (SEM).

Results and Discussions:

There was very large difference of tensile property between the exposed films to the unexposed films and showed more difference when increased to 30% of nanoTiO2 (see Figure 1). The nanoTiO2 particle mixed in the starch film consequenly had effect to decrease film flexibility due to degradation occurred by photocatalysis. FTIR spectrum showed chemical structure of the exposed nanoTiO2-cassava films (after exposure) which showed some difference from the unexposed film (before exposure) around frequency of 3250-3500 cm^{-1}, and 1000-1200 cm^{-1}, which a peak of O-H increased and a peak of COH decreased, respectively.

Conclusions:

The nanoTiO2 effected to accerelate degradation on cassava starch film by photocatalysis because tensile property and FTIR showed some different values when compare to the blank cassava films.

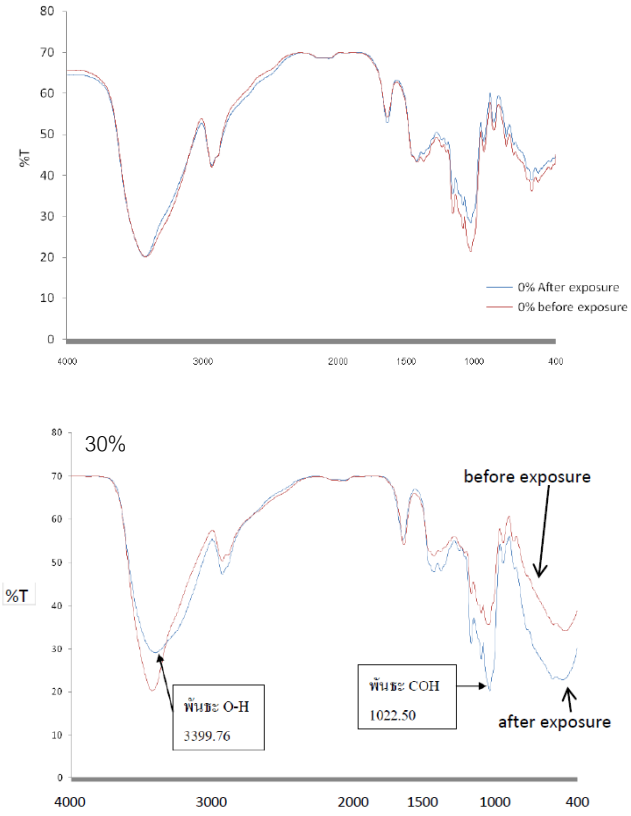

Figure 2 : FTIR spectrum of nanoTiO2-cassava films

References:

Changjun Yanga, Chuqing Gonga, Tianyou Penga, Kejian Dengb ,andLing Zana , "High photocatalytic degradation activity of the polyvinyl chloride (PVC)–vitaminC (VC)–TiO2 nano-composite film" , Journal of Hazardous Materials 178 (2010) 152–156.

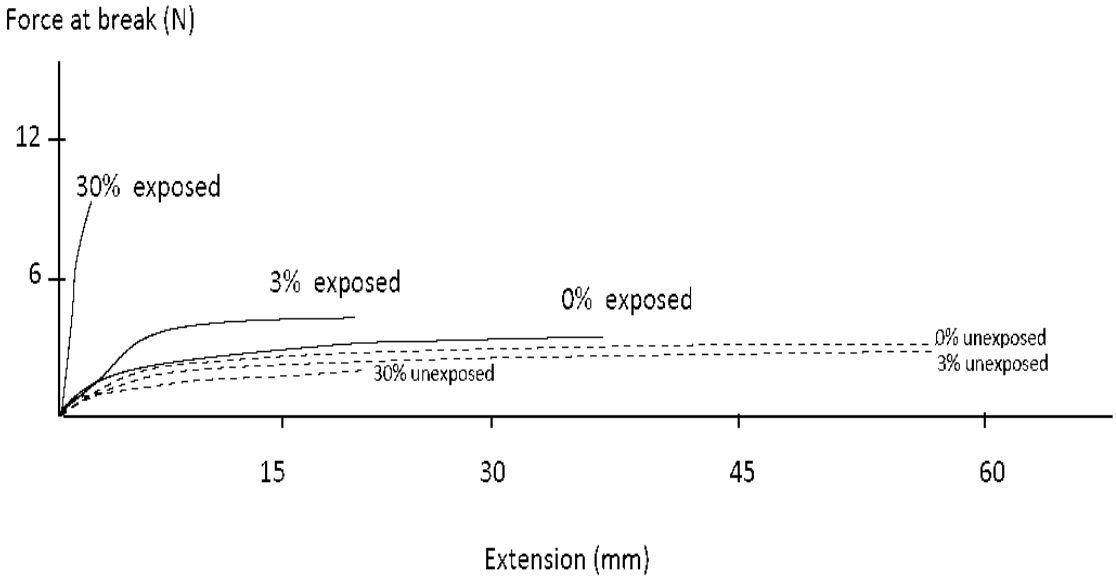

Figure 1: nanoTiO2-cassava films at 0, 3, 30% of nanoTiO2 after exposing by sunlight for 120 hrs

Plasmonic Enhancement of Light Absorption by Controlled Growth of Metallic Nanoparticles

Feras G. Alzubi,[1,*] Reem M. Alrashed,[1] and Ahmad A. Alduweesh,[1]
[1]Energy and Building Research Center, Kuwait Institute for Scientific Research, Safat 13109, Kuwait

Abstract:

In this work, we report the fabrication of Silver (Ag) and Titanium (Ti) nanoparticles (NPs) by electron-beam physical vapor deposition (e-beam PVD) technique. While as-deposited samples showed smooth surfaces with no presence of NPs, thermally annealed samples showed formation of uniform NPs recognizable in the AFM topography images. Ag and Ti NPs diameters ranged from 50 to 100 nm. In case of Ag NPs, about 90% of the formed NPs have height between 5 and 6.5 nm reflecting a uniform formation of the NPs by PVD and annealing processes. Absorption spectra of annealed samples showed surface plasmonic resonance (SPR) peak around 308 nm for Ti samples which reflects an enhancement in the spectra comparing to as-deposited films. Our study shows a possibility of controlling NPs properties through the processing conditions of NPs.

Keywords*:* Metallic Nanoparticles, PVD, AFM, Absorption Spectra, Thermal Annealing.

Introduction:

Metallic nanoparticles (NPs) have gained more interest in many optical applications over the last decade because of their novel properties [1,2]. For example, optical properties such as enhancement of light absorption as a result of surface Plasmon presence [3,4]. Such unique properties are a result of the variation in size and shape of NPs which can be controlled through governing the variation in fabrication parameters such as, deposition rate, deposited film thickness, thermal annealing temperature and time. Moreover, metallic thin films react differently to these fabrication parameters due to their different physical and thermal properties such as surface energy and thermal conductivity.

Experimental:

Thin films of Ag and Ti were deposited on Si and quartz substrates by e-beam PVD inside high vacuum chamber with pressure ~ 10^{-6} Torr. Deposition rate was 0.1 Å/s. Film thickness was 4 nm for all samples. To form the nanoparticles, deposition process was followed by thermal annealing at 800 ^{o}C under Argon inert atmospheric pressure for 30 minutes. UV-Vis Shimadzu and atomic force microscopy (AFM) by Agility were utilized to investigate the formation of the nanoparticles (Si-substrates) and the related absorption enhancement (Quartz-substrates) for Ag and Ti annealed thin-films samples compared to as-deposited ones.

Results and Discussions

Figure 1 shows 5x5 μm topography surfaces by AFM of As-deposited thin films of Ti and Ag. Surfaces are very smooth with very low value of roughness about 0.05 nm and 0.14 nm for (a) titanium and (b) silver, respectively. Figures 2 (a) and (b) show annealed surfaces of Ti and Ag NPs on Si substrate, respectively, illustrating individual NPs. Ti and Ag NPs are clear in topography images compared to as deposited thin film in Figure 1.

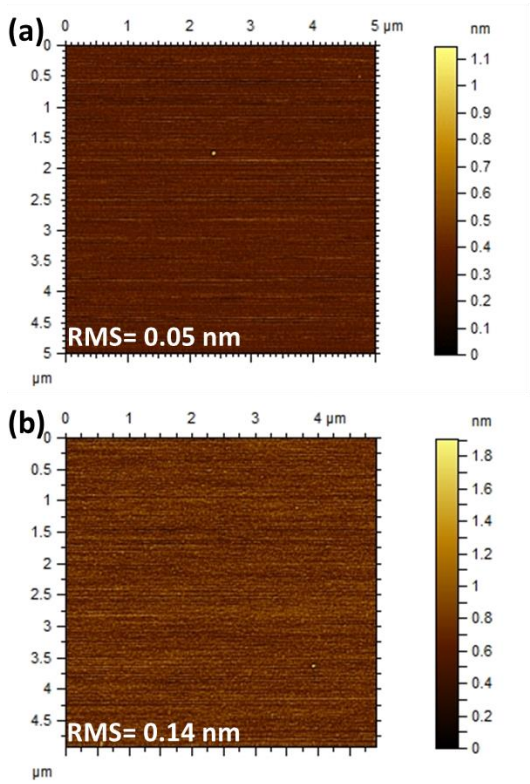

Figure 1: Topography AFM images of As-deposited 4 nm thickness of (a) Ti and (b) Ag thin-films.

PVD process followed by thermal annealing has led to a uniform formation and distribution of Ag about 20% and Ti about 60% of NPs with respect to bare substrate. In case of Ag NPs, they are more clear and larger with average diameter 90 nm and particles separation of 180 nm while average diameter is 55 nm in Ti case with separation of 24 nm. Roughness of Ag surface is higher ~ 0.69 nm than Ti ~ 0.32 nm due to larger Ag NPs. About 90% of the formed NPs have height between 5 and 6.5 nm in Ag case while it is between 1.3 to 3.1 nm for Ti NPs. This clear difference in size and separation between two materials can be a result of larger thermal conductivity for Ag (429 W/m K) than Ti (31 w/m K). This allows Ag material to be more thermally active. Other reason can be a difference in the surface energy between both materials which affects the adhesion of the metal particles and their physical interaction with the substrate. Lower surface energy for Ag, (890 mJ/m^2), leads to lower interaction with the substrate and hence higher among the Ag NPs.

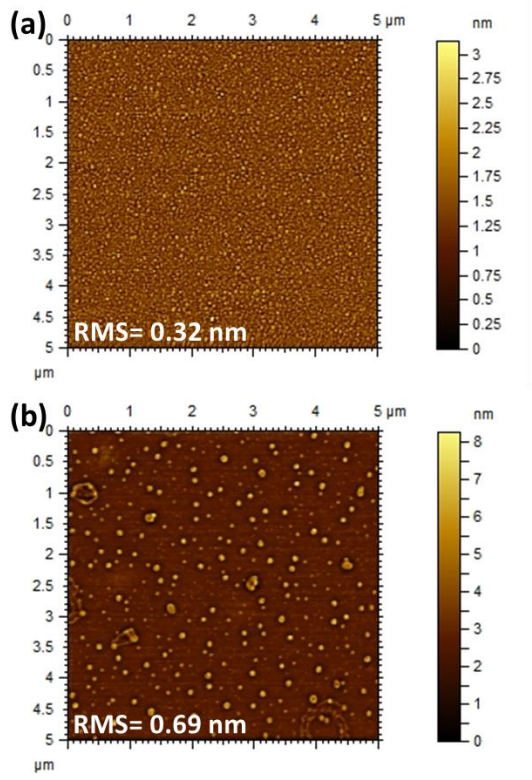

Figure 2: Topography of 4 nm annealed samples at 800 ^{o}C for 30 minutes of (a) Ti and (b) Ag.

Figure 3 shows surface plasmonic resonance peak at 308 nm which is generated due to separated individual NPs evoluted from the Ti thin-film compared to as deposited. Since NPs work as wave guides in the film, then a shift of the absorption peak is expected with size variation. More experimental procedure however is needed to proof that this peak is not a result of a band gap created in case of formation of TiO_2.

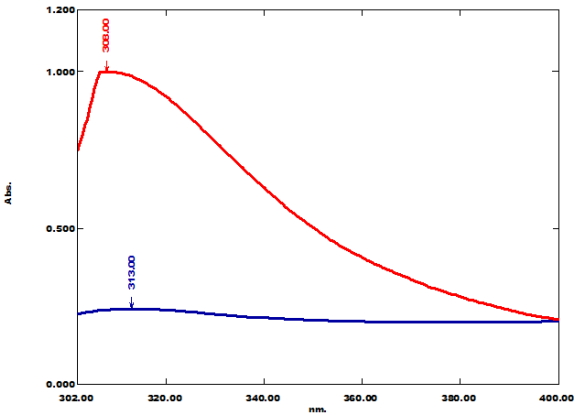

Figure 3: Absorption spectra for Ti annealed (red) vs. un-annealed (blue) samples.

Conclusions:

We have successfully deposited ultra-thin films about 4 nm of Ti and Ag materials and formed NPs of size between 50 and 100 nm by e-beam PVD followed by thermal annealing. Larger NPs size for Ag and higher NPs coverage for Ti were observed. Difference in size and coverage is thought to be as a result of different thermal conductivity and surface energy of both materials. An enhancement in the absorption spectra around 308 nm was observed for annealed Ti samples comparing to as-deposited films. This work provides an opportunity to tune the structural and optical properties of NPs by controlling the processing conditions.

Acknowledgment:

Support is received by Kuwait Institute for Scientific Research (KISR) and project (P-KISR-06-04 Kuwait government). The financial support is from KFAS for publishing this work.

References:

[1] Kumar, S. S., Venkateswarlu, P., Rao, V. R., and Rao, G. N. 2013. *International Nano Lett.* **3**: 30, 1-6.
[2] Atwater, H. A., and Polman, A. 2010. *Nature Mater.* **9**: 205-213.
[3] Willets K. A., and Van Dyune R. P. 2007. *Ann. Rev. Phys. Chem.* **58:** 267-297
[4] Pan, T.-S., Sharma, J., Chu, C.-C., Tai, Y. 2014. *Journal of Nanoparticle Research* 16.10: 1-10

Photodegradation of oflaxacin with Nano-GO/M composite and its reuse

P. Alicanoglu,[1*] D.T. Sponza[2]

[1]Pamukkale University, Department of Environmental Engineering, Denizli, Turkey
[2]Dokuz Eylul University, Department of Environmental Engineering, Izmir, Turkey

Abstract:

Among widespread used antibiotics, fluoroquinolone antibiotics (FQ) are an important type with undetectable biodegradability. In receiving environments, low concentrations of antibiotic traces can cause resistance to microorganisms. Graphene oxide (GO) with large quantities of oxygen atoms on the surface are present in the forms of epoxy, hydroxyl, and carboxyl groups. These functional groups make GO hydrophilic and suitable to be an adsorbent. Especially, some iron oxide nanomaterials composited with GO as magnetic adsorbents were a better solution. Thus, the combination of GO with magnetic nanoparticles (Nano-GO/M) to produce a magnetic graphene-based composite and it will be separated from the matrix rapidly and easily by an external magnetic field. This study aims to investigate the removal of Ofloxacin (OFL) at increasing concentrations (1, 3, 5, 25, 100, 500 and 1000 mg/L), at increasing irradiation times and at acidic (pH=4), neutral and alkaline (pH=10) conditions via photodegredation process by using UV light and sunlight. Also photodegredation products of OFL POF (9-piperazino ofloxacin) and MOF (des-methyl ofloxacin) were investigated during the UV light process. The Nano-GO/M was prepared under laboratory conditions. The surface properties of the Nano-GO/M composite was investigated by a scanning electron microscope (SEM), fourier transform infrared spectroscopy (FTIR) and x-ray diffraction (XRD). For maximum OFL removal (96%) the optimum Nano-GO/M concentration was found to be 0.5 g/L at 1 mg/L OFL concentration, at pH of 6.5, at a UV power of 300 W and at a temperature of 21°C after 60 min retention time by UV light. For maximum OFL removal (82%) the optimum Nano-GO/M concentration was found to be 2 g/L at 1 mg/L OFL concentration, at pH of 6.5, after 350 min irradiation time, at 35°C ± 5°C and with a power of 80 W sunlight. In this study, six sequential treatment steps were investigated for determination of reusability of Nano-GO/M composite. 0.5 g/L Nano-GO/M composite were used for six times under under specified operational conditions (60 min, 300 W UV, 100 mg/L OFL, pH 6.5 and room temperature).

Keywords: Fluoroquinolone, Ofloxacin, Graphene, Magnetite, Nano composite, Photodegradation, UV irradiation, Sunlight

Introduction:

There has been an increasing concern in recent years about the occurrence, fate, and adverse effects of pharmaceutical residues in the aquatic environment [1]. Antibiotics are most widely and frequently used ones all over the World. As a consequence of their poor metabolization and their incomplete removal in sewage treatment plants (STPs), antibiotics are continuously released into the aquatic environment [2]. Pharmaceuticals are designed to have physiological effect on humans and animals at trace concentrations. These compounds are persistent against biological degradation and natural attenuation and, therefore, may remain in the environment for a long time [3]. Many studies have reported the presence of PPCPs at concentrations ranging between mg/L and ng/L levels in aquatic environments worldwide [3]. Although antibiotics are found in the environment at sub-inhibitory levels, relatively low concentrations of them can still promote bacterial resistance [4]. Fluoroquinolones (FQs) are broad-spectrum antibacterial agents widely used for treating bacterial infections [5]. Their major mode of action is the inhibition of DNA replication in bacteria via interference of the normal function of DNA topoisomerase [5]. OFL is one of the most frequently used fluorinated quinolone-type antibiotics with a broad spectrum of activity against both Gram-positive and Gram-negative bacteria [6]. In recent years many works purposed different methods for removing OFL such as sonophotocatalytic degradation [7], solar fenton [5], photodegradation [3], adsorption [8]. Graphene, a new member of carbon materials, has been used as a support material for photocata-

lysts owing to its unique physical structure, large surface area, superior electrical conductivity and excellent adsorption capacity [9]. In the field of photocatalysis, the introduction of graphene is a very popular method to enhance the photocatalytic performance of conventional photocatalysts [10]. Thanks to the scaled-up and reliable production of graphene derivatives, such as graphene oxide (GO), it is possible to synthesize a wide range of graphene-based functional materials for various applications [11]. Magnetite (Fe_3O_4) nanoparticles have drawn considerable attention because of the fundamental scientific interest and the promising applications in magnetic fluids, catalysis, sensors, biomedicine, spintronics, magnetic recording devices, and environmental remediation [12]. Additionally, Fe_3O_4 nanoparticles also show advantages such as low toxicity, low cost, and eco-friendliness. Thus, the combination of graphene with magnetic nanoparticles to produce a magnetic graphene-based composite would provide a new, functional hybrid with synergistic or complementary behavior between each constituent, and thus will have great advantages for above-mentioned applications. In particular, the magnetic nanoparticles in such composite system could also serve as a stabilizer against the aggregation of individual graphene sheets due to a strong van der Waals interaction between graphene layers [11]. In this study, the removal of OFL at increasing concentrations (1, 3, 5, 25, 100, 500 and 1000 mg/L), at increasing irradiation times and at acidic (pH=4), neutral and alkaline (pH=10) conditions via photodegredation process by using UV light and sunlight. Also photodegredation products of OFL POF (9-piperazino ofloxacin) and MOF (des-methyl ofloxacin) were investigated during the UV light process.

Materials and Methods:

2.1. Reagents and Chemicals

OFL (>98%, Bayer AG, Germany) and its metabolites (POF- 9-piperazino ofloxacin (>98%, Bayer AG, Germany) and MOF- des-methyl ofloxacin (>98%, Bayer AG, Germany), Graphene (Ege Nanotek Kimya Sanayi Ltd. Şti.) and Magnetite were bought externally. Natural magnetite was purchased from Synergy Laboratory Products Ltd., Turkey. Demineralized water was used for preparation of reagents solutions. 0.1 M HCl and 0.1 M NaOH are used to adjust pH vales of OFL solutions.

2.2. Experimental Procedures

2.2.1. Quartz Glass Reactors for Photocatalytic Processes

Photocatalytic experiments were conducted in a system which is well-sealed and constructed with stainless steel material. Quartz glass reactors and 10 UV lambs (each one has a power of 30 watt) were used for photocatalytic experiments. The dimensions of the quartz glass reactors were 38 and 3.5 cm. The experiments were performed at different initial concentration of and the pH of the reaction mixture was adjusted from 4 to 6.5 and 10 using 0.1 M of HCL and NaOH solution. Photocatalytic experiments were carried out with a known quantity of Nano-GO/M composite varying between 0.5 g/L, 2 g/L and 10 g/L at different irradiations times (15, 30, 60, 90 and 120 min,). Then, they were irradiated in a closed isolated device system. And also, photocatalytic degradation experiments were carried out under sunlight in the same quartz glass reactors which have the same dimensions. Experiments were carried out at different retention times of the day (30, 120, 250, 350 min and 24 h) and different initial concentration of OFL and the reactors were placed at an angle of 90 degrees to the sun at hours 08.00-17.00. Experiments were carried out at the same Nano-GO/M composite concentrations varying between 0.5 g/L, 2 g/L, 3.5 g/L, 5 g/L and 10 g/L. Samples were separated magnetically and were analyzed in HPLC. The sunlight power was measures as 80 W with a lightmeter.

2.3. The synthesis of Nano-GO/M Composite

GO was synthesized from natural graphite powder by a modified Hummers method [13]. 120 mL of H_2SO_4 was added into 5 g of graphene and 2.5 g of $NaNO_3$ containing flask and followed by stirring the mixture for 30 min inside a water bath. Next, 15 g of $KMnO_4$ was added gradually to the mixture. The reaction temperature was kept below 20°C during this step. The mixture was stirred at room temperature overnight, continuously. After this period, 150 mL of H_2O was slowly added under stirring. The

mixture was stirred for one day at 98°C. Following, 50 mL of 30% H_2O_2 was added to the final mixture. For purification, the mixture was washed with 5% HCl and deionized (DI) water for many times and then, centrifugated and dried under vacuum. The final product GO was obtained as a solid phase. The Fe_3O_4 Nano particles were dispersed in 25 mL of water and added to 50 mL of GO aqueous solution, drop by drop (1 mg/mL). The mixture was stirred at 60 °C through 1 h. The product was collected by using a magnet and washed with water three times. Finally, the Fe_3O_4/GO composite was obtained [14].

2.4. Analytical Procedure

HPLC Analysis: A HPLC Degasser (Agilent 1100), a HPLC Pump (Agilent 1100), a HPLC Auto-Sampler (Agilent 1100), a HPLC Column Oven (Agilent 1100) and a HPLC Diode-Array-Detector (DAD) (Agilent 1100) and C-18 (5 µm, 4.6 mm 250 mm, Thermo Scientific) column were used. The analyte was separated at ambient temperature. The mobile phase consisted of acetonitrile (18:82, v/v). The aqueous component of the mobile phase was prepared by dissolving 1.0 g of ammonium acetate and 1.75 g of potassium perchlorate by ultrasonic treatment in 325 mL of water and the pH was adjusted to 3.50 using 85% orthophosphoric acid. The column was equilibrated to stable baseline at a flow rate of 1.0 mL min^{-1}, maintaining the temperature of the column at 45 °C. Detection was at 294 nm [6]. OFL, (9-piperazino ofloxacin) and MOF (des-methyl ofloxacin) metabolites peaks were seen at 10.01, 7.99 and 9.68 min. Also C8 column was used for the analysis.

2.5. Instrumental Characterization

2.5.1. X-ray diffraction (XRD)

XRD measurements were carried out with the D/max-2200 PC (Rigaku, Japan), using Cu-Ka radiation.

2.5.2. Fourier transform infrared (FT-IR)

FT- IR spectra's of Nano-GO/M after different conditions applied were measured with the Perkin Elmer FTIR System Spectrum BX with the KBr method.

2.5.3. SEM

The morphological and structural observation was made on a scanning electron microscope VegaII/LMU (Tescan, Czech Republic)

2.6. Photooxidation Kinetic Studies

2.6.1. Zero-Order Kinetics

A zero order reaction has a rate that is independent of the concentration of the reactants. Increasing the concentration of the reacting species will not speed up the rate of the reaction i.e. the amount of substance reacted is proportional to the time. Zero order reactions are typically found when a material that is required for the reaction to proceed, such as a surface or a catalyst, is saturated by the reactants. The rate law for a zero order reaction is:

$$r=k \qquad \text{Eq.(1)}$$

where r is the reaction rate and k is the reaction rate coefficient with units of concentration or time. If, and only if, this zeroth order reaction;

1) occurs in a closed system,

2) there is no net build-up of intermediates,

3) there are no other reactions occurring, it can be shown by solving a mass balance equation for the system that:

$$r = -\frac{d[A]}{dt} = k$$

If this differential equation is integrated it gives an equation often called the integrated zero order rate law.

$$[A]_t = -kt + [A]_0 \qquad \text{Eq.(2)}$$

where $[A]_t$ represents the concentration of the chemical of interest at a particular time, and $[A]_0$ represents the initial concentration.

Eq.(2) is in the form y = mx+b where slope = m = -k and the y-intercept = b = $[A]_0$

where A_0 is the influent concentration of OFL and A is the effluent concentration of OFL (mg/L) at any time t (min), respectively and k_0

is the constant of pseudo-zero-order reaction (min^{-1}).

2.6.2. First-Order Kinetics

A first order reaction depends on the concentration of only one reactant (a unimolecular reaction). Other reactants can be present, but each will be zero order. The rate law for a reaction that is first order with respect to a reactant A is;

$$-d[A] / dt = r = k[A] \quad \text{Eq.(3)}$$

k is the first order rate constant, which has units of 1/s. The integrated first order rate law is:

$$\ln[A] = -kt + \ln[A]_0 \quad \text{Eq.(4)}$$

A plot of $\ln[A]_0$ vs. time *t* gives a straight line with a slope of -k [15].

Where A_0 is the influent concentration of OFL (mg/L) and A is the effluent concentration of OFL (mg/L) at any time t (min), respectively and k_1 is the constant of pseudo-firs-order reaction (min^{-1}).

2.6.3. Second-Order Kinetics

A second order reaction depends on the concentrations of one second order reactant, or two first order reactants [15].

Its reaction rate is given by:

$$\frac{1}{[A]} = \frac{1}{[A]_0} + kt \quad \text{Eq.(5)}$$

where A_0 is the influent concentration of OFL (mg/L) and A is the effluent concentration of OFL (mg/L) at any time t (min), respectively and k_2 is the constant of pseudo-second-order reaction (min^{-1}).

3. Results and Discussions

3.1 Psychochemical Properties of Nano-GO/M

3.1.1 FTIR analysis of Nano-GO/M composite

Figure 1. shows the peaks of GO plotted between wave number $(cm)^{-1}$ and percent transmittance (A-%). In the spectrum of Nano-GO/M, the peaks at 2359, 1568 cm^{-1} are the characteristics spectrum of benzene ring of Nano-GO/M while the peak at 1073 cm^{-1} is the characteristic spectrum of the C–OH rings of Nano-GO/M. This confirms the presence of graphene oxide peak at 600 cm^{-1} which is the characteristics of Fe_3O_4 giving an evidence of the successful preparation of the Nano-GO/M as reported by Huamin et al. [16].

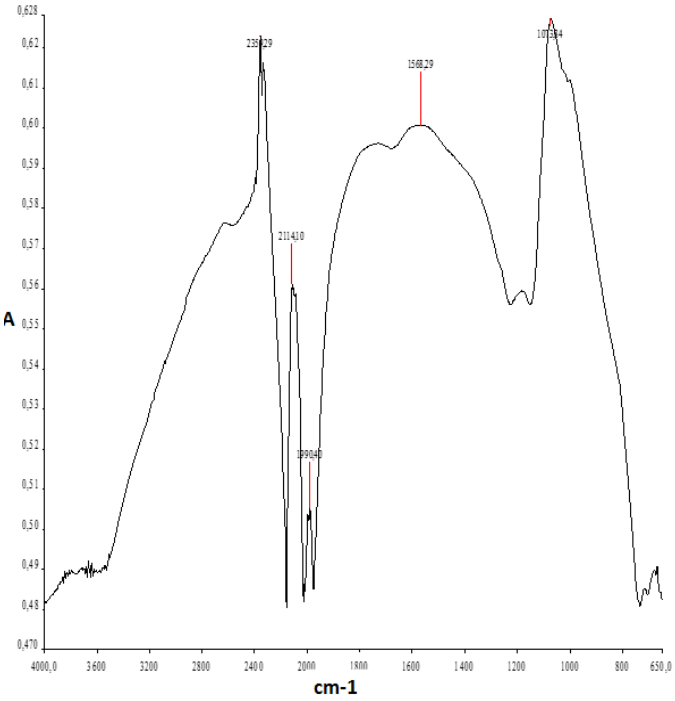

Figure 1. FTIR analysis of raw Nano-GO/M (cm^{-1}: wave number and A-%: percent transmittance)

OFL photooxidation experiments were conducted in optimal conditions. In UV oxidation process, experiments were realized at optimum Nano-GO/M concentration (0.5 g/L), for initial 100 mg/L OFL concentration, at a pH of 6.5 and under 300 W UV light after 60 min irradiation time at 21ºC. In sunlight oxidation process, experiments were realized at optimum Nano-GO/M concentration (2 g/L), for initial 100 mg/L OFL concentration, at a pH of 6.5 and under 80 W sunlight after 350 min irradiation time and at 35ºC±5. Figure 2. shows the FTIR analysis of Nano-GO/M composite after OFL treatment with UV. The maximum peaks obtained in this figure are similar to the nano composite before UV treatment. Condensation

of Nano-GO/M composite remained almost the same after UV treatment. After sunlight experiments, Nano-GO/M structure has turned to amorphous shape (Figure 3.). It may be due to sunlight has wide spectrum in comparison to UV light and thus, sunlight might be changed the structure of Nano-GO/M.

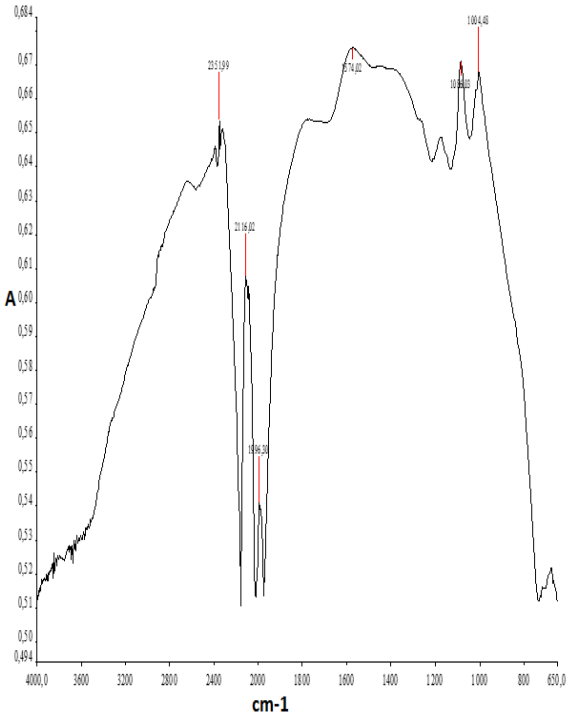

Figure 2. FTIR analysis of Nano-GO/M (0.5 g/L) after UV treatment (300 W) of OFL (100 mg/L), at pH=6.5, at 21ºC after 60 min irradiation time (cm^{-1}: wave number and A-%: percent transmittance)

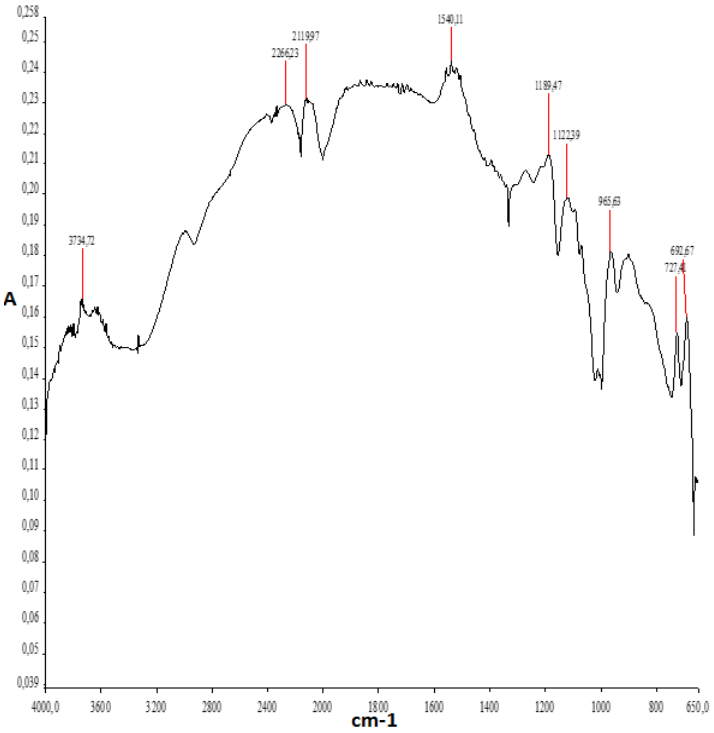

Figure 3. FTIR analysis of Nano-GO/M (2 g/L) after sunlight treatment (80 W) of OFL (100 mg/L), at pH=6.5, at 35ºC±5 after 350 min irradiation time (cm^{-1}: wave number and A-%: percent transmittance)

3.1.2 XRD analysis of Nano-GO/M

The XRD spectra of magnetite nanoparticles, GO, raw Nano-GO/M composite and Nano-GO/M composite after OFL treatment under UV irradiation with 100 mg/L OFL concentration. As shown in Figure 4. series of characteristic peaks at the ranges at 2θ = 18-20°, 30-32°, 35-37°, 43-45°, 53-55°, 57-59°, and 62-64° versus intensities (cps) were observed. These peaks were well matched of the crystal planes of Fe_3O_4. Experiments were realized at optimum Nano-GO/M concentration (0.5 g/L), for initial 100 mg/L OFL concentration, at a pH of 6.5 and under 300 W UV light after 60 min irradiation time. The characteristic peaks of Nano-GO/M did not change considerably after UV irradiation. In this aspect, Nano-GO/M composite can be used again and again.

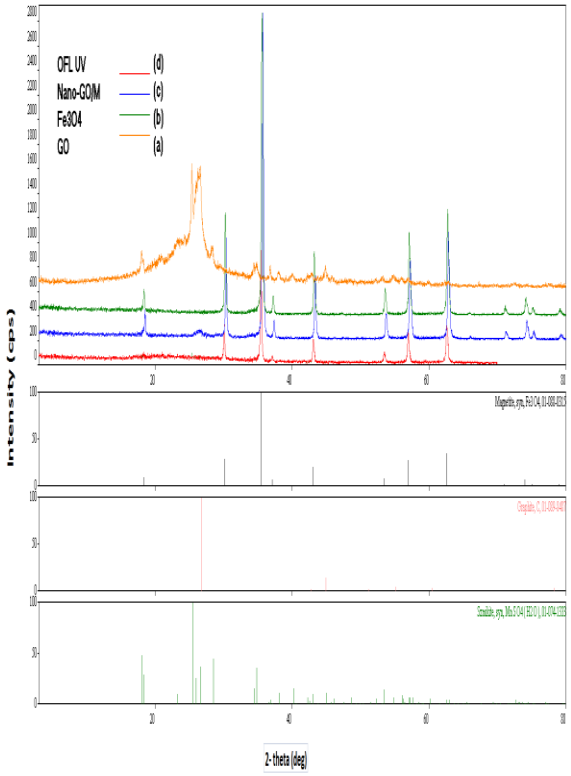

Figure 4. XRD analysis of GO (a), Fe_3O_4 (b) and Nano-GO/M composite before(c) and Nano-GO/M (0.5 g/L) composite after UV irradiation (60 min-300 W), with 100 mg/L OFL concentration (d) at pH=6.5

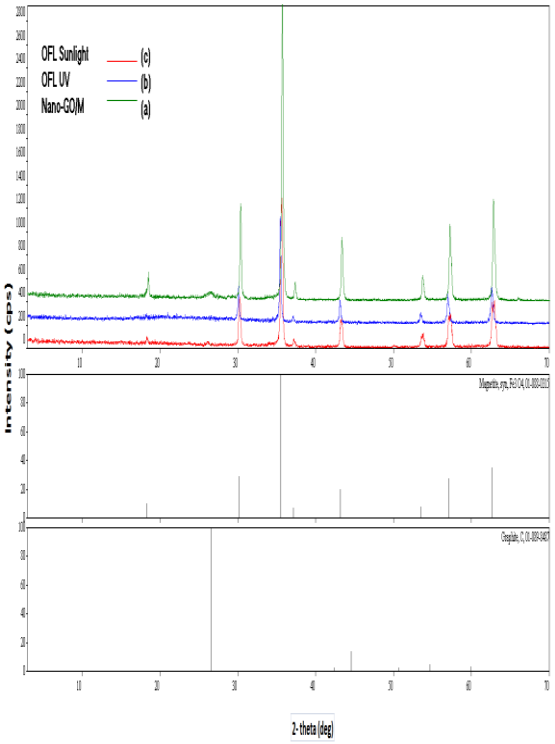

Figure 5. XRD analysis raw Nano-GO/M composite (a), Nano-GO/M (0.5 g/L) composite after UV irradiation (60 min-300 W) (b), Nano-GO/M (2 g/L) composite after sunlight (350 min- 80 W) with 100 mg/L OFL concentration (c) at pH=6.5

The comparison of XRD spectra of raw Nano-GO/M composite and Nano-GO/M composite after OFL treatment under UV irradiation (60 min- 300 W) and sunlight (350 min- 80 W) with 100 mg/L OFL concentration are shown in Figure 5. After UV and sunlight irradiations the crystal planes of Fe_3O_4 remained almost same. The structure of Nano-GO/M composite did not change considerably. UV experiments were realized at optimum Nano-GO/M concentration (0.5 g/L), for initial 100 mg/L OFL concentration, at a pH of 6.5 and under 300 W UV light after 60 min irradiation time. Sunlight experiments were realized at optimum Nano-GO/M concentration (2 g/L), for initial 100 mg/L OFL concentration, at a pH of 6.5 and under 80 W UV light after 350 min irradiation time. The characteristic peaks of Nano-GO/M did not change considerably after UV and sunlight irradiation.

3.1.3 SEM Imagines of Nano-GO/M

The SEM images of GO, Fe_3O_4, raw Nano-GO/M composite are shown in Figure 6., Figure 7. and Figure 8., respectively. From Figure 8., it can be clearly seen that, many Fe_3O_4 microspheres were firmly anchored on both sides of the wrinkled graphene sheets. The graphene layers might contribute to hinder the Fe_3O_4 microspheres from aggregation as reported by Tang et al. [17].

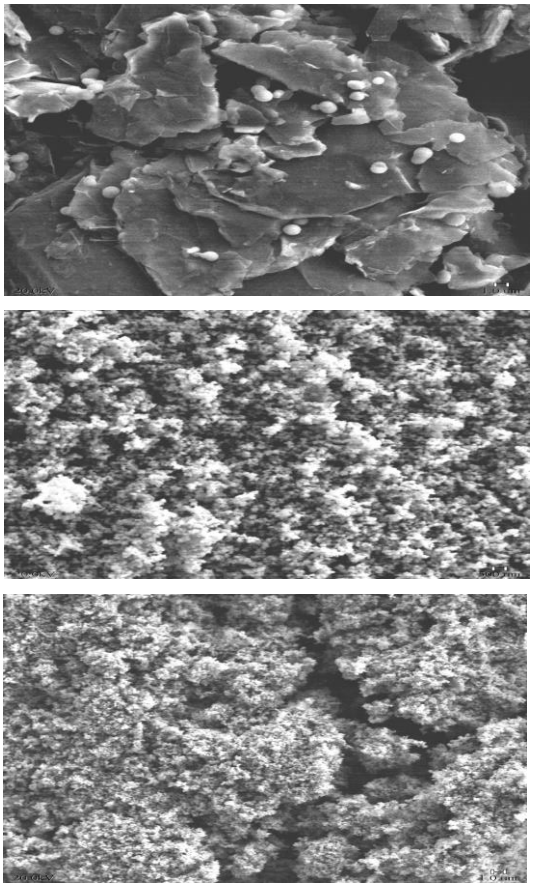

Figure 6,7 and 8. SEM imagine of synthesized GO(1µm), Fe_3O_4 (500 nm) and raw Nano-GO/M(1µm), respectively.

OFL photooxidation experiments were conducted in optimal conditions. In UV oxidation process, experiments were realized at optimum Nano-GO/M concentration (0.5 g/L), for initial 100 mg/L OFL concentration, at a pH of 6.5 and under 300 W UV light after 60 min irradiation time at 21ºC. In sunlight oxidation process, experiments were realized at optimum Nano-GO/M concentration (2 g/L), for initial 100 mg/L OFL concentration, at a pH of 6.5 and under 80 W sunlight after 350 min irradiation time and at 35ºC±5. Figure 9. shows the SEM imagine of Nano-GO/M composite after OFL treatment with UV. Color of Nano-GO/M composite turns to grey after treatment of OFL under UV and sunlight treatment surface of composite fills with OFL as illustrated in Figure 9. and Figure 10. Crystalline structure of Nano-GO/M composite turns to amorphous form due to filling of pollutants on to surface of Nano-GO/M. The average particle size was measured about 400 nm and 250 µm for Nano-GO/M composite and UV irradiated Nano-GO/M composite, respectively. After sunlight irradiation average particle size was measured about 400 µm.

3.2 Removal of OFL Under Photocatalytic Studies

3.2.1 Photodegradation of OFL Under UV light

3.2.1.1 *Effects of Nano-GO/M Composite Concentrations On The Photocatalytic Treatment of OFL Under Uv light*

OFL were treated via photodegradation under UV light power in the presence of a nano composite (Nano-GO/M*)* generated under laboratory conditions. Nano particles concentration is an important parameter for the treatment of

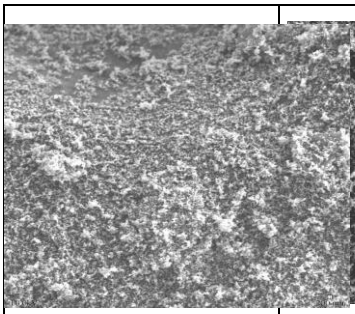

Figure 9. SEM imagine of Nano-GO/M (0.5 g/L) after UV treatment

(300 W) of OFL (100 mg/L), at pH=6.5, at 21ºC after 60 min irradiation time (200 nm)

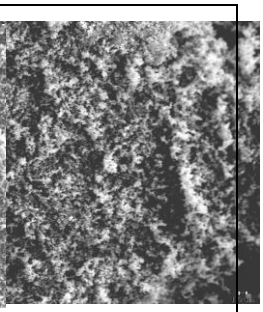

Figure 10. SEM imagine of Nano-GO/M (2 g/L) after sunlight treatment (80 W) of OFL (100 mg/L), at pH=6.5, at 35ºC±5 after 350 min irradiation time (1 µm)

OFL. In order to determine the effects of increasing Nano-GO/M concentrations on the treatment of 1, 3, 5, 25, 100, 500 and 1000 mg/L OFL; the effects of 0.5 g/L, 2 g/L, 10 g/L Nano-GO/M composite concentrations were researched. Preliminary experiments showed that among the irradiation times that are tested, the maximum OFL removal was obtained after 60 min irradiation time (data not shown). Therefore, all experiments were realized after 60 min irradiation time, at 21°C (room temperature) and at original pH (6.5) of OFL solution and with a power of 300 W UV light. Figure 11. summarizes the photocatalytic treatment efficiencies of OFL at 0.5, 2 and 10 g/L Nano-GO/M, at increasing OFL concentrations (1, 3, 5, 25, 100, 500 and 1000 mg/L). The maximum removal efficiency (96%) of 1 mg/L OFL was found at 0.5 g/L Nano-GO/M

composite (Figure 11). Similarly, 97 % OFL (1 mg/L) photooxidation yield was obtained for 2 g/L Nano-GO/M (Figure 11). With 10 g/L Nano-GO/M composite concentration lower removal efficiency (87%) was obtained at the same operational conditions (Figure 11). Increasing the amount of photocatalyst from 0.5 g/L to 10 g/L resulted in decreasing the photocatalytic treatment efficiency from 96% to 87% at the irradiation time of 60 min for 1 mg/L of OFL initial solution, respectively. By increasing the catalyst dosage, the surface area was increased, leading to an increase in the production of reactive species [18]. However, more Nano-GO/M dosage would also induce greater aggregation of the catalyst and decrease the total active surface area, thereby leading to a reduction in the photocatalytic treatment efficiency. Moreover, due to an increase in the turbidity of the solution, reduction in the degree of light penetration through the solution could take place [19]. Therefore, other experiments were carried out with 0.5 g/L Nano-GO/M to avoid the excessive usage of the catalyst. It is clear that the photodegradation of OFL decreases with increasing concentration of the OFL. By increasing the concentration of OFL, more OFL molecules are adsorbed at the Nano-GO/M surface, resulting in occupation of the catalyst active sites. Thus, decreasing the OH^0 radicals generated at the photocatalyst surface. Furthermore, the large amount of the adsorbed OFL is thought to inhibit the reaction between the OFL molecules and photogenerated holes or the hydroxyl radicals [20].

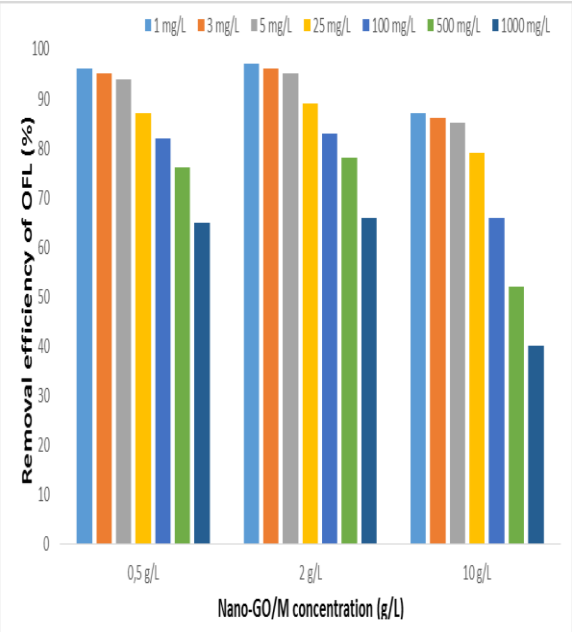

Figure 11. Effect of increasing concentration of Nano-GO/M (0.5, 2 and 10 g/L) on the yields of OFL removal via photooxidation for increasing OFL concentration at pH=6.5, at 21°C and 60 min irradiation time

3.2.1.2 *Effect of Irradiation Time On The Photocatalytic Treatment of OFL Under Uv light*

After determining the optimum concentration of Nano-GO/M (0.5 g/L), it was decided to investigate the effect of irradiation time on the photocatalytic treatment of constant OFL (1 mg/L) at increasing irradiation times (15, 30, 60, 90 and 120 min) at pH = 6.5, at a temperature of 21°C and with a power of 300 W UV light. As the irradiation time was increased from 15 min to 30 min, 60 min and 90 min the OFL removals increased slightly from 88% to 90% and to 96% and 97% for initial OFL concentration of 1 mg/L (Figure 12). Further increase in irradiation time from 90 min to 120 min decreased the OFL removal yield from 97% to 89%. As a result, in this study the optimum irradiation time for maximum OFL removal (96%) was found to be 60 min.

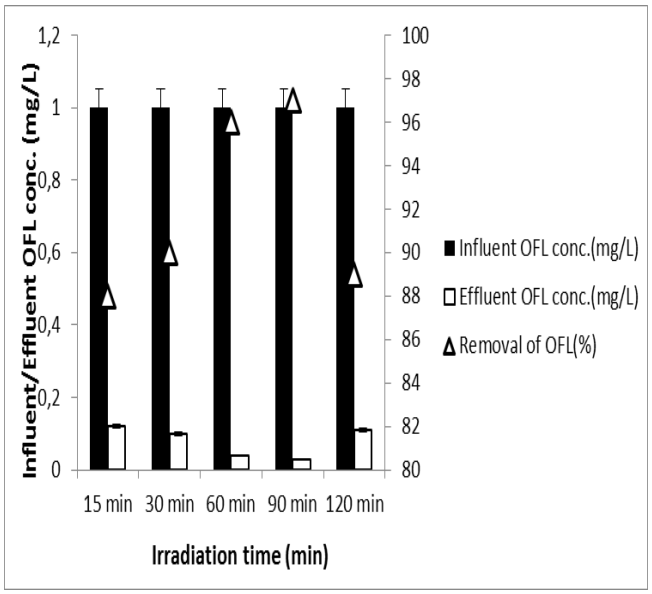

Figure 12. Effect of irradiation time on the yields of constant OFL concentration (1 mg/L), at a constant Nano-GO/M concentration (0.5 g/L), at a pH of 6.5 and at 21°C and with a power of 300 W UV light

3.2.1.3 Effect of pH on the Photocatalytic Treatment of OFL with Nano-GO/M composite Under UV light

pH is an important parameter that can affect photocatalytic reactions. In this study the degradation of OFL was evaluated at different pH values (4, 6.5, and 10) as shown in Figure 13. The effects of pH on the removal of increasing OFL concentrations (1, 3, 5, 25, 100 , 500 and 1000 mg/L) were studied under acidic, neutral and alkaline pHs (4, 6.5 and 10) at an irradiation time of 60 min, at a Nano-GO/M concentration of 0.5 g/L and at 21°C. Consequently, the maximum OFL (initial OFL concentration was 1 mg/L) photocatalytic removal yield was obtained at pH 6.5 (96%), but at alkaline pH lowest OFL photocatalytic removal yield (60%) was obtained whilst at acidic pH lower OFL adsorption yield was obtained (79%).

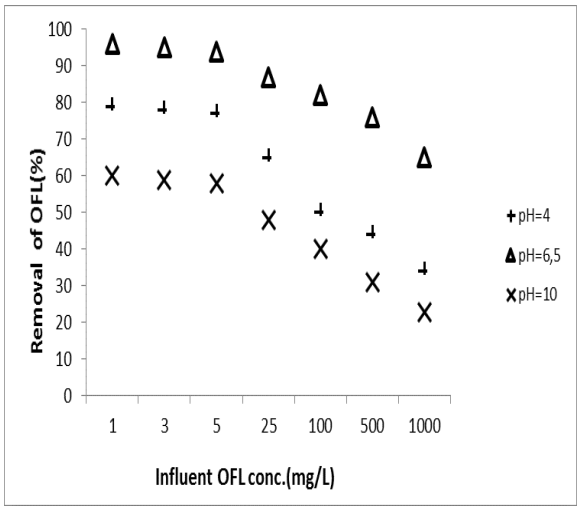

Figure 13. Effect of different pHs (4, 6.5 and 10) on the yield of OFL photooxidation efficiency at a Nano-GO/M concentration of 0.5 g/L, at 21°C and 60 min irradiation time and with a power of 300 W UV light

pH changes can influence OFL molecule adsorption on the Nano-GO/M surface, which is decisive for the occurrence of photocatalytic oxidation reactions. The zero charge point of (pH_{pzc}) Nano-GO/M is at pH ≈ 5.5 [21]. Thus the surface of Nano-GO/M was positively charged when pH < pH_{pzc}, and negatively charged when pH > pH_{pzc}. OFL is positively charged at pH values lower than the pKa1 (6.05), negatively charged at pH values above the pKa2 (8.11), and neutral at pH values between pKa1 and pKa2 [22]. Therefore, pH 4 and 10 are not suitable for OFL adsorption on the Nano-GO/M surface, since there is electronic repulsion between the charges of the compound and the catalyst with the same sign. At pH 6.5, both the Nano-GO/M molecule and the OFL are in their neutral forms, and no repulsion occurs between them. Photocatalysis degradation efficiencies at pH 4 and 10 were lower than those obtained for the same process at pH 6.5. This was probably due to the charge-repulsion phenomenon, which is not favorable to OFL adsorption on Nano-GO/M.

3.2.1.4 Transformation Products of OFL Under Uv light

In this study we also investigated two different metabolites (POF: 9-piperazino ofloxacin and MOF: des-methyl ofloxacin) of OFL which are released during photocatalytic processes. In order to measure the metabolites of OFL (initial OFL conc. 100 mg/L), all experiments were realized after 60 min irradiation time, at room temperature and at original pH (6.5) of OFL solution with 0.5 g/L Nano-GO/M. Results showed that, after photocatalytic treatment from 100 mg/L OFL 82 mg/L OFL was photodegraded (Table 1). 18.11% of OFL was remained in the effluent without photodegradation. OFL was photodegraded to two metabolites (POF and MOF). From 100 mg/L OFL, 0.8211 mg/L POF and 2.2110 mg/L MOF were produced (Table 1). This showed that metabolites of OFL and almost 82 mg/L OFL was transformed into final products such as CO_2 and H_2O. Table 1. shows the percentage of removed or transformed products. Figure 14. shows the HPLC analysis of OFL and its metabolites under UV light at 60 min irradiation time and with 0.5 g/L Nano-GO/M.

	Influent (mg/L)	Effluent (mg/L)	Removed/Transformed (%)
OFL	100	18.110	82
POF (9-piperazinofloxacin)	0	0.8211	0.8211
MOF (des-methyl ofloxacin)	0	2.2110	2.2110

Table 1. shows the influent/effluent and removed/transformed OFL, POF (9-piperazino ofloxacin) and MOF (des-methyl ofloxacin) (operational conditions: 60 min, pH 6.5, 0.5 g/L Nano-GO/M, 21°C).

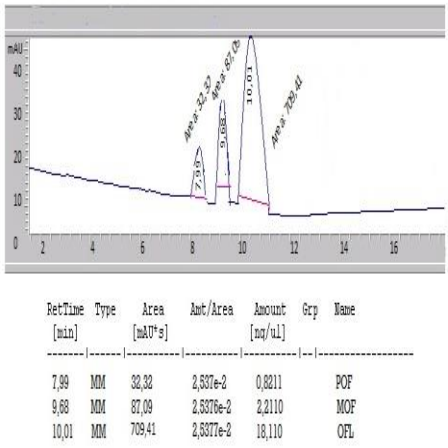

Figure 14. HLPC analysis of OFL (initial 100 mg/L) treatment with 300 W UV light at 60 min irradiation time and with 0.5 g/L Nano-GO/M

3.2.1.5 Kinetic Study of OFL Under UV light

3.2.1.5.1 Zero-Order Kinetics

The R^2 value for pseudo-zero-order reaction was found as 1 for OFL in the photocatalytic studies performed with Nano-GO/M (Figure 15). Pseudo-zero-order reaction's the zero order rate kinetic constant is k_0. The k_0 values evaluated from Pseudo-zero-order reaction plots were found as 0.078 min^{-1} for OFL from the Eq.(2).

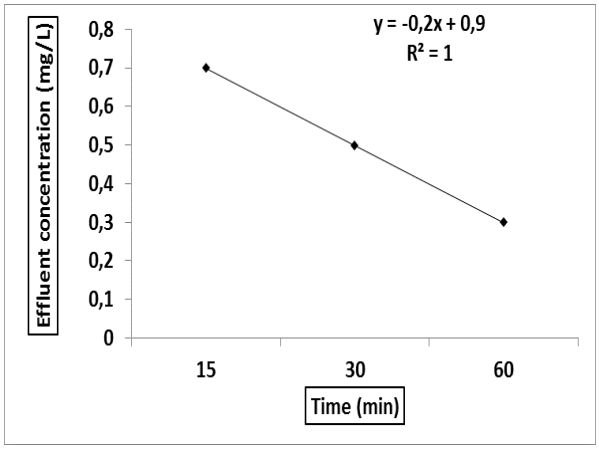

Figure 15. Pseudo-zero-order reaction of OFL (OFL: 5 mg/L, T: room temperature, irradiation time: 60 min., concentration of Nano-GO/M: 0.5 g/L, 300 watt UV light)

3.2.1.5.2 First-Order Kinetics

The R^2 value for first-order reaction was obtained as 0.986 for OFL in the photocatalytic studies performed with Nano-GO/M (Figure 16). First-order reaction's in the first order rate kinetic constant is k_1. The k_1 values evaluated from first-order reaction plots were found to be 0.0468 min^{-1} for OFL from the Eq.(3).

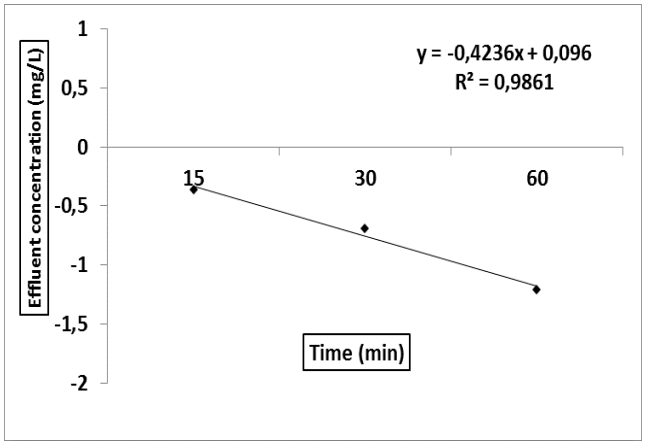

Figure 16. First-order reaction of OFL (OFL concentration: 5 mg/L, T: room temperature, irradiation time: 60 min, concentration of Nano-GO/M: 0.5 g/L, 300 watt UV light)

3.2.1.5.3 Second-Order Kinetics

The R^2 value for second-order reaction was found as 0.949 for OFL in the photocatalytic studies performed with Nano-GO/M (Figure

17). Second-order reaction's the second order rate kinetic constant is k_2. The k_2 values evaluated from second-order reaction plots were found as 0.052 min^{-1} for OFL from the Eq.(5).

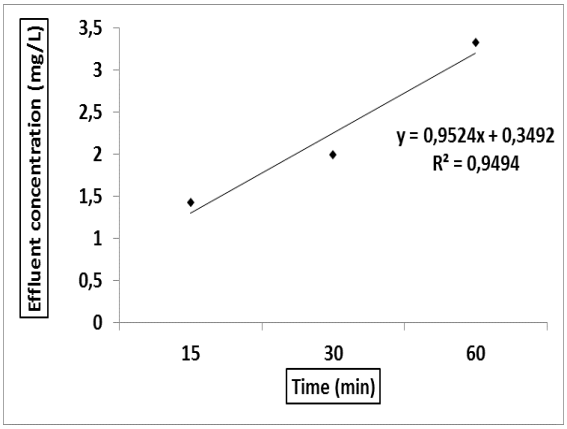

Figure 17. Second-order reaction of OFL (OFL concentration: 5 mg/L, T: room temperature, irradiation time: 60 min, concentration of Nano-GO/M: 0.5 g/L, 300 watt UV light)

As results of kinetic studies it was found that the OFL was photodegraded according to zero order reaction kinetic since the k_0 value calculated is meaningful than first order and second order reaction kinetics with highest R^2 value (1). From the zero order reaction plots k_0 value for OFL photodegradation was found to be 0.078 min^{-1}. In the other words, OFL was removed under 300 W UV irradiation according to zero order reaction kinetics.

3.2.2 Photodegradation of OFL Under Sunlight

3.2.2.1 Effects of Concentration of Nano-GO/M Composite on the Treatment of OFL Under Sunlight

Effects of 0.5 g/L, 2 g/L, 3.5 g/L, 5 g/L and 10 g/L Nano-GO/M composite concentrations on the removals of OFL with constant sunlight time (350 min was chosen due to preliminary studies results) at original pH of OFL solution (pH=6.5) under sunlight irradiation with a power of 80 W at outdoor temperature (35°C ± 5°C). The results were given in Figure 18. for 0.5, 2, 3.5, 5 and 10 g/L Nano-GO/M concentration at increasing OFL concentrations (1, 3, 5, 25, 100, 500 and 1000 mg/L). The removal efficiency is low at high OFL concentrations.Increased concentration of the OFL could occupy more active sites of Nano-GO/M, which inhibits generation of the oxidants [23].

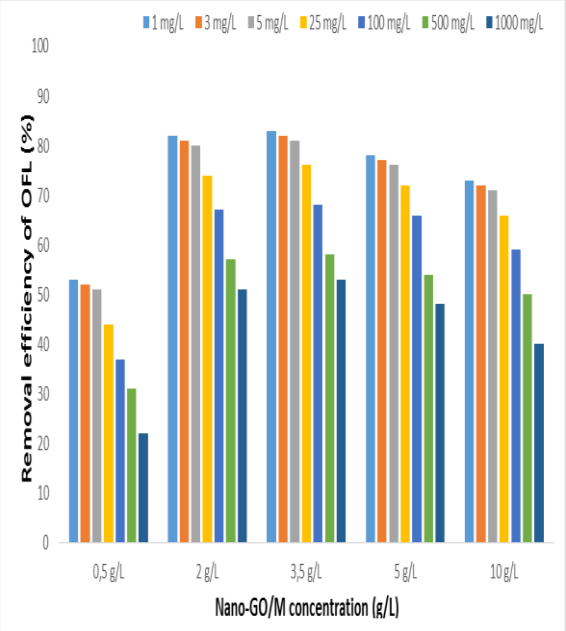

Figure 18. Effect of increasing OFL concentration on the yields of OFL removal efficiencies at a Nano-GO/M concentration of 0.5, 2, 3.5, 5 and 10 g/L at pH=6.5, at 35°C ± 5°C and 350 min irradiation time and with a power of 80 W sunlight

As the concentration of Nano-GO/M was increased from 0.5 g/L to 2 g/L and to 3.5 g/L the OFL removal efficiency increased from 53% to 82% and to 83% for initial OFL concentration of 1 mg/L (Figure 18.). Further increase in concentration of Nano-GO/M from 3.5 g/L to 5 g/L and to 10 g/L decreased the OFL removal yield slightly from 83% to 78% and to 73%, respectively, at the same operational conditions. The optimum Nano-GO/M concentration was chosen as 2 g/L in order to reduce the operational cost of photocatalytic treatment process. The effect of Nano-GO/M concentration on the degradation efficiency of OFL was investigated over the concentration range from 0.5 to 10 g/L. A significant increase is observed in the efficiency of degradation of OFL within the range of Nano-GO/M concentration from 0.5 to 3.5 g/L. The number of available adsorption and Nano-GO/M sites on the Nano-GO/M surface increases with increasing in Nano-GO/M concentration, resulting in the observed enhancement in degradation efficiency [19]. However, a further increase in Nano-GO/M

(from 3.5 to 10 g/L) concentration also reduces the specific activity of the catalyst because of agglomeration of catalyst particles and light scattering and screening effect, thus leading to the decreased photocatalytic degradation efficiency from 82% to 73% for 1 mg/L initial OFL concentration.

3.2.2.2 Effects of Irradiation time on the treatment of OFL under Sunlight

In order to determine optimum irradiation time for maximum OFL removal yields, increasing irradiation (30 min, 120 min, 250 min, 350 min and 24h) times were used (Figure 18). As aforementioned in the upper section, the optimum Nano-GO/M composite concentration was found as 2 g/L. Therefore, the effects of irradiation times of sunlight on the removal of OFL studied under same conditions (for constant OFL concentration 1 mg/L, at five different sunlight irradiation times (30 min, 120 min, 250 min, 350 min and 24h), at a pH of 6.5 and at constant 2 g/L Nano-GO/M composite concentration with a power of 80 W sunlight). As the irradiation time was increased from 30 min to 120 min to 250 min and to 350 min the OFL removals increased from 57% to 77% to 79% and to 82% for initial OFL concentration of 1 mg/L (Figure 19). Further increase in irradiation time from 350 min to 24 h did not affect the OFL removal yield significantly. OFL removal efficiency was increased only 3% (from 82% to 85%). The optimum sunlight irradiation time can be considered as 350 min for the maximum removal efficiency of OFL (82%- for 1 mg/L OFL).

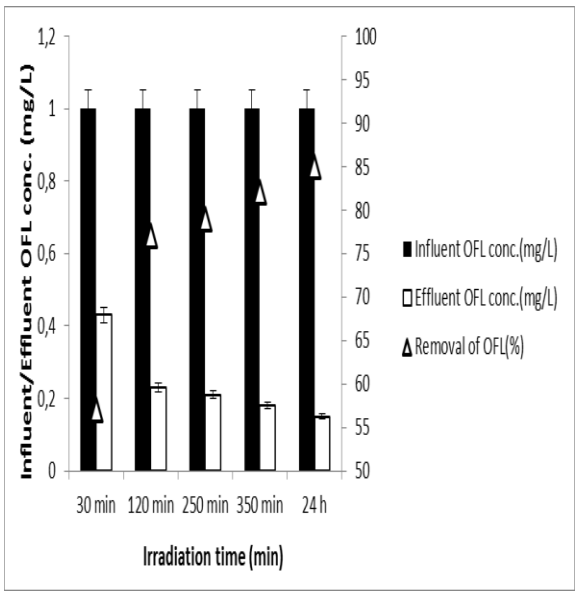

Figure 19. Effect of irradiation time on the yields of constant OFL concentration (5 mg/L), at a constant nano GO/M concentration (2g/L), at a pH of 6.5 and at 35°C ± 5°C and at increasing irradiation time and with a power of 80 W sunlight

3.2.2.3 Effects of pH on the of Removal OFL throughout Photodegradation Under Sunlight

The effects of pH on the on the increasing OFL concentrations (1, 3, 5, 25, 100 , 500 and 1000 mg/L) were studied under acidic, neutral and alkaline pHs (4, 6.5 and 10) at an irradiation time of 350 min, at a Nano-GO/M concentration of 2 g/L and at 35°C ± 5°C. In this study, the maximum removal efficiency was found as 82% at pH=6.5 at 1 mg/L OFL concentration and at 2 g/L Nano-GO/M concentration. As the pH values decreased from 6.5 to 4 the OFL removal yields decreased to 71% for 1mg/L OFL concentration and constant Nano-GO/M concentration (2 g/L). Under alkaline conditions photodegradation yields decrease to 53%. As the OFL concentrations were increased from 1 to 1000 mg/L the removal yields decreased significantly to 35%, 51% and 20% at pH 4, 6.5 and 10, respectively. The literature surveys showed that no data was found investigating the photo-removal of OFL under sunlight by Nano-GO/M, yet. Figure 20. summarizes the photocatalytic removal yields versus pH levels and OFL concentrations. Consequently, the maximum OFL (initial OFL concentration was 1 mg/L) photocatalytic removal yield (82%) was obtained at pH 6.5, but at alkaline and acidic pHs lowest OFL photocatalytic removal yields (71% and 53%, respectively) was obtained.

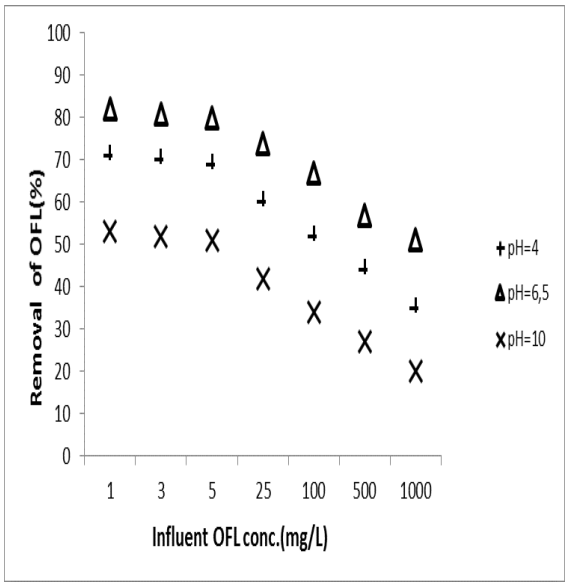

Figure 20. Effect of different pHs (4, 6.5 and 10) on the yield of OFL photocatalytic removal efficiency at a Nano-GO/M concentration of 2g/L, at 35°C ± 5°C and 350 min irradiation time and with a power of 80 W sunlight

3.3 Recovery of Nano-GO/M composite

One of the most fascinating characteristics of magnetic nanoparticles, showing advantage over other nanoparticles, is their magnetism [24]. Most water or wastewater treatment systems require a settling, filtration or centrifuge process to separate solids. However, magnetic nanoparticles can be separated and recovered with an external magnetic field due to the intrinsic magnetic characteristic of the nanoparticles, aiding in prominent nanoparticles recovery without a filtration process [24]. In photocatalytic processes catalyst cost is a very important issue. In this aspect, Nano-GO/M nanoparticles could be reused to solve this problem. A novel photocatalyst with ferromagnetic properties such as magnetite for recovery of Nano-GO/M and high effectiveness in the treatment of OFL was developed. Magnetic separation provides a very convenient approach for removing and recycling magnetic particles (such as magnetite) by applying external magnetic fields. In this study, six sequential treatment steps were investigated for determination of reusability of Nano-GO/M composite. Same 0.5 g/L Nano-GO/M composite were used for sequential six treatments of OFL without change the composite under same operational conditions {for OFL degradation-60 min) UV irradiation (300 Watt), for 1 mg/L OFL at original pH of solutions (6.5), at room temperature}. OFL removal efficiencies measured to determine the removal of OFL after six sequential with the same Nano-GO/M composite. In order to reuse Nano-GO/M composite after first treatment step, Nano-GO/M composite separated magnetically and then regenerated using ethanol (adjusted to pH 2.0 with 0.1 mol/ L HCl) as eluent [25]. After using ethanol Nano-GO/M composite dried under vacuum then the Nano-GO/M reused for second treatment process to treat 1 mg/L OFL again. For every new treatment step same procedure was applied to Nano-GO/M composite. From Figure 21, it can be clearly seen that the utilization of Nano-GO/M composite after first, second, third, fourth, fifth and sixth times, the removal efficiency of OFL decreased from 96% to 94%, to 90%, to 86%, to 79% and to 75%, respectively.

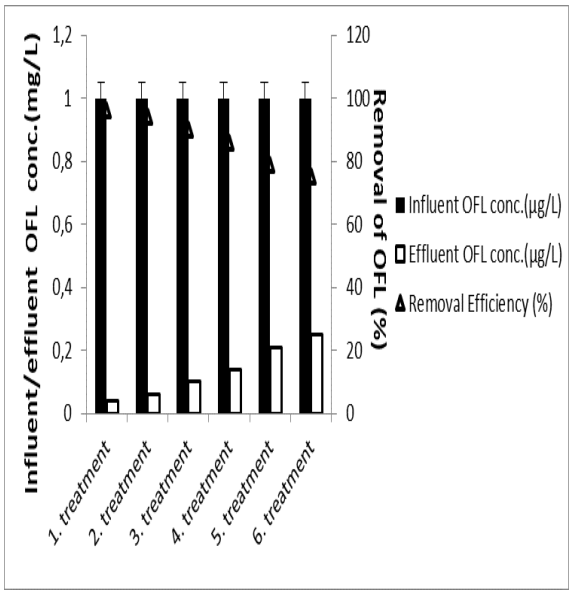

Figure 21. OFL measurement by recovery of Nano-GO/M composite (T: room temperature, Nano-GO/M composite concentration: 0.5 g/L, UV irradiation time: 60 min, UV power: 300 Watt, pH: 6.5 (original pH of OFL), initial concentration of OFL: 1 mg/L).

Conclusions:

For maximum OFL removal (96%) the optimum Nano-GO/M concentration was found to be 0.5 g/L at 1 mg/L initial OFL concentration, at pH of 6.5, at a UV power of 300 W and at a temperature of 21°C after 60 minutes irradiation time throughout photocatalytic degradation under UV light. The minimum OFL removal

was found to be 65% at 1000 mg/L OFL at the optimum Nano-GO/M concentration (0.5 g/L) at a pH of 6.5, at a UV power of 300 W and at a temperature of 21°C after 60 minutes irradiation time by photooxidation. OFL photodegraded according to the zero-order reaction kinetic model. The maximum photooxidation yield under sunlight was found to be 82% for 1 mg/L OFL at a Nano-GO/M concentration of 2 g/L at a pH of 6.5 and at a temperature of 35°C ± 5°C after 350 minutes retention time. It can be concluded that the Nano-GO/M can be produced succesfully under laboratory conditions. Also Nano-GO/M could be reused at least six treatment step without any significant lost.

Acknowlegment:

The Authors Would Like To Express Appreciation For The Support Of The Sponsors Dokuz Eylul University Scientific Research Project (KB.FEN.020), TUBITAK 2210-C National Grant For Master Thesis Relevant To Priority Subjects and Pamukkale University Scientific Research Project (2016KRM004).

References:

1. D. Fatta-Kassinos, S. Meric, A. Nikolaou, Pharmaceutical residues in environmental waters and wastewater: current state of knowledge and future research, *Analytical and Bioanalytical Chemistry* ***399*** (2011) 251-275
2. K. Kümmerer, Antibiotics in the aquatic environment–a review–part I, *Chemosphere* ***75*** (2009) 417–434
3. E. Hapeshi, A. Achilleos, M.I. Vasquez et al.,, Drugs degrading photocatalytically: Kinetics and mechanisms of ofloxacin and atenolol removal on titania suspensions, *Water Research* ***44*** (2010) 1737–1746.
4. S. Castiglioni, F. Pomati, K. Miller, et al., Novel homologs of the multiple resistance regulator marA in antibiotic-contaminated environments, *Water Research* ***42*** (2008) 4271–80.
5. I. Michael, E. Hapeshi, J. Aceña, et al., Light-induced catalytic transformation of ofloxacin by solar Fenton in various water matrices at a pilot plant: Mineralization and characterization of major intermediate products, *Science of the Total Environment* ***461–462*** (2013) 39–48
6. L. Zivanovic, G. Zigic, M. Zecevic, Investigation of chromatographic conditions for the separation of ofloxacin and its degradation products, *Journal of Chromatography A* ***1119*** (2006) 224–230
7. E. Hapeshi, F. Fotiou, D. Fatta-Kassinos, Sonophotocatalytic treatment of ofloxacin in secondary treated effluent and elucidation of its transformation products, *Chemical Engineering Journal* ***224*** (2013) 96–105
8. M. Crespo-Alonso, V.M. Nurchi, R. Biesuz, et al., Biomass against emerging pollution in wastewater: Ability of cork for the removal of ofloxacin from aqueous solutions at different pH, *Journal of Environmental Chemical Engineering* ***1*** (2013) 1199–1204
9. A.H. Castro Neto, F. Guinea, N.M.R Peres et al., The electronic properties of graphene, *Reviews of Modern Physics* ***81*** (2009) 109–162
10. Q.J. Xiang, J.G. Yu, M. Jaroniec, Graphene-based semiconductor photocatalysts, *Chemical Society Reviews* ***41*** (2011) 782–796.
11. S. Zhong, J. Wei, H. Mei, et al., Graphene supported silver@silver chloride & ferroferric oxide hybrid, a magnetically separable photocatalyst with high performance under visible light irradiation, *Applied Surface Science* ***347*** (2015) 242–249
12. L. Ai, Z. Chunying, C. Zhonglan, Removal of methylene blue from aqueous solution by a solvothermal-synthesized graphene/magnetite composite, *Journal of Hazardous Materials* ***192*** (2011) 1515–1524.
13. W. Hummers, R. Offeman, Preparation of graphitic oxide. *Journal of American Chemical Society* ***80 (6)*** (1958) 1339–1339
14. Y. Nengsheng, X. Yali, S. Pengzhi et al., Synthesis of magnetite/graphene oxide/chitosan composite and its application for protein adsorption, *Materials Science and Engineering* **45** (1958) 8–14

15. https://en.wikipedia.org/wiki/Rate_equation

16. Q. Huamin, L. Chuannan, S. Min, L. Fuguang, et al., A chemiluminescence sensor for determination of epinephrine using graphene oxide–magnetite-molecularly imprinted polymers, *Carbon* ***50*** (2012) 4052–4060

17. Y. Tang, H. Guo, L. Xiao et al., Synthesis of reduced graphene oxide/magnetite composites and ınvestigation of their adsorption performance of fluoroquinolone antibiotics, *Colloids And Surfaces A: Physicochemical And Engineering Aspects* ***424*** (2013) 74–80

18. M. Pelaez, N. Nolan, S. Pillai et al., A review on the visible light active titanium dioxide photocatalysts for environmental applications, *Applied catalysis b: Environmental* ***25*** (2012) 331–349

19. L. Zhe-Qi, W. Hui-Long, Z. Long-Yun, Preparation and photocatalytic performance of magnetic TiO_2–Fe_3O_4/Graphene (RGO) composites under vıs-light irradiation, *Ceramics International* ***41*** (2015) 10634–10643

20. M. Barjasteh-Moghaddam, A. Habibi-Yangjeh, Effect of Operational Parameters on Photodegradation of Methylene Blue on ZnS Nanoparticles Prepared in Presence of an Ionic Liquid as a Highly Efficient Photocatalyst, *Journal of the Iranian Chemical Sociecty* ***8*** (2010) 169-175

21. G. Liu, N. Wang, J. Zhou, A. Wang et al., Microbial preparation of magnetite/reduced graphene oxide nanocomposites for the removal of organic dyes from aqueous solutions, *RSC Advances* ***5*** (2015) 95857-95865

22. M.S. Peres, M.G. Maniero, J.R. Guimarães, Photocatalytic degradation of ofloxacin and evaluation of the residual antimicrobial activity, *Photochemical Photobiological Sciences 3 (2015)* 556-62

23. L. Yan, L. Yu, M. Ray, Degradation of paracetamol in aqueous solutions by TiO_2 photocatalysis, *Water Research* ***42*** (2008) 3480–3488

24. S. Tang, I. Lo, Magnetic nanoparticles: essential factors for sustainable environmental applications, *Water Research* ***47*** (2013) 2613 -2632

25. S. Chowdhury, R. Balasubramanian, Recent advances in the use of graphene-family nanoadsorbents for removal of toxic pollutants from wastewater, *Advances in Colloid and Interface Science* ***204*** *(2014)* 35–56

Synthesis and Characterization of Superparamagnetic Magnetite/Modified Magnetite Nano-Particles (Fe3O4@SiO2@L)

Hakan Çiftçi1, Bahri Ersoy1,a and Atilla Evcin2

1Afyon Kocatepe University, Engineering Faculty, Department of Mining Engineering, Afyonkarahisar, Turkey
2Afyon Kocatepe University, Engineering Faculty, Department of Material Science and Engineering, Afyonkarahisar, Turkey

Abstract:

In this study, magnetite nano-particles (MNPs) were synthesized by chemical co-precipitation method at first, and then MNPs were coated with silica by modified Stöber process and the surface of silica coated MNPs were functionalized by 3-aminopropyl-triethoxysilane (APTES). Finally, the prepared NPs were characterized by Fourier transform infrared spectroscopy (FT-IR), transmission electron microscopy (TEM), vibrating sample magnetometer (VSM) and Zetasizer devices/methods. Mean size of NPs was about 15 nm according to TEM photographs and the saturation magnetization values of Fe3O4 and Fe3O4@SiO2@L NPs were measured as 75 emug-1 and 37 emug-1, respectively. **Keywords**: protein folding, nanoporous sol-gel glasses, silica-based biomaterials, circular dichroism spectroscopy, surface hydration, crowding effects, micropatterning, biomedical applications.

Introduction:

Magnetite nano-particles (MNPs) have recently attracted considerable attention in analytical chemistry, medicine and adsorption processes because of their some properties which of high surface area, low cost and high magnetic sensitivity. However, pure MNPs are not stable at different ambient conditions that can be oxidized, easily soluble in acidic media and may be agglomerated [1, 3]. To overcome these obstacles, silica is the best material to coat the surface of MNPs as a shell. In this way MNPs can remain stable, do not oxidize and their surface becomes much more functional [2]. The surface of silica coated magnetite (Fe3O4@SiO2) is negatively charged in aqueous media even at low pH values. Fe3O4@SiO2 NPs can be modified by some functional amine groups (for example, APTES) and thus, positively charged surface will have been obtained for specific purposes.

Materials and Methods:

Materials: Iron(III) chloride, Iron (II) chloride, absolute ethanol, tetraethylorthosilicate (TEOS) (>98%), NH_4OH (28%) and APTES (>98%) were purchased from Merck.

Synthesis of the NPs: Chemical co-precipitation technique of Fe(II) and Fe(III) ions in alkaline medium was used to prepare Fe_3O_4 NPs [4]. In summary, $FeCl_2.4H_2O$ (0.01 mol) and $FeCl_3.6H_2O$ (0.02 mol) were dissolved in a five-neck flask with 100 mL of deionized water and then 50 mL of NH_4OH (28 wt%) was added into the solution slowly (3.33 mL/min) with mechanical stirring (750 rpm) at 30 ^oC. The last mixture was then heated 90 ^oC and stirred for 2 h. The resulting Fe_3O_4 precipitates were separated from mixture by a magnet and washed with deionized water and ethanol. $Fe_3O_4@SiO_2$ NPs were prepared based on modified Stöber method [6]. Accordingly, MNPs (0.5 g) were re-dispersed in a three-neck flask which contains 40 ml of deionized water, 160 ml of ethanol and 5 ml of NH_4OH. After 30 min stirring (750 rpm) at 30 ^oC, 0.4 ml of TEOS was added drop wise and the mixture was further stirred for 4 h. The resulting $Fe_3O_4@SiO_2$ NPs were collected by magnetic separation and washed with deionized water and ethanol. To obtain $Fe_3O_4@SiO_2@L$ NPs, 150 mg of $Fe_3O_4@SiO_2$ was added in a beaker with 50 ml of ethanol and dispersed ultrasonically for 5 min. Then, 1 ml APTES was added into the mixture and stirred at 50 ^oC for 3 h. Finally, attained $Fe_3O_4@SiO_2@L$ NPs were dried at 65 ^oC for 4 h. All synthesis processes were performed under nitrogen gas to prevent oxidization of NPs. Fig. 1 illustrates summarized schematic diagram of synthesis processes.

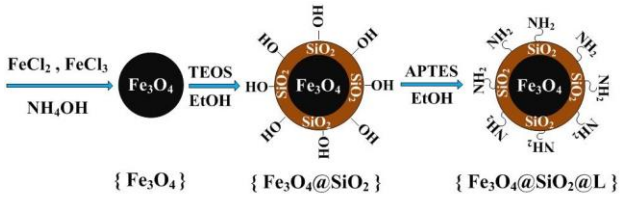

Figure 1. Illustration of synthesis process of NPs.

Characterization techniques: Morphology and size of NPs were observed using JEM 2100F (JEOL) TEM. To determine the functional groups of NPs, FT-IR spectra were recorded using a Perkin–Elmer Spectrum BX spectrometer. Zeta potential measurements were done using Malvern Nano-Z zetasizer. 1.2H VSM (LDJ 9600) was used to identify magnetic properties of NPs.

Results and discussion

Fig. 2 shows the TEM images of NPs. The shape of NPs is nearly spherical and average size of NPs is about 15 nm. Additionaly, silica coating and amine modification have no significant effect on the size and morphology of Fe_3O_4 NPs.

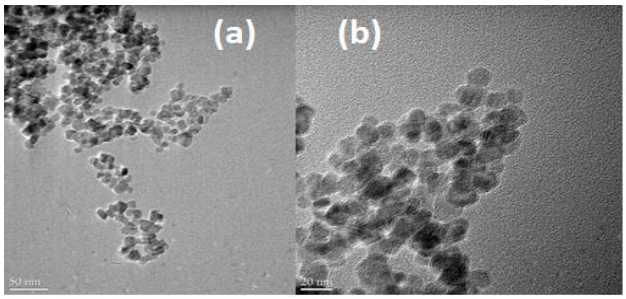

Figure 2. TEM images of Fe_3O_4(a), Fe_3O_4@SiO_2@L(b) NPs.

The IR spectrum of NPs (Fig. 3a) shows a strong absorption band at 575 cm^{-1} which is attributed to the Fe–O vibration frequency of magnetite [3]. The bands around 945 cm^{-1} and 1094 cm^{-1} (Fig. 3b) indicate the Si–O–Si and Si–O–H stretching vibrations [5]. The peaks at around 800 cm^{-1} show Si–O vibration. The broad band around 3450 cm^{-1} is a result of O-H stretching vibrations [3].

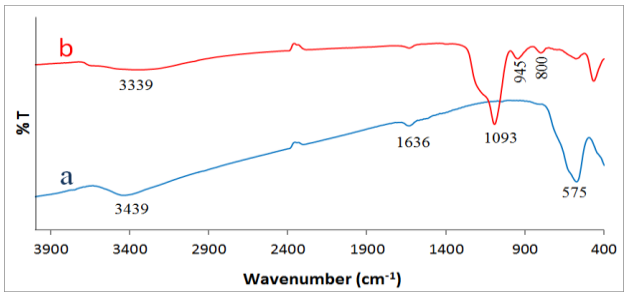

Figure 3. FT-IR spectrum of Fe_3O_4 (a), Fe_3O_4@SiO_2 (b) NPs.

Zeta potential measurements of NPs are presented in the Fig. 4. The iso-electric points of Fe_3O_4, Fe_3O_4@SiO_2 and Fe_3O_4@SiO_2@L NPs were measured as 6.8, 2.2 and 8.4, respectively. While the surface of Fe_3O_4@SiO_2 NPs is more negative, Fe_3O_4@SiO_2@L NPs are more positively charged when compared to the pure magnetite NPs at the same pH values. This result proves that, silica coating and amine modification processes of Fe_3O_4 NPs were successfully done.

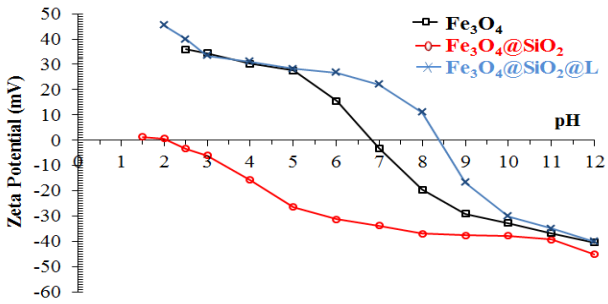

Figure 4. Zeta potential curves of NPs as a function of pH.

Vibrating sample magnetometer (VSM) was used to determine the magnetic properties of the NPs. Fig. 5 shows the hysteresis loops of NPs and both magnetization curves go through exactly the origin of magnetization graph. Accordingly, NPs did not exhibit hysteresis, coercivity and remanence. This is a result of superparamagnetic property of NPs [7]. The saturation magnetization values of Fe_3O_4, and Fe_3O_4@SiO_2@L NPs were measured as 75 $emug^{-1}$ and 37 $emug^{-1}$, respectively. Even so, 37 $emug^{-1}$ is also sufficient to separate Fe_3O_4@SiO_2@L NPs by a magnet from a suspension.

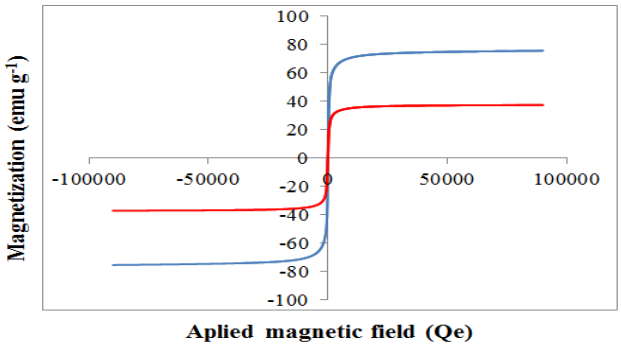

Figure 5. Magnetization curves of Fe_3O_4(a), Fe_3O_4@SiO_2@L (b) NPs.

4. Conclusions

In this study, the obtained results can be summarized as following: (i) mean size of synthesized NPs was about 15 nm; (ii) FT-IR, VSM, TEM and Zeta Potential analysis proved that the MNPs have been successfully coated with silica in the core-shell form, and modified by APTES; (iii) The superparamagnetic property of NPs was confirmed by VSM.

Acknowledgments

This study was financially supported by Afyon Kocatepe University, Scientific Research Projects (BAP), Project No: 16.KARİYER.15.

References

1. H. Bagheri, A. Afkhami, M. Saber-Tehrani, H. Khoshsafar, Talanta, **97**, 87 (2012)
2. Y.H. Deng, C.C. Wang, J.H. Hu, W.L. Yang, S.K. Fu, Coll. and Surf. A: Physicochem. Eng. Aspects. **262**, 87 (2005)
3. M.H. Farimani, N. Shahtahmasebi, M. RezaeeRoknabadi, N. Ghows, A. Kazemi, Physica E, **53**, 207 (2013)
4. R. Massart, IEEE Transactions on Magnetics., **17(2)**, 1247 (1981)
5. S. Sadeghi, H. Azhdari, H. Arabi, A.Z. Moghaddam, Journal of Hazardous Materials, **215-216**, 208 (2012)
6. W. Stöber, A. Fink, E. Bohn, Journal of Colloid and Interface Science., **26-1**, 62 (1968)
7. X. Zhao, Y. Shi, T. Wang, Y. Cai, G. Jiang, Journal of Chromatography A, **1188**, 140 (2008)
1. 71-491.

Effect of Post-Exfoliation Annealing and Ultrasonic Treatments on Mechanically Exfoliated MoS_2

P. Budania,* N. Mitchell, D. McNeill
School of Electronics, Electrical Engineering and Computer Science, Queen's University, Belfast, UK

Abstract:
Post-exfoliation thermal annealing in air and ultrasonic treatments were carried out on mechanically exfoliated MoS_2 flakes on oxidised silicon substrates. Ultra-sonication of MoS_2 flakes on SiO_2 without prior annealing results in almost complete removal of flakes. Thermal annealing at 270 ℃ prior to ultrasonic treatment significantly increases the interface adhesion. Annealing at 75 ℃ to 175 ℃ followed by ultrasonic treatment results in small residual MoS_2 fragments on the samples. Increase in annealing temperature to 460 ℃ results in decomposition of MoS_2.

Keywords: mechanical exfoliation, MoS_2, post-exfoliation, thermal annealing, ultrasonic cleaning, interface adhesion.

Introduction
Among various preparation methods for transition metal dichalcogenides (TMDs), mechanical exfoliation remains the most efficient way to transfer high quality 2D TMD material onto a substrate. The pristine quality of 2D semiconductors is preserved by mechanical exfoliation. Therefore, MoS_2 field effect transistors (FET) fabricated by mechanical exfoliation have resulted in much higher performance devices (Radisavljevic *et al.*, 2011) in comparison to films synthesized by other methods (Zhan *et al.*, 2012). The main drawbacks of mechanical exfoliation are small flake area and low throughput of ultra-thin 2D TMD material. Here a study is presented on post-exfoliation thermal annealing in air and ultrasonic treatments performed on mechanically exfoliated MoS_2 flakes on oxidised silicon substrates. These post-exfoliation tratements aimed to increase the density of large area ultra-thin mechanically exfoliated flakes. Post-exfoliation treatments on mechanically exfoliated graphene have been previously reported to enable formation of large area single-layer nanosheets of graphene (Pang *et al.*, 2010).

Experimental details
Samples were prepared by Scotch® tape assisted mechanical exfoliation of MoS_2 onto a solvent cleaned oxidized silicon (290 nm) substrate. Optical microscopy and tapping mode atomic force microscopy (AFM) were used to determine the thickness of flakes. Table 1 gives details of four different post-exfoliation experiments. Optical microscope imaging of each sample was done before and after post-exfoliation treatment to observe any modification in colour or position of MoS_2 flakes on the samples.

Expt.	Thermal annealing	Ultrasonic tretament
I	none	5 minutes
II	460 °C for 2 hours	none
III	270 °C for 2 hours	10 minutes
IV	75 °C - 150 °C for 1 and half hours	10 minutes

Table 1: Details of different post-exfoliation annealing and ultrasonic treatments performed on mechanically exfoliated MoS_2 samples.

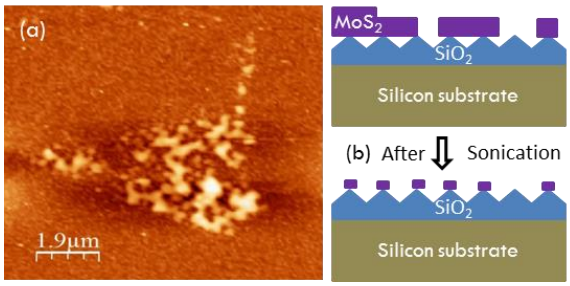

Figure 1: (a) AFM image of region where a MoS_2 flake has come off the substrate leaving non-continuous fragments of MoS_2. (b) representation of a thick MoS_2 flake on oxide substrate.

Results and discussion
Ultra-sonication of MoS_2 flakes on SiO_2 without prior annealing resulted in almost complete removal of flakes, indicating weak bonding at the MoS_2/SiO_2 interface. AFM scan of Figure 1(a) shows very small bits of MoS_2 have remained adhered to the substrate after ultrasonic treatment. The adhesion of a thick MoS_2 flake to the oxide substrate is illustrated in Figure 1(b). Adhesion is believed to be reduced due to low contact area. Therefore, ultrasonic treatment without prior annealing of the sample results in removal of all top layers of the flake but sometimes a few bottom layers remain adhered to the substrate only at places where it was in contact prior to sonication. This results in non-uniform and discontinuous fragments on the substrate. For experiment II, MoS_2 samples were annealed above its oxidation temperature at 460 ℃. This lead to decomposition of MoS_2. For experiment III, annealing temperature was further reduced to 270 ℃. Annealing was followed by ultrasonic treatment of the samples. It was found that contrary to previous post-exfoliation ultrasonication treatment, the interface adhesion between MoS_2 and underlying oxide significantly increases and prevents removal of MoS_2 flakes. We consider that the improved adhesion is due to effusion of water vapour

and other impurities from the interface resulting in greater contact area. However, the treatment did not result in thinning of MoS_2 flakes, so the annealing temperature was further reduced.

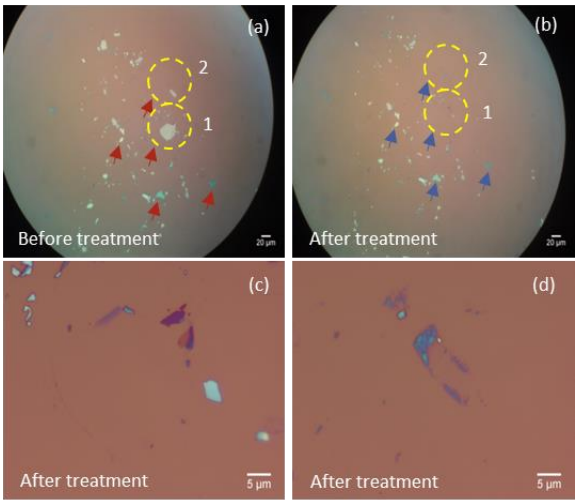

Figure 2: (a) and (b) optical microscope images of the same region on a sample taken before and after annealing of MoS_2 flakes at 125 ℃ followed by ultrasonic treatment. Arrows are used for identification of the same region. Flakes within circle 1 and 2 in 2(b) have left behind thin residual flakes as observed in 2(c) and 2(d).

For experiment IV, samples were annealed in the range of 75 ℃ to 175 ℃ followed by ultrasonic treatment. This resulted in small residual MoS_2 fragments due to breakage and/or partial removal of overlying MoS_2 flakes. Figure 2(a) and (b) are optical microscope images of the same region of a sample taken before and after the treatment respectively. The flakes encircled in Figure 2(a) have been removed after the treatment, as observed in Figure 2(b). Figure 2(c) and 2(d) corresponds to encircled regions 1 and 2 in Figure 2(b) respectively. In a few instances top layers of MoS_2 flakes have been removed from the sample and underlying layers have been exposed. In some instances MoS_2 flakes have been completely removed from the sample leaving behind non-uniform residual layers.

Contrary to post-exfoliation experiments on graphene, we observed that whilst the adhesion of MoS_2 is considerably enhanced upon annealing, no single-layer MoS_2 flakes resulted. Although the two materials have very similar interlayer van der Waals interaction, the corrugation upon annealing on oxide substrates is not identical. We believe that the dissimilarity in corrugation is due to structural difference in the materials. Interplanar interaction between out-of-plane Mo and S atoms gives MoS_2 a higher bending rigidity (Jiang *et al.*, 2013) in comparison to graphene which is a single layer of carbon atoms.

Conclusion

Post-exfoliation thermal annealing in air and ultasonic treatments were performed on mechanically exfoliated MoS_2 on oxide substrates. It did not yield large area thin two dimensional flakes due to high rigidity of MoS_2. However, the adhesion of MoS_2 flakes to the oxide subsatrte was controlled by annealing temperature.

References:

Radisavljevic, B., Radenovic, A., Brivio, J., Giacometti, V., and Kis, A. (2011), Single-layer MoS_2 transistors, *Nat. Nanotechnol.*, 6, 147-150.

Zhan, Y., Liu, Z., Najmaei, S., Ajayan, P. M., and Lou, J. (2012), Large-Area Vapor-Phase Growth and Characterization of MoS_2 Atomic Layers on a SiO_2 Substrate, *Small*, 8, 966–971.

Pang, S., Englert , J. M., Tsao, H. N., Hernandez , Y., Hirsch, A., Feng, X., Müllen, K. (2010), Extrinsic Corrugation-Assisted Mechanical Exfoliation of Monolayer Graphene, *Adv. Mater.*, 10, 5374-5377.

Jiang, J,-W., Qi, Z., Park, H. S., Rabczuk T. (2013), Elastic bending modulus of single-layer molybdenum disulfide (MoS_2): finite thickness effect, *Nanotechnology*, 24, 435705.

Plasma-assisted CVD graphene synthesis and characterisation on nickel substrates

P. Pop-Ghe,* L. Krückemeier, N. Wöhrl and V. Buck

University of Duisburg-Essen, Faculty of Physics and CENIDE, Duisburg, Germany

By now, the most reliable approach for the synthesis of graphene is the Chemical Vapour Deposition (CVD) on copper. This is due to the catalysing effects of copper that are often exploited. This process has to be conducted at high temperatures close to the melting point of copper, which restricts the achievable quality. Therefore the application of nickel is suggested, as it exhibits a higher melting point as copper, but still offers the advantages of commercial availability and catalysing effects. In addition, the process temperature can be reduced by the application of a plasma, as it allows for the partial decomposition of species before reaching the substrate. Hereby, the use of nickel as a substrate material includes special circumstances, because of efficient methane adsorption [1][2] and decomposition on nickel [2][3] and the high diffusion coefficient and solubility of carbon in nickel respectively [4][5]. For hydrogen desorption is favoured instead of adsorption on or diffusion into nickel respectively[2][3][6][7], although a possible etching effect has to be considered within a plasma. It is common knowledge in literature that the transfer will worsen the graphene qualities due the introduction of contaminations, defects or atmospheric influence. Before transfer, the presented sample inherited average graphene signals and comparable high defect densities. After the transfer onto a Si/SiO_2 substrate a significant improvement occurs. High-quality graphene areas of high extensions (40 x 40 µm²) and 2D/G ratios up to 7.4 can be found frequently, while defect densities and FWHM are low ($(D/G)_{average} \sim 0.3$, FWHM = 32 cm^{-1}). To give evidence to this, Raman mapping was performed. The reason for this improvement can be assumed within the strong mutual interaction that is proposed for the nickel-graphene system [8], not in an actual quality improvement of the graphene by the transfer. The strong bonding evolving between graphene and nickel distorts the graphene Raman spectrum by altering the graphene phonon dispersion [8] and thus a reasonable comparison to other works is prohibited. Concerning synthesis, the dominant mechanisms on layer growth are solubility and diffusion. Since both are strongly temperature dependent, values for diffusion and solubility have been approximated from literature [4][5]. Following this, solubility and diffusion are negligible at low temperatures, thus amorphous growth is assumed to occur in this temperature regime. The experimental results presented confirm this expectation, low temperatures lead to the growth of carbon black [9] throughout the sample. The medium temperature resembles a transition regime, which leads to the crystalline growth domain at highest temperatures used. Here, solely crystalline layer modifications as graphene, multilayers and graphite grow on the sample. At low temperatures the dominating factor is the plasma activity, so synthesis will result to a thick coverage by amorphous carbon. At high temperatures, the high diffusion coefficient and solubility remove the excessive carbon from the surface, so that the equilibrium between surface and plasma is shifted towards a rather empty surface. Consequently, layer formation starts when the plasma is turned off and the sample begins to cool down. Concerning layer formation, two dominant mechanisms are present: First, there will be lateral growth out of the grain boundaries as quick out-diffusion facilitates nucleation. Secondly, there must be diffusion out of the grains, too, because bulk defects and preferred crystal orientations have to be assumed. Which mechanisms dominates here is significantly determined by the cooling rate [10]. At process times of up to 30 minutes, the previous assumptions have to be adjusted, as the diffusion length increases up to the entire substrate thickness. This includes the possibility that carbon diffuses along the whole axial distance, thus an additional equilibrium has to be assumed that evolves within the substrate and causes a correlation between front and back side graphene growth. Although the back side is not in direct contact to the plasma, it can be assumed that species will be able to reach the back surface. Still, the transport to the back side underlies spatial restrictions, which cause a spatial dependence of graphene growth. On the basis of the characteristics obtained, it can be verified

that graphene could be synthesised on the back surface as well, but the optical observation shows that this result is not representative. The lateral growth causes a thick coverage with graphite at the edges, thinning into direction of the centre. Apart from that, the back side temperature variation shows the same development as the front side within the given restrictions. The Raman mapping shows that continuous graphene areas of low defect density have been synthesised ($(2D/G)_{max}$ = 5.4, $(D/G)_{average}$ ~ 0.5). The additional examination of a grain boundary reveals that the assumptions on preferred crystal orientations are valid, the different grains exhibit the growth of distinct modifications each. From the distribution of defects it is indicated, that the graphene segregation has a strong reconstructional character. At grain boundaries, where defects accumulate, the reconstruction is intense and thus the defect density is high. Furthermore all crystalline layer modifications of carbon are always present on the sample due to the statistical distribution of grain orientations. To give further evidence to this suggestion, a nickel single crystal was applied as a substrate. The Ni(111) orientation exhibits the best crystal lattice match (lattice mismatch 1.6%) with regard to graphene among the available nickel orientations. Its usage as a substrate material leads to graphene growth solely throughout the substrate, although it is worth mentioning that island growth is preferred. In respect of the synthesis, the parameters demonstrated feature high temperatures, low methane supply and long synthesis times. The transferred graphene exhibits a higher quality than could be concluded from the analysis on the nickel substrate and the defect-density proves to be throughout low or below resolution. Considering the development of the 2D-band morphology, the result points at a strong graphene-nickel binding as well. In particular a developing asymmetry in the 2D-band can be suggested to correlate to the lifting of the degeneracy of the ZO (out-of-plane optical) and ZA (out-of-plane acoustical) phonon branches [8]. The results allow for the conclusion, that the PACVD approach has an extensive potential towards graphene synthesis and still offers various possibilities on improvements. Stable, distinct temperatures as well as time control at high H_2/CH_4 ratios turn out to be a reliable way to synthesise graphene on polycrystalline nickel foils (within the restrictions given by the substrate). However, the remaining process parameters such as cooling and annealing time, pressure (independent from temperature), variation of substrate thickness and application of larger-scale or distant plasmas have to be considered, too, if the process shall be fully optimised. It could be shown that the substrate structure determines the preferred growing carbon modification and moreover, that the substrate influence is not only crucial to the synthesis, but to subsequent analysis as well as the graphene-nickel system exhibits a strong bonding, which causes a distortion of the measurement results.

References:

[1]W. An, X. C. Zeng und C. H. Turner (2009), First-principles study of methane dehydrogenation on a bimetallic Cu/Ni(111) surface, *Digital Commons University of Nebraska-Lincoln*, 1.

[2]M. Losurdo, M. M. Giangregorio, P. Capezzuto und G. Bruno (2011), Graphene CVD growth on copper and nickel: role of hydrogen in kinetics and structure, *Physical Chemistry Chemical Physics*, 13, 20836.

[3]G. Henkelmann, A. Arnaldsson und H. Jónsson (2006), Theoretical calculations of CH_4 and H_2 associative desorption from Ni(111): Could subsurface hydrogen play an important role?, *Journal of Chemical Physics*, 124.

[4]K. Natesan und T. Kassner (1973), Thermodynamics of carbon in nickel, iron-nickel and iron-chromium-nickel alloys, *Metallurgical Transactions*, 4, 2557.

[5]J. Lander, H. Kern und A. Beach (1952), Solubility and Diffusion Coefficient of Carbon in Nickel: Reaction Rates of Nickel-Carbon Alloys with Barium Oxide, *Journal of Applied Physics*, 23, 1305.

[6]R. Baer, Y. Zeiri und R. Koslo (1997), Hydrogen transport in nickel (111), *Physical Review B*, 55, 10952.

[7]R. B. McLellan und P. L. Sutter (1984), Thermodynamics of the Hydrogen-Nickel System, *Acta Metallurgica*, 32, 2233.

[8]A. Dahal and M. Batzill (2014), Graphene-nickel interfaces: A review, *Nanoscale*, 6, 2458.

[9] T. Jawhari, A. Roid, and J. Casado (1995), Raman Spectroscopic Characterization of Some Commercially Available Carbon Black Materials, *Carbon*, 33, 1561–65.

[10]Q. Yu, J. Lian, S. Siriponglert, H. Li, Y. P. Chen und S.-S. Pei (2008), Graphene segregated on Ni surfaces and transferred to insulators, *Applied Physics Letters*, 93, 113103.

Few-Layer Graphene Langmuir Nanofilm Decorated by Palladium Nanoparticles for NO_2 and H_2 Gas Sensing

D. Kostiuk[1*], S. Luby[1], M. Demydenko[1], Y. Halahovets[1], P. Siffalovic[1], K. Vegso[1], J. Ivanco[1], M. Jergel[1], M. Kotlar[2], R. Redhammer[2], E. Majkova[1]
[1]Institute of Physics, Slovak Academy of Sciences, Bratislava, Slovakia
[2]Slovak University of Technology, Bratislava, Slovakia

Abstract:
Graphene nanofilms were deposited onto oxidized Si by modified Langmuir-Schaefer technique with the submerged substrate from the solution of few-layer graphene (FLG) in 1-methyl-2-pyrrolidone. Films were characterized by SEM, AFM, HRTEM, XRD and Raman spectroscopy. Average FLG flake thickness and lateral dimension are 5 and 300 nm, respectively. Films were decorated by Pd nanoparticles (6 – 7 nm) using drop casting and centrifugation. Gas sensing was tested in the mixtures of dry air with 10 – 10 000 ppm of H_2 and 2 – 200 ppm of NO_2. The sensor response at room temperature (RT) was 4 % at 10 ppm and 13.5 % at 1000 ppm of H_2. For NO_2 gas the response of 10% at 6ppm at RT was observed. The Pd decoration doubled the response to NO_2 gas. The fabrication metod is simple, low cost and scalable.

Introduction:
The high surface-to-volume ratio of graphene stimulated its application in advanced chemical gas sensors. It was demonstrated that their sensitivity could be enhanced with graphene decorated by metallic nanoparticles, e.g. Pd or Pt [1]. In this work we present the NO_2 and H_2 gas sensing properties of the few-layer graphene (FLG) Langmuir nanofilm decorated by Pd nanoparticles.

Materials and Methods:
A solution of FLG in 1-methyl-2-pyrrolidone was obtained by a 1 hour mild sonication of the expanded milled graphite (SGL-Carbon) followed by 30 min centrifugation at 10^4 g. The few-layered nature of nanosheets was confirmed by HRTEM. Prepared solution of FLG nanosheets was deposited onto SiO_2 (500 nm)/Si substrates by a modified Langmuir-Schaefer technique allowing uniform coverage of large area substrates [2]. The FLG films were characterized by AFM, XRD, and Raman spectroscopy. From XRD pattern we calculated an interplanar distance between graphene layers in separate FLG nanosheet to be 0.404 nm. This value is bigger than that of natural graphite due to the use of expanded graphite as an initial material for exfoliation. The average FLG nanosheet thickness and lateral dimension are 5 nm and 300 nm, respectively.

Keywords: few-layered graphene, Langmuir-Schaefer technique, palladium decoration, NO_2 and H_2 gas sensing, long-term stability

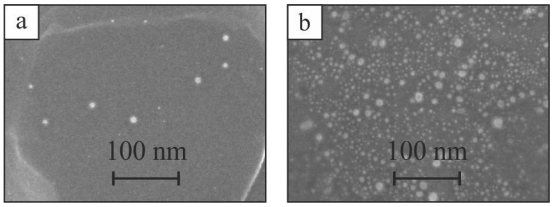

Figure 1: SEM images of Pd NPs decorated FLG Langmuir nanofilm with low (a) and high (b) concentrations of Pd NPs.

From the intensity of D vs. G Raman band, relatively low defects density is assumed in our samples. During the subsequent vacuum annealing (T=1100 K) of the FLG nanofilm an initial electrical resistance of FLG LS layer dropped from 2 MΩ to the final value of 10 kΩ at room temperature. Repeated heating cycles of FLG nanofilm revealed its semiconducting character. Besides removing absorbents such annealing leads to a healing of defects which act as adsorption centers for NO_2 gas molecules [3]. Therefore sensitivity decreases after an annealing at high temperatures (T=1100 K). Moreover the annealing leads to an improvement of electrical conduction of the FLG flakes deposit. As a result the level of noise decreases. The FLG nanofilm was decorated by colloidal Pd nanoparticles (6–7 nm, PlasmaChem, 0.1 mg/ml in chloroform) by spin-coating technique. We prepared several samples with different concentrations of Pd nanoparticles (Fig. 1) by multiple spin-coating cycles with a constant drop volume of 5 µl and rotation speed of 10 rps. It was shown that 2-3 cycles (10-15 µl of NPs solution) is already enougth to fully cover the surface of FLG nanofilm by Pd nanoparticles. The distribution of Pd NPs with the lowest concentration was prepared after the first cycle at 75 rps. SEM analysis confirmed uniform distribution of Pd nanoparticles over the FLG nanofilm, the nanoparticles being preferentially located at the edges of individual nanosheets. After the decoration the structure was annealed at 600 K in order to remove surfactants from Pd nanoparticles. The crystallinity of Pd nanoparticles after the annealing was confirmed by HRTEM.

Results and Discussions:
The gas sensing properties were tested in a mixture of dry air and NO_2 gas with concentrations in a range of 2–200 ppm and in a mixture of dry air and H_2 gas in a range of 10-10000 ppm from room temperature up to 250°C. The response of FLG nanofilm

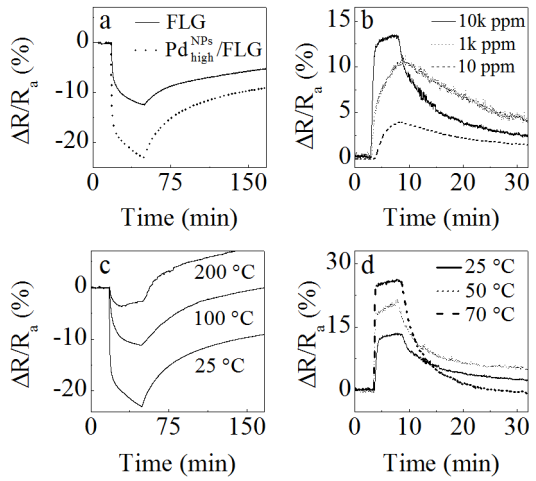

Figure 2: Response to 6 ppm of NO_2 (a) and 10, 1000, 10000 ppm of H_2 (b) gas mixtures for Pd NPs decorated FLG sensors at room temperature and voltage of 2 V (decoration by Pd NPs was performed with one spin-coating cycle at 10 rps). Temperature effect on the sensitivity to 6 ppm of NO_2 and 10000 ppm of H_2 gases is shown in (c) and (d), respectively.

with Pd decoration is of p-type for all mixtures. The gas response $\Delta R/R_a$ = -22% (sensor resistance change related to resistance in air) was observed for the exposition to 6 ppm NO_2 at room temperature (Fig. 2). The decoration by Pd NPs increased the sensitivity to NO_2 gas approximately twice. The saturation of gas response to both NO_2 and H_2 gases was observed when the surface of FLG nanofilm become fully covered by Pd NPs (Fig. 3). In the case of NO_2 gas detection, higher operating temperatures accelerate desorption processes, lowering sensitivity and minimizing the recovery time. A rather long recovery time during NO_2 gas sensing can be attributed to the intercalation of FLG nanosheets by the gas molecules.

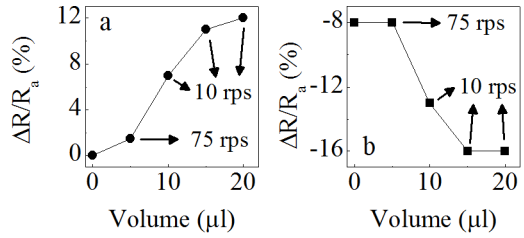

Figure 3: Effect of decoration of FLG nanofilm by Pd NPs with different concentrations on gas response to 1000 ppm of H_2 (a) and 3 ppm of NO_2 (b) gases at room temperature. Volume is the amount of Pd NPs solution applied onto FLG nanofilm by spin-coating.

The sensitivity of Pd NPs decorated FLG nanofilm to H_2 gas increases with increasing temperature due to an enhanced chemical reactivity between the gas and the sensor. For 10000 ppm and 1000 ppm of H_2 gas, the response at room temperature of 13% and 10% was found, respectively. At minimum test concentration 10 ppm the response of 4% was measured. The maximum sensitivity of 27% was achieved at 70°C. After 6 month storage of the device in air, the response to 6 ppm of NO_2 gas decreased only from 22% to 20%.

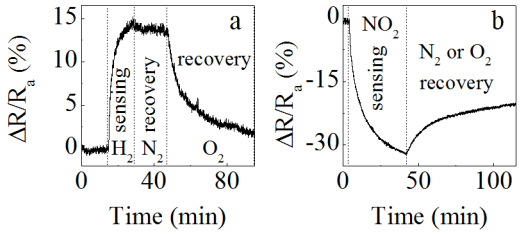

Figure 4: Recovery of the sensors after exposure to 1000 ppm of H_2 (a) and 200 ppm of NO_2 (b) gas at room temperature.

The NO_2 gas sensor can be recovered by oxygen or nitrogen flow with the same rate (Fig. 4b). This suggests weak bonding between NO_2 gas molecules and the surface of FLG nanosheets forsing the desorption of NO_2 gas molecules. As it was already mentioned, chemical reactions come into play in the case of H_2 sensing by Pd decorated FLG nanofilm. When H_2 molecules meet Pd NPs, they tend to form palladium hydride with a lower work function than that in pure Pd. This forces electrons to move from Pd atoms to FLG nanofilm increasing resistance of the whole system. In this case, the recovery appears after decomposition of the palladium hydride into hydroxyl and water in air. Therefore contrary to the NO_2 gas sensor, only the oxygen flow was effective to recover the H_2 gas sensor (Fig. 4a).

Conclusions:

The sensing properties of our devices are fully comparable to those of other types of graphene sensors and nanoparticle-based sensors of transition metal oxides [1-3].

Acknowledgements

This work was supported by the projects VEGA 2/0010/15, APVV-14-0120, APVV-14-0891, CNR-SAS programme 2016–2018, SAS-TUBITAK JRP 2013/6, COST MP1307.

References:

1. Y. Pak, et. al, (2014), Palladium-decorated hydrogen-gas sensors using periodically aligned graphene nanoribbons, *ASC Appl. Mater. Interfaces*, 6, 13293 – 13298.
2. Cagliani A., et.al, (2014), Large-area nanopatterned graphene for ultrasensitive gas sensing, *Nano Research*, 7, 743 – 754.
3. Capone S., et. al, (2014), Fe_3O_4/γ -Fe_2O_3 nanoparticle multilayers deposited by Langmuir-Blodgett technique for gas sensing, *Langmuir*, 30, 1190 – 1197.